Search for multiquark states decaying into neutral strange particles, kaons and lambdas, using the ATLAS detector

ANTARA PAUL

Department of Physics
McGill University
Montréal, Québec, Canada
October 5, 2022

A thesis presented for the degree of Master of Science in Physics

Abstract

Conventional matter consists of mesons and baryons, made of two or three quarks, respectively. However, the Standard Model of Particle Physics does not forbid particles consisting of more than three quarks, although very few have been observed clearly up to now. This thesis is a feasibility study on the search for possible exotic hadronic states using strange particles, the K_s^0 meson and the Λ^0 baryon, with data collected during proton-proton collisions with a center-of-mass energy $\sqrt{s} = 13$ TeV at the ATLAS detector. Minimum bias events collected in 2015 are used in this analysis, which corresponds to an integrated luminosity of 21.559 nb^{-1}. K_s^0 and Λ^0 are first identified in the data with high efficiencies, and their lifetime distributions and invariant mass distributions are obtained. The lower mass range of $K_s^0 K_s^0$ spectrum is investigated and a peak at $\sim$1535 MeV, presumably the $f_2'(1525)$ state, is observed. A data-driven signal searching technique is then performed on the higher range of the invariant $K_s^0 K_s^0$, $K_s^0 \Lambda^0$ and $\Lambda^0 \Lambda^0$ mass spectra to look for possible tetraquark, pentaquark and hexaquark states. No observation of signal with $> 5\sigma$ significance has been made. An extensive study using Monte Carlo simulations and full Run-2 data would be required to place limits on the cross-section of the multiquark state masses.

Résumé

La matière conventionnelle est faite de mésons et de baryons, respectivement composés de deux ou trois quarks fondamentaux. Le Modèle Standard de la Physique des Particules n'exclut pas l'existence de particules composées de plus de trois quarks, bien que très peu aient été observées avec certitude jusqu'à présent. Cette analyse porte sur la recherche de tels états hadroniques exotiques possibles par le biais de particules étranges neutres, le méson kaon et le baryon lambda. Les données “Minimum Bias” de 2015 du détecteur ATLAS, prises lors de collisions proton-proton à une énergie du centre de masse de 13 TeV, ont été utilisées, correspondant à une luminosité intégrée de 21.559 nb^{-1}. Les kaons et lambdas sont d'abord identifiés dans les données avec grande efficacité. Une techniques de détection de signal est ensuite appliquée. Le domaine des basses énergies du spectre $K_s^0K_0$ est d'abord étudié et un signal à ~1535 MeV est observé, probablement l'état $f_2'(1525)$. Une technique de recherche de signal est alors appliquée à des plus grandes énergies aux spectres de masse invariante kaon-kaon, kaon-lambda et lambda-lambda pour repérer de possibles états de tetraquark, pentaquark and hexaquark, respectivement. Aucun signal avec une significance supérieures à 5 déviations standards n'a été observé. Une étude approfondie utilisant des simulations Monte Carlo et l'ensemble des données de la campagne 2 seraient nécessaires pour déterminer les limites en section efficaces pour les masses des états multi-quarks.

Acknowledgements

This thesis has not been due to my hard work alone; rather it is the culmination of so many others' contributions to my life. This section is dedicated to that long, non-exhaustive list of people who shaped my life as it is now.

Firstly, I would like to extend my gratitude towards my supervisor, Prof. François Corriveau, who has patiently explained to me all the physics concepts and provided me with the motivation to carry on my analysis, even on days I felt stuck. This thesis would not have been possible without his constant guidance and belief that I could make it. I would also like to thank Dr. Raphael Hulsken, who took time to clear my computational doubts and took out time for me despite the 6-hours time difference between us. Many thanks to Prof. Andreas Warburton who would take great interest in my analysis and provide me hints on how to go forward with it.

A huge chunk of my work could not be done if not for the help from members of the ATLAS-McGill group. I have learned to efficiently use computational tools from them, but most importantly, I have learned that not everything in particle physics can be learned in a day. My first year of masters has been a painstaking remote one, but the friendships fostered over Zoom classes and assignment discussions with Chloe, Ivan, Melissa and Louis will be cherished forever. The transition to the in-person life has been initially awkward but my seniors and colleagues made sure I never had a dull time; thank you, Matteo, Alessandro, Nirmalya, Vishwangi, and Bryce! And finally, Shreya, who has been my office-mate and senior in the ATLAS group, but most of all, has been my elder sister in Montreal.

I would have been exhausted by the end of masters, had it not been for my wonderful friends. To Fathima, Siril and Sripadh, with whom I started my journey here. And to Avishek, who has laughed in the rain and cried on the sunniest days with me, and held my hand throughout.

But most importantly, this is to my parents and sister, who have stood like a wall behind me, never letting me crumble and lose despair. They made me feel like the most gifted person ever, even on days I could not put one and one as two. To them, I dedicate this thesis.

I am missing out on so many more people whose littlest actions have had the greatest impacts on my life and on this thesis, but I will end this section acknowledging that our lives are entangled in the most intricate of ways and there was once probably a humble fiction writer who led me to pursue particle physics years later.

Contribution of the Author

The analysis and the results presented in this thesis are the author's original work. All the chapters in this thesis are written by the author and the main analysis starts from Chapter 4. The analysis is done within the ATLAS software framework, which is built by the contributions of collaborators all over the world.

Table of Contents

List of Figures

List of Tables

Chapter 1

Introduction

Over the last century, developments in theory and discoveries in experiments have led to the better understanding of the building blocks of our universe. The standard model (SM) of particle physics is a gauge theory which describes three out of four fundamental laws of physics - weak, strong and electromagnetic interactions. It includes the electroweak model and quantum chromodynamics (QCD), the theory of strong interactions. Despite the success of the SM in being able to predict or explain phenomena observed in high energy physics experiments, there are still questions the theory does not answer. Some of them include the origin of non-zero neutrino masses, Dark Matter (DM) or the incorporation of the fourth force, gravity, into the SM. Several searches and tests are being carried out by different experiments to better understand the SM or test different theoretical models which predict the extensions of the SM.

One of the interesting aspects of the SM is QCD, which describes the interactions between quarks and gluons that make up composite hadrons, the color singlet states. QCD, and consequently, the quark model have been successfully able to explain the spectroscopy of the conventional baryons (qqq) and mesons ($q\bar{q}$). Beyond these, QCD does not forbid the existence of more complex color singlet states, which comprise more than three quarks. These 'exotic' hadrons are referred to as multiquark states. $X(3872)$ was the first tetraquark to be unexpectedly discovered by the Belle collaboration in 2003 [1]. Since then, different experiments have probed into the search for exotic hadrons and been successful [2].

Several theoretical models attempt to explain the different mechanisms that a multiquark could be formed. However, it is challenging for QCD to consistently explain the origin of the wide range of multiquark states that have come into the fore and more that are still waiting to be discovered. Thus, it is now up to experiments to drive forward the field of exotic spectroscopy and study the properties of observed multiquark states.

The $K_s^0 K_s^0$ mass spectrum has been under scrutiny for long. Previous searches for exotic hadrons, like glueballs have been conducted by the L3 [3] and ZEUS [4] experiments in the $K_s^0 K_s^0$ mass spectrum. Several mesons like the $f_2(1270)$ and $a_2(1320)$ states were found in this spectrum, which were, prior to observation, assumed to be exotic. Proton-proton collisions at higher centre-of-mass energy of $\sqrt{s} = 13$ TeV in the ATLAS [5] detector facilitate the study of the $K_s^0 K_s^0$ mass spectrum at energies higher than 3 GeV, which is where most of the multiquark states have been discovered up to now.

This thesis is a feasibility study to look for multiquark states using the strange hadrons, K_s^0 and Λ^0. The K_s^0 and Λ^0 particles are first reconstructed from the decay channels $K_s^0 \rightarrow \pi^+\pi^-$ and $\Lambda^0 \rightarrow p^+\pi^-$. These channels are used as the final state particles, the pions and proton, have very clean signatures in the ATLAS detector. Using a bump search method over a large combinatorial background, the $K_s^0 K_s^0$ mass spectrum is investigated to look for a possible tetraquark state in the energy range of 2.9-8 GeV. Using the same search method, the $K_s^0 \Lambda^0$ and $\Lambda^0 \Lambda^0$ mass spectra are investigated to look for possible pentaquark and hexaquark states respectively. The specific combinations are chosen as such since their invariant masses are close to the production threshold of the respective multiquark states with loosely bound constituent particles. In other words, the total number of quarks needs to be conserved.

The thesis is structured as follows: Chapter 2 gives an overview of the theory with an emphasis on the exotic hadron spectroscopy. Chapter 3 comprises a description of the LHC and specifically, the ATLAS detector and its sub-systems. Chapter 4 goes into the details of the reconstruction of the K_s^0 and Λ^0 particles, and further, the $K_s^0 K_s^0$, $K_s^0 \Lambda^0$ and $\Lambda^0 \Lambda^0$ combinations. The lifetime and invariant mass distributions of K_s^0 and Λ^0 are discussed in chapter 5. Chapter 6 investigates the lower energy range of the $K_s^0 K_s^0$ spectrum, comparing results with previous experiments. Finally, in Chapter 7, the bump search method is explained and results from using the method on all three mass spectra are presented. The thesis ends with a conclusion and outlook in chapter 8.

Chapter 2

Theory

2.1 The Standard Model of Particle Physics

The Universe is understood to be constituted of elementary particles. The Standard Model of Particle Physics [6, 7] provides a comprehensive understanding of these particles and the interactions among them.

The four types of fundamental interactions are: gravitational, electromagnetic, weak and strong interactions. Of these four, gravity is considered insignificant on the scale of particle interaction. The fundamental particles in the standard model are broadly classified into three groups: the spin-$\frac{1}{2}$ fermions, the spin-1 gauge bosons and the spin-0 Higgs Boson.

2.1.1 Introduction

The Standard Model is a gauge quantum field theory described by the symmetry group

$$SU(3)_C \times SU(2)_L \times U(1)_Y \tag{2.1}$$

where the $SU(3)_C$ gauge field describes the strong interaction and the $SU(2)_L \times U(1)_Y$ gauge fields combine to describe the electroweak theory. The quanta of the gauge fields are the gauge bosons, which mediate interactions between the different kinds of fermions.

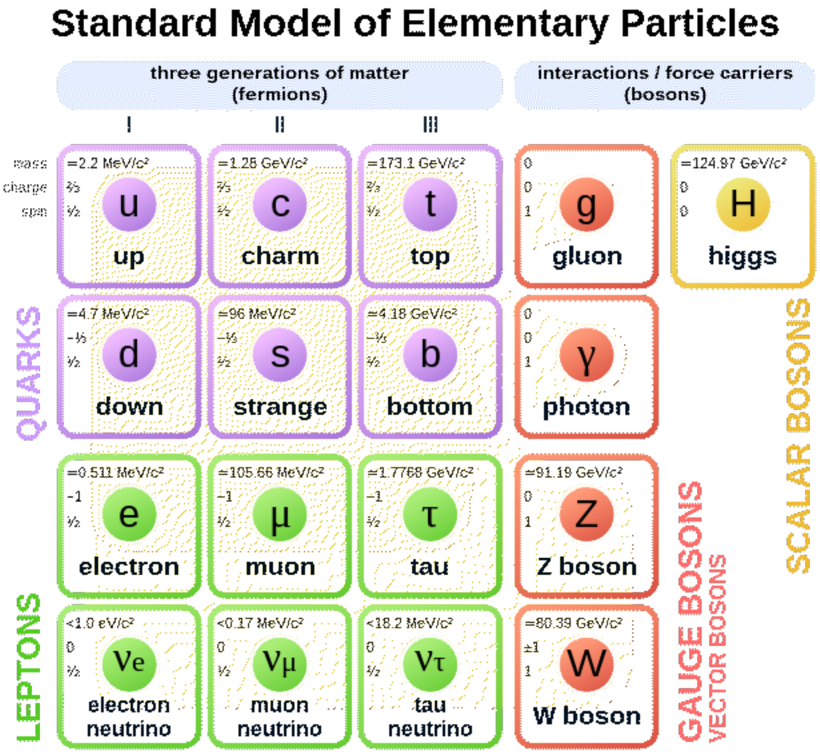

Figure 2.1: Standard Model of particle physics: the 12 fundamental fermions classified into three generations and the 5 gauge bosons [8]

2.1.2 Particle Content of the Standard Model

As previously mentioned, there are three groups of fundamental particles in the SM. The gauge bosons are the mediators of the different interactions. The electromagnetic interaction is mediated by the *photons* (particles without mass, electric charge or color). The strong interaction is mediated by the *gluons* (particles without mass or electric charge, but carrying color charge). The weak interaction is mediated by the massive $W^{\pm}$ and Z^0 *bosons*. The Higgs field interacts with the W and Z bosons to give them mass.

The fermions can be classified into *quarks* and *leptons*. There are six leptons and six quarks, with pairs of similar particles classified into three generations each. Fig. 2.1 shows the 12 fermions placed in three columns, each representing one generation.

As shown in Fig 2.1, the electron and its neutrino, ν_e are the first generation of leptons. The muon μ^- (tau τ^-) along with its corresponding neutrino ν_μ (ν_τ) form the second (third) generation.

Leptons have an associated quantum number called the lepton number, which is 1 for leptons and -1 for anti-leptons. The leptons electron (e^-), muon (μ^-) and tau (τ^-) are electrically charged, while their corresponding neutrinos (ν_e, ν_μ and ν_τ) are electrically neutral. The masses of the charged leptons increase with each generation. The masses of the three neutrinos are not yet determined precisely, but they are very small, with an upper limit of the order of eV for ν_e and a few MeV for ν_μ and ν_τ. All leptons experience the weak interaction, and the charged ones experience the electromagnetic interaction as well.

All the quarks have fractional electrical charge: $\frac{2}{3}$ for up-type quarks and $-\frac{1}{3}$ for down-type quarks. The up-type quarks are up (u), charm (c) and top (t) while the down-type quarks are down (d), strange (s) and bottom (b). The u and d quarks form the first generation, while the c (t) and s (b) quarks form the second (third) generation. The masses of the quarks increase with each generation. The quarks, like gluons, have a 'color' charge which is responsible for the strong interaction. All quarks experience the weak and electromagnetic interactions as well. More about quarks will be discussed in the next section.

Finally, there exists the Higgs boson, which is a spin-0 scalar particle. It is the quantum particle of the Higgs field. Other particles (except photons and possibly, neutrinos) interact with this field, which leads to them acquiring mass. It is the last element of the SM to be discovered in 2012 by the ATLAS [5] and CMS [9] experiments, and validates the theory of the SM.

Every particle in the standard model has its own anti-particle which has the same mass but opposite quantum number. They form the antimatter.

2.1.3 Limitations of the Standard Model

The Standard Model has been successfully able to predict and explain most of the phenomena observed in high energy collisions. However, it has certain shortcomings which are described in brief here.

One of the major problems in the SM is the *hierarchy problem* [10]. The Higgs mass is of the order of 100 GeV, which is the electroweak symmetry breaking scale. However, the mass of Higgs receives corrections of the order of Planck scale (10^9 GeV) which are much larger than the actual mass of the Higgs, due to the presence of heavy, virtual top quarks. The observation of the low, actual mass is explained by its fine-tuning such that it almost completely cancels the corrections. This explanation is considered superficial. Moreover, the origin of the the wide range of masses of elementary particles, ranging from 0.511 GeV for the electron to 170 GeV for the tau, is still unresolved.

This brings another problem to the fore, that is the mass of neutrinos. The SM describes neutrinos as massless as a result of containing only left-handed neutrinos. However, experiments have now placed upper limits of the order of eV for ν_e and a few MeV for ν_μ and ν_τ [11]. This requires an extension to the existing SM theory, either by adding a separate right-handed neutrino and making them couple to the left-handed neutrino, which would make them Dirac particles or by having a right-handed neutrino which is its own anti-particle, which would make them Majorana particles.

Yet another problem is the exclusion of gravity, one of the four fundamental forces, from SM. It also fails to explain why gravitational force is so weak as compared to the other forces.

According to cosmological observations, the baryonic matter makes up only 5% of the universe, which is explained by the SM. It does not account for the unknown type of Dark Matter which makes up 25%. Moreover, it does not provide a good explanation of the rest 70% of the universe made of dark energy [10].

2.2 Quantum chromodynamics and the system of quarks

The strong interaction is described by the theory of quantum chromodynamics (QCD) which is mediated by an octet of massless colored gluons. They correspond to the eight generators of the SU(3) symmetry. The three orthogonal states of the SU(3) symmetry are represented by the three colors r, g, b. Colored particles have not been observed to exist freely but remain confined in color singlet hadronic states. This is because, the gluon-gluon interaction modifies the QCD coupling strength α_s in such a way that it increases as the distance keeps increasing, as shown in Fig. 2.2 (opposite to how the quantum electrodynamics coupling strength behaves). Due to the confinement of these states, the QCD Lagrangian is unable to describe the complete spectrum of hadrons using any first-principle methods, but efforts are put to understand the spectrum using lattice QCD [12]. The best established of these colorless states are the baryons, consisting of three quarks (qqq) and mesons, consisting of a quark-antiquark pair ($q\bar{q}$) [13, 14].

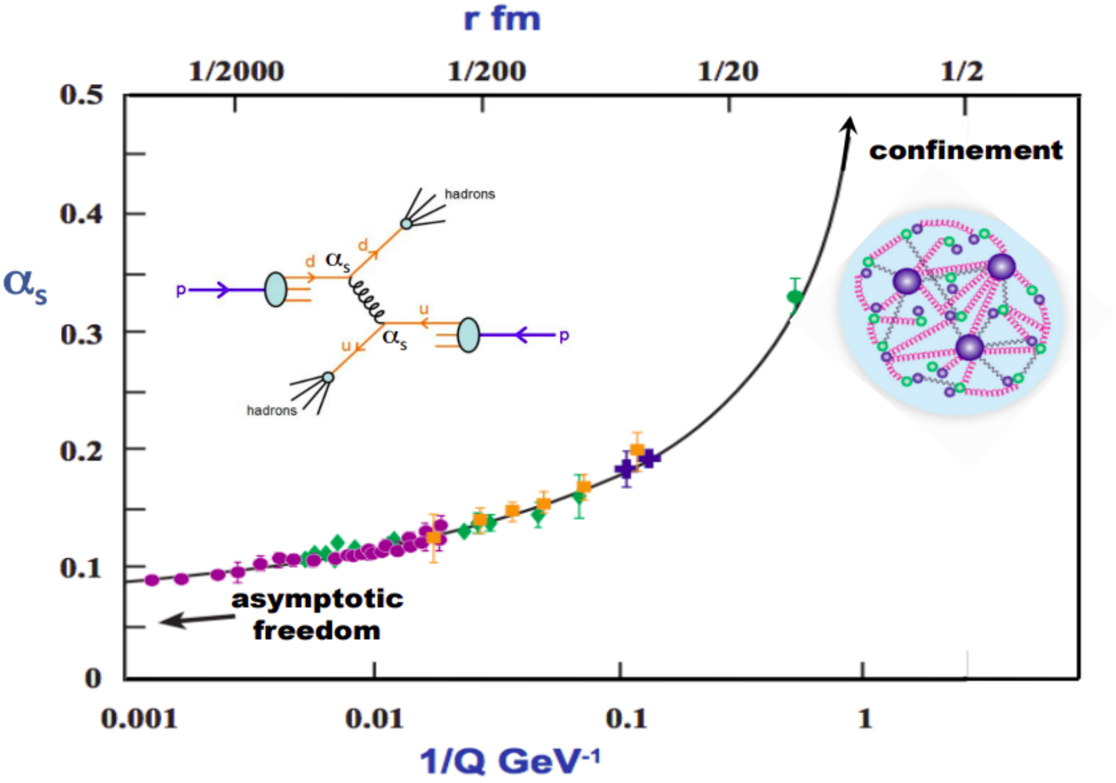

Figure 2.2: The behavior of the QCD coupling strength α_s as a function of the inverse momentum transfer $1/Q$ or, equivalently, the quark separation distance r [12].

2.2.1 The exotic states

However, more color singlet states beyond these two can exist in nature. A hadron of two quarks and two antiquarks can form a color singlet: such a system would be an exotic meson called ‘tetraquark’ ($qq\bar{q}\bar{q}$). Another way to form a color singlet hadron is to have a baryon together with a quark antiquark pair. This would result in an exotic baryon called ‘pentaquark’($qqqq\bar{q}$). A composition of two baryons or three mesons could also be possible, which would result in a ‘hexaquark’ (q^6 or $q^3\bar{q}^3$) state. Such states have not been forbidden by theory and searches for these states are being carried out by various experiments [15].

It is also important to note that gluons contribute to hadron quantum numbers as well. As such, gluon-gluon pairs or gluons combined with quarks can also form colored singlets. Exotic hadrons made of only gluons (and thus no quarks) are called glueballs [16, 17].

Yet another way of forming colorless states is having ordinary mesons with at least one gluon. Such states are known as hybrids [17].

2.2.2 Theoretical models

Several phenomenological models based on non-perturbative QCD are proposed to understand the strong interactions which give rise to the exotic hadrons. The two most important of them are the *compact multiquark* picture based on the QCD color, and the *molecular* picture [12].

In the first case, multiquark hadrons can exist in the form of tightly bound colored diquarks and diantiquarks, hybrids comprised of color singlet baryons and mesons combined with one or more valence gluons or glueball mesons comprised of only gluons. This case is basically the one described in Section 2.2.1.

In the second case, meson-meson and meson-baryon molecular states can be formed via Yukawa-like nuclear forces. Such states would have masses close to the threshold of constituent particles' masses, since the binding energy is of the order of a few MeV [12].

2.3 Exotic hadron spectroscopy

The established exotic hadrons have been mostly found in the *charmonium* ($c\bar{c}$) and *bottomonium* [1] ($b\bar{b}$) states as the spectrum at the energy scale of c and b quarks are clean and free from interference patterns. The first exotic state to be found was X(3872), which has a charmonium structure [1]. On the other hand, the masses of the light quarks, that is, u, d and s quarks are in the scale of 5-100 MeV which make them comparable to the scale of QCD. This would make it difficult to discern exotic hadrons from the conventional ones due to their broad structures and interference patterns [2].

---

[1] Quarkonium is a flavorless meson consisting of a heavy flavor quark and its antiquark. Thus, it is a neutral particle and its own antiparticle. Charmonium and bottomonium are types of quarkonia.

This thesis is a feasibility study on the search for possible multiquark states consisting of strange quarks. A possible tetraquark structure is searched in the $K_s^0 K_s^0$ spectrum, a pentaquark structure is searched in the $K_s^0 \Lambda^0$ spectrum and a hexaquark structure is searched in the $\Lambda^0 \Lambda^0$ spectrum. If there indeed exist such structures decaying into the final states of $K_s^0 K_s^0$, $K_s^0 \Lambda^0$ and $\Lambda^0 \Lambda^0$, they would be seen as resonant 'bump' in their respective invariant mass spectra over large combinatorial backgrounds. The motivation arises from previous investigations of the $K_s^0 K_s^0$ spectrum which has resulted in the observation of possible glueball candidates and tensor mesons[2] by the ZEUS and L3 experiments, plots as shown in Fig. 2.3.

The search is further motivated by the most recent observation by the LHCb collaboration of a pentaquark state (among other multiquark states) containing a strange quark [19]. The pentaquark, $P_{\psi S}^{\Lambda}(4338)^0$ with a minimum quark content ccuds is the first one observed to contain an s quark, with mass and width of 4338.2 ± 0.7 MeV and 7.0 ± 1.2 MeV, respectively Fig. 2.4 shows a list of exotic hadrons observed in the LHC so far. The widths of such states vary over a wide range, from 6.4 ± 2 MeV for $P_{\psi}^{N}(4457)^+$ to 136 ± 23 MeV for the recently discovered tetraquarks, $T_{cs0}^{a}(2900)$.

---

[2] In particle physics, a tensor meson is a spin-2 meson with an even parity.

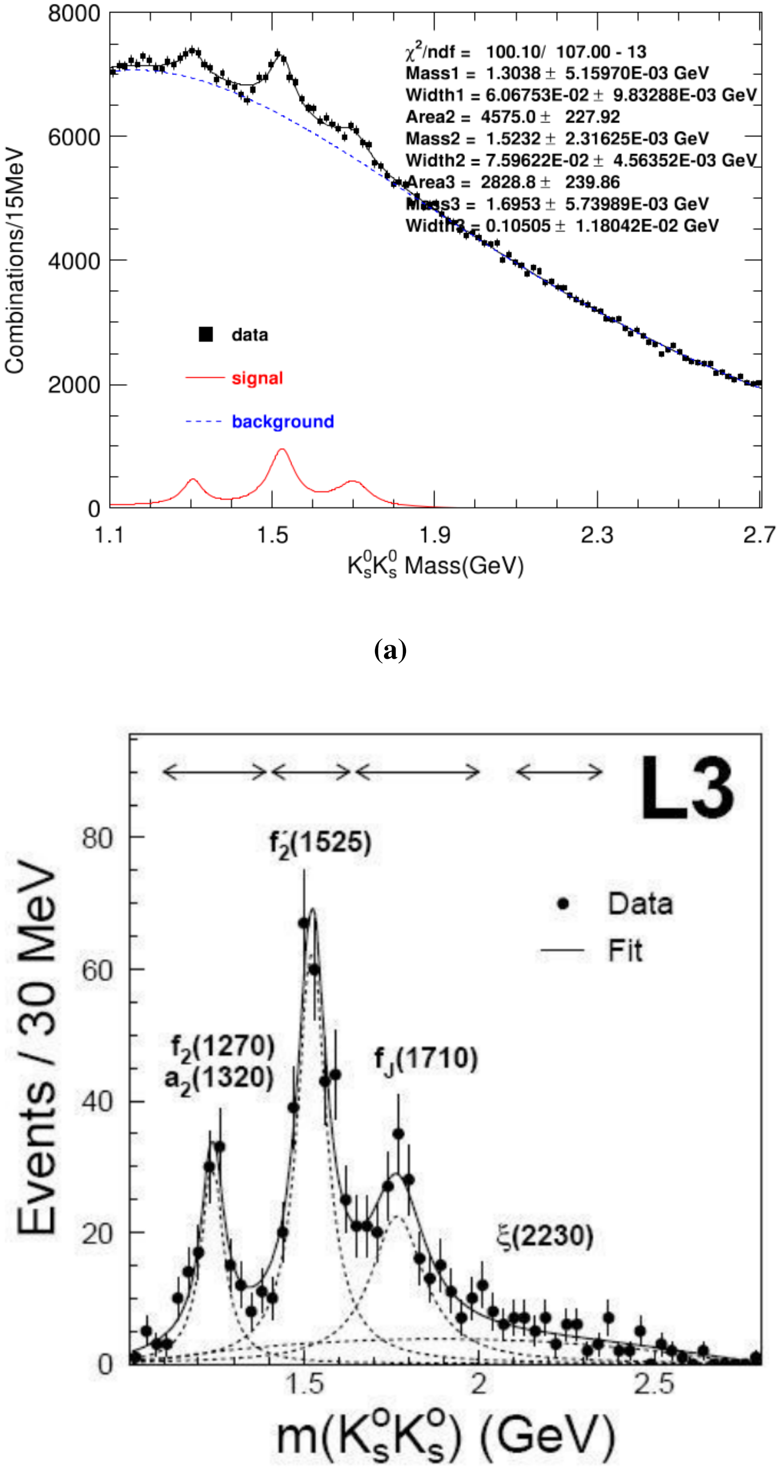

(a)

(b)

Figure 2.3: $K_s^0K_s^0$ invariant mass spectra in the (a) ZEUS [4] and (b) L3 experiments [3]. The plots show resonances observed in the energy range 1.1-2.7 GeV. The $f_2(1270)$ $f_2'(1525)$ are mesons, $f_J(1710)$ is a possible glueball candidate.

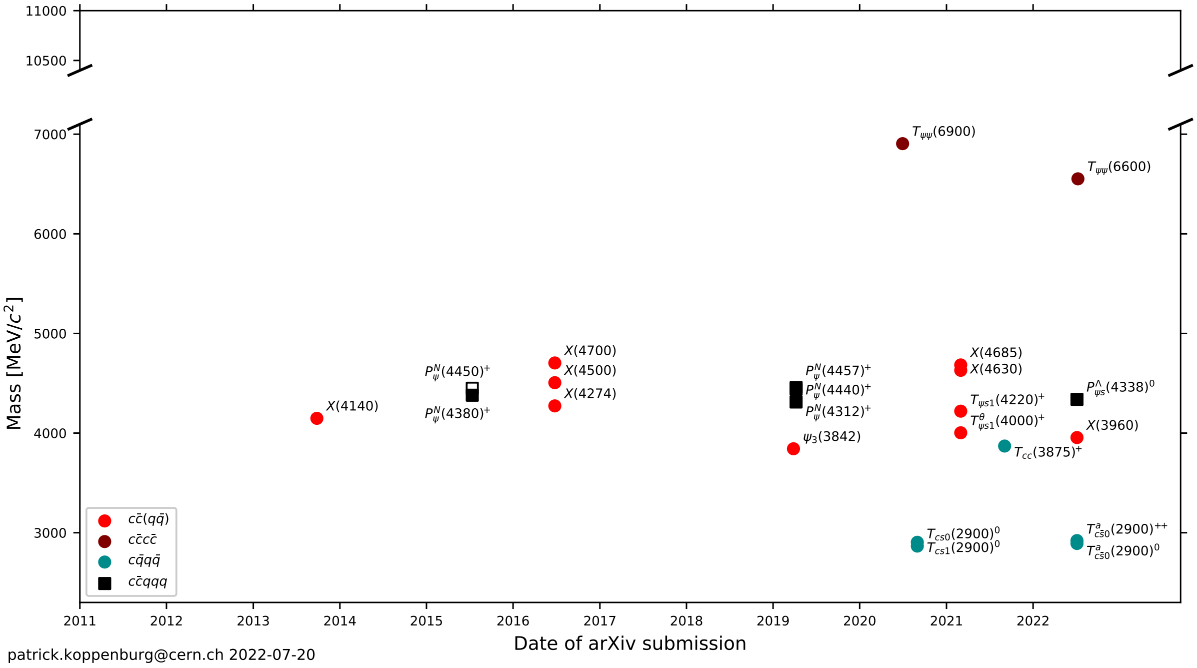

Figure 2.4: Exotic hadrons found in the LHC so far. Observations with significance greater than 5σ are reported only [18].

Chapter 3

Experimental Setup

The study of fundamental particles is facilitated by particle accelerators, which use electromagnetic fields to accelerate particles close to the speed of light and collide them [20].

The European research organization, CERN (originally derived from the French name *Conseil européen pour la recherche nucléaire*) houses the largest particle accelerator in the world, the Large Hadron Collider (LHC). Starting with the 600 MeV Synchrocyclotron in 1954[21], it now hosts a range of particle colliders as well as advanced computing facilities, with the principal aim of carrying out fundamental research.

This chapter starts with an overview of the accelerator complex at CERN, followed by a short description of the LHC and finally proceeds to briefly describe the ATLAS detector.

3.1 CERN accelerator complex

The LHC is only the final machine in a series of particle accelerators, which is better known as the 'CERN accelerator complex' [22]. Starting with hydrogen anions that are accelerated to 160 MeV in the Linear Accelerator (Linac4), the beam passes through a series of accelerators as illustrated in Fig. 3.1 to finally become a proton beam of energy 450 GeV in the Super Proton Synchrotron (SPS). This proton beam is then finally injected to the two rings of the Large Hadron Collider, where the protons circulate in opposite directions, and are currently, after the Long Shutdown 2 (LS2), projected to reach an energy of 6.8 TeV.

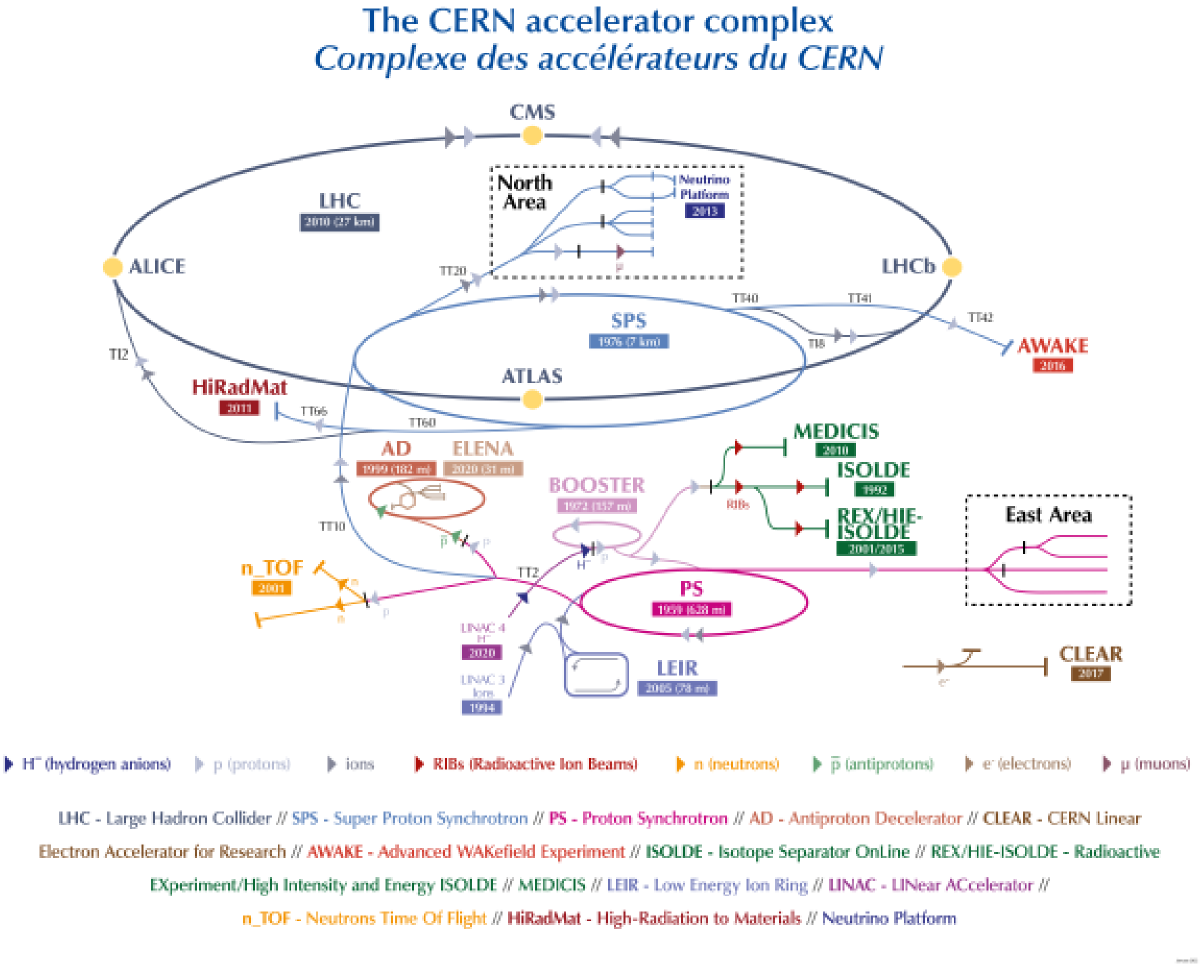

Figure 3.1: The CERN accelerator complex [23]

3.2 The Large Hadron Collider

The world's most powerful particle accelerator, the Large Hadron Collider (LHC), has a circumference of 27 km and is located 175 m underneath the Franco-Swiss border near Geneva. Each of the two rings of the LHC, maintained at a pressure of $10^{-10} - 10^{-11}$ mbar for the lowest possible scattering and energy losses, receives the proton beam at 450 GeV. The proton beams are directed along the path of the beam pipes in 'bunches' by superconducting magnets which generate a magnetic field of 8.3 T and are accelerated using radiofrequency (RF) cavities [24, 25, 26]. The electric field at each RF cavity is oscillated at 400 MHz which creates resonance and accelerates the protons, provided the timing of passage of the protons. Several upgrades have been made to the LHC during LS2 to increases the maximum centre-of-mass energy of collisions from 13 TeV during Run 2 to 13.6 TeV (projected) for Run 3.

The beams inside the LHC are collided at four different points, each of which are associated with four particle detectors: **ATLAS** (**A** **T**oroidal **L**HC **A**pparatu**S**) [5], **CMS** (**C**ompact **M**uon **S**olenoid) [9], **LHCb** (**L**arge **H**adron **C**ollider **b**eauty experiment) [27] and **ALICE** (**A** **L**arge **I**on **C**ollider **E**xperiment) [28]. Of these, ATLAS and CMS are general-purpose detectors, and LHCb and ALICE are specialized detectors built to study B-physics and heavy-ion collisions, respectively.

3.2.1 Luminosity

The cross-section is a measure of the probability that any process occurs during a proton-proton collision, and can be calculated from the scattering amplitudes using perturbative QCD. The instantaneous luminosity, L, of two beams colliding head-on and given in units of $\mathrm{cm}^{-2}\,\mathrm{s}^{-1}$ is given by:

$$L = \frac{f N_1 N_2}{4\pi\sigma_x\sigma_y} \tag{3.1}$$

where N_1 and N_2 are the number of protons in each bunch, $f = 40$ MHz is the frequency of bunch crossing, and $\sigma_{x,y}$ are the root mean square (RMS) sizes of the beams at the interaction point in the beam axis. The time integral of the instantaneous luminosity is

$$L_{int} = \int_0^t L\, dt, \tag{3.2}$$

which is then used to calculate the total number of events i over a period of time:

$$N_{events} = L_{int}\sigma_{pp\to i}. \tag{3.3}$$

Here, $\sigma_{pp\to i}$ is the cross-section of the event i from a proton-proton collision.

3.3 The ATLAS detector

ATLAS is a general-purpose detector which operates with the general aim of carrying out multiple physics analyses ranging from tests of the Standard Model to looking for Beyond Standard Model (BSM) physics and dark matter particles. The ATLAS detector has the largest volume of all particle detectors ever built, with a length of 46 m and a diameter of 25 m. It has a powerful magnet system and is made up of different layers of detector subcomponents, namely, the inner detectors, calorimeters and the muon spectrometers. The data is detected by the trigger and collected by the data acquisition system. This chapter goes into some details of each of these components. [5]

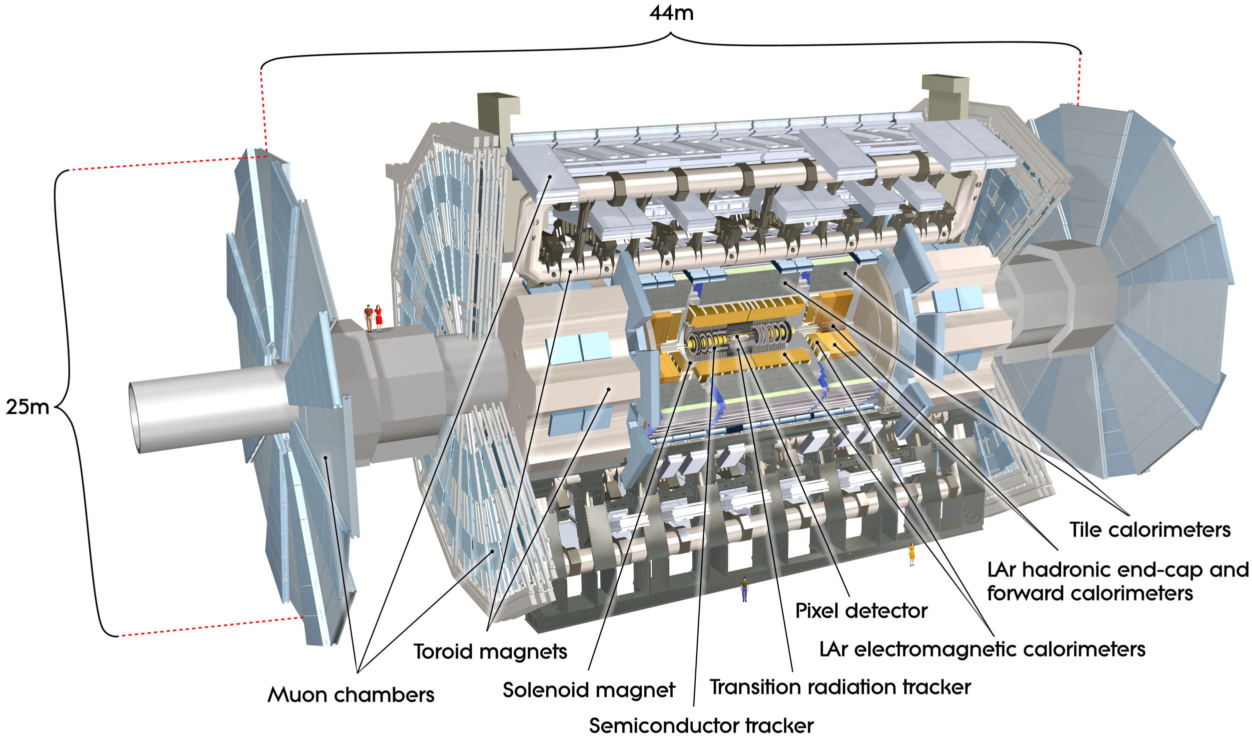

Figure 3.2: Cutaway labelled view of the ATLAS detector [29]

3.3.1 Coordinate System

The ATLAS frame of reference follows a right-handed Cartesian system, with the proton-proton interaction point defined as the origin [5]. The positive x-axis points toward the center of LHC, while the positive y-axis points upwards, making the z-axis along the beam pipe. A cylindrical symmetry can be defined around the beam axis, thus, a cylindrical coordinate system is followed to describe the particle trajectory in the experiment. The azimuthal angle $\phi \in [-\pi, \pi]$ is described around the z-axis, with $\phi = 0$ pointing towards the positive x-axis. The polar angle $\theta \in [0, \pi]$ is described from the z-axis, with $\theta = 0$ pointing towards positive z-direction. The polar direction of particles is described using pseudorapidity $\eta = -ln[\tan(\frac{\theta}{2})]$, with $\eta = 0$ being in the $x - y$ place and $\eta \longrightarrow \infty$ aligning with the beam axis. The angular separation between objects are expressed in terms of the azimuthal angle and pseudorapidity as $\Delta R = \sqrt{(\Delta\phi^2 + \Delta\eta^2)}$. As is evident from the naming convention, the transverse momentum (p_T) and the missing transverse energy (E_T^{miss}) are all defined in the $x - y$ (transverse) plane.

3.3.2 Magnet System

The motion of charged particles in a magnetic field can provide information about their momentum. The radius of curvature of a charged particle is directly proportional to its momentum and inversely proportional to the applied magnetic field. Thus, a high magnetic field needs to be employed to identify high momentum particles. ATLAS does so with a combination of four large superconducting magnets, as shown in Fig. 3.3:

- A central solenoid magnet provides a 2 T magnetic field for the inner detector along the beam axis.
- A barrel toroid magnet provides a 0.5 T magnetic field for the muon spectrometer in the central region.
- Two end-cap toroid magnets provide 1 T magnetic field for the muon spectrometer in the end-cap regions [5].

3.3.3 Inner Detector

The Inner Detector (ID) lies the closest to the interaction point, surrounded by a 2 T solenoid magnetic field and receives a high track density of approximately 1000 particles every 25 ns. It has the crucial task of tracking particle trajectories to precisely measure their momentum and reconstruct vertices. As such, high granularity needs to be achieved, which is facilitated by the

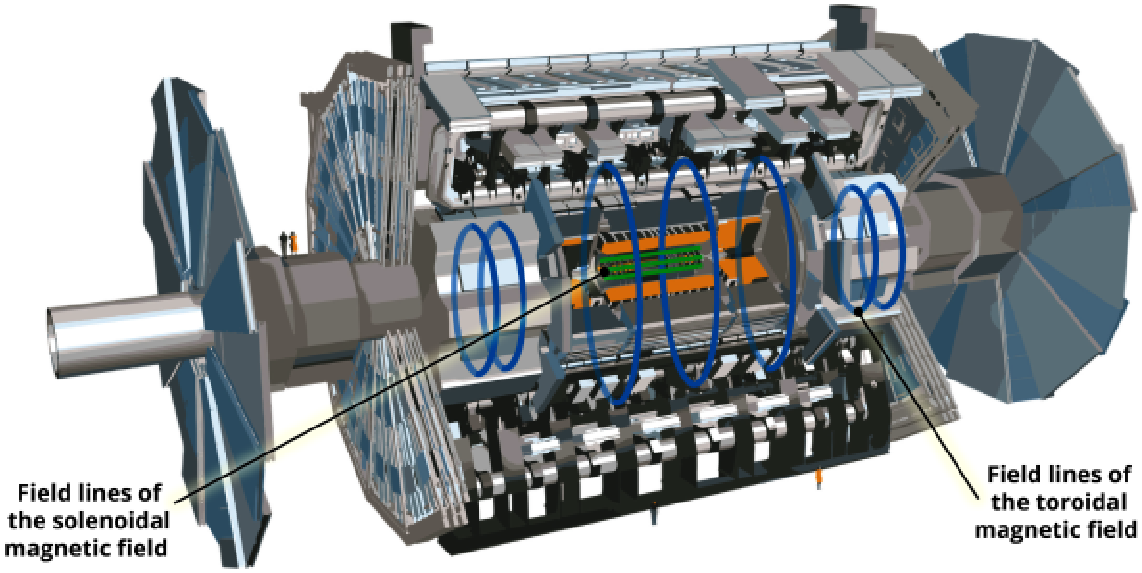

Figure 3.3: Cutaway labelled view of the ATLAS magnet system [30]

combination of the three subcomponents of the ID, each of which is divided into a barrel region surrounding the beam pipe and two end cap regions on either side of the barrel [5, 32]:

- The Pixel Detector (PD) is the innermost part of the tracking system, consisting of a barrel tracker and two symmetric end-cap trackers. It consists of silicon ‘pixels’ of size $50 \times 400\ \mu m^2$ arranged in three cylindrical layers (B-layer, Layer 1 and Layer 2) in the barrel region and in three layers of disks on either side in the end cap regions, with approximately 90 million readout channels. Before LHC Run-2, a new layer, called the Insertable B-layer, was added between the beam pipe and the existing B-layer to maintain detector performance despite radiation damage caused due to extremely high luminosity [33]. The pixel detector is designed to reconstruct particles with $p_T > 0.5$ GeV (or > 0.1 GeV for minimum bias events[1]) and $|\eta| < 2.5$ [5, 32].
- The Semiconductor Tracker (SCT) consists of silicon sensors in the form of ‘microstrips’ arranged in four cylindrical layers in the barrel tracker and nine disks on either side in the end cap regions, with approximately 6 million readout channels [5, 32]. Each microstrip module

---

[1] More about minimum bias events is discussed in Section 3.4

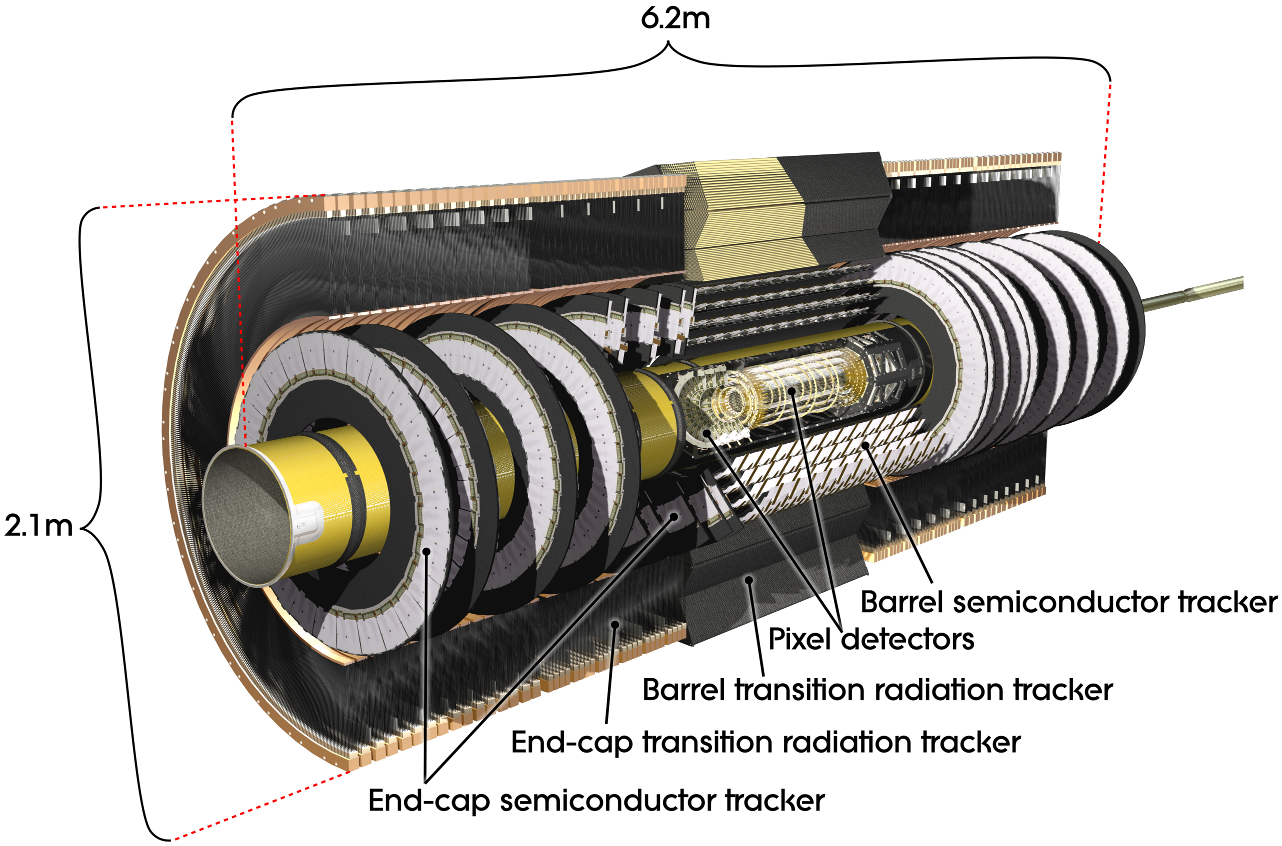

Figure 3.4: Cutaway labelled view of the ATLAS inner detector [31]

is made of two layers, whose axes are tilted by 40 mrad with respect to each other. The SCT provides a coverage of $|\eta| < 2.5$.

- The transition-radiation tracker (TRT), unlike the inner components, is not made of silicon detectors but consists of gas-filled straw drift tubes. It is made of 73 straw tubes arranged longitudinally in the barrel region and 160 straw tubes arranged radially in the end cap regions. When a charged particle passes through the gas mixture, it ionizes the gas, which results in free electrons. These drift towards the central wire, where they are amplified and read out. The straw hits can allow large number of readouts and longer measured track lengths. It is designed to reconstruct particles with $|\eta| < 2.0$ [5, 32].

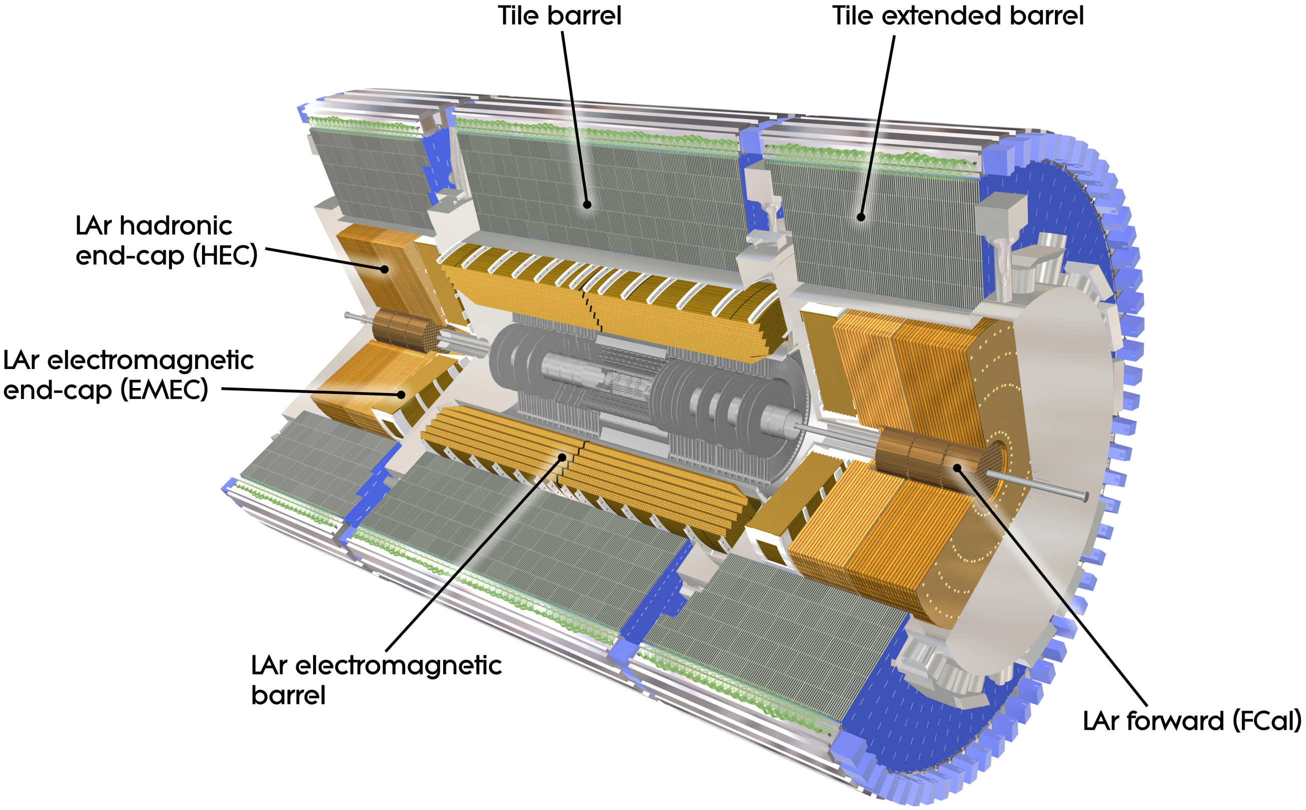

Figure 3.5: Cutaway labelled view of the ATLAS calorimeter [34]

3.3.4 Calorimeters

The calorimeter system is used to measure the energies of the traversing particles and effectively contain most of them before they reach the muon system. The calorimeters are built in a complex way, with alternating layers of passive and active medium. The passive medium is some dense material used to slow down particles, and the active medium is used to measure a fraction of the energy they lose and produce a signal. When particles pass through the calorimeters, their interactions with the dense, absorbing materials create a shower of secondary particles, which in turn produce a signal proportional to the deposited energy when they pass through the active material. Such calorimeters are called ‘sampling’ calorimeters as a portion of the energy of the incident particle is lost to the absorber medium, which makes them capable of ‘sampling’ the energy of the particle. Largely, the ATLAS calorimetry system can be subdivided into two based on the kind of particles, they effectively contain [5]:

- The electromagnetic calorimeter (ECAL) is used for precision energy measurements of photons and electrons with up to $|\eta| < 3.2$. It consists of a barrel region and two end cap regions. It uses lead as absorber plates to reduce the energy of the incoming particles and liquid argon (LAr) as the active detector medium interleaved with the plates. The active medium is chosen as such, as it is resistant to radiation and produces low noise on cooling. The ECAL has a thickness of $> 22X_0$ (radiation length)[2] in the barrel and $> 24X_0$ in the end caps to contain all the photons and electrons[5, 35].

- The hadron calorimeter (HCAL) is used for energy measurements of hadronic showers as well as E_T^{miss} measurements with up to $|\eta| < 4.9$. It consists of the Tile Calorimeter (TileCal) in the barrel, the Hadronic End-cap Calorimeter (HEC) and the Forward Calorimeter (FCal) at each end. The TileCal uses steel as the absorber and scintillating plastic tiles as the active medium. The HEC and FCal use LAr as the active medium, and dense metals like tungsten and copper as absorbers. The HCAL has a thickness of 9.7 λ (interaction length)[3] in the barrel and 10 λ in the end caps [5, 35, 36].

3.3.5 Muon Spectrometer

The Muon Spectrometer (MS) is the outermost detector sub-system. As the name suggests, it is responsible for the reconstruction of muons. It uses large superconducting air-core toroid magnets to bend the tracks of muons after they exit the calorimeters. The MS can measure the momentum of muons with pseudorapidity up to $|\eta| < 2.7$ and also trigger on muons with $|\eta| < 2.4$. Four chamber sub-systems make up the entire muon system: The Monitored Drift Tube chambers (MDT) in the barrel as well as in the end-cap, combined with the Cathode Strip Chambers (CSC) in the innermost end cap layer, provide precision tracking in the plane containing the beam axis (bending plane). Resistive Plate Chambers (RPC) in the barrel, together with Thin Gap Chambers (TGC) in the

---

[2] radiation length is the distance over which the energy of an electron becomes 1/e of its initial energy via the bremsstrahlung radiation

[3] nuclear interaction length is the average distance travelled by a hadronic particle before it undergoes inelastic nuclear interaction

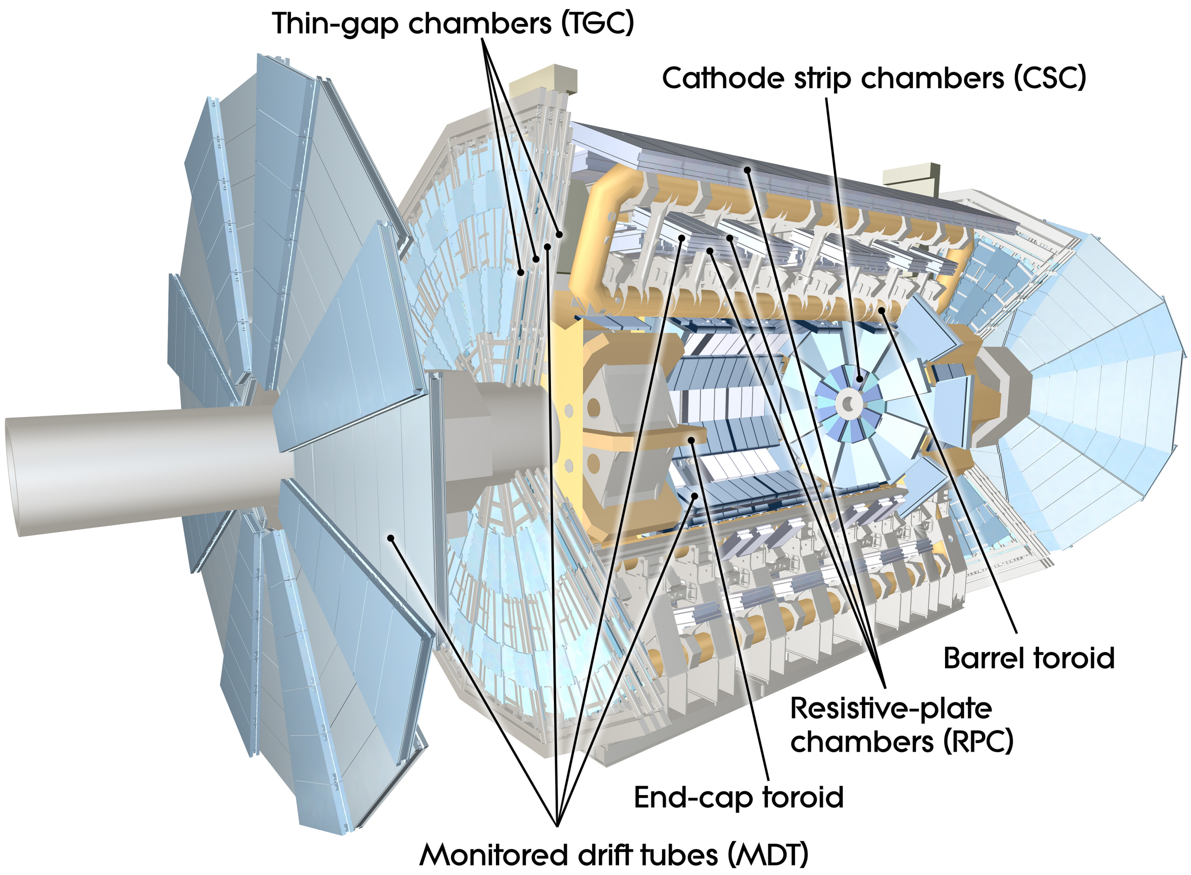

Figure 3.6: Cutaway labelled view of the ATLAS Muon Spectrometer [37]

end-cap, provide a fast trigger system to yield track information in the non-bending plane [5, 38, 39].

The MDT system consists of 30 mm diameter cathode tubes with a central anode wire. Each tube, filled with a mix of Argon-CO_2 gas, yields a spatial resolution of 35 μm. The CSC system consists of multi-wire proportional chambers with cathodes segmented into strips. The position at which a muon traversed the chamber is obtained by readout electronics. CSCs are used in the innermost end-cap regions ($2.0 < |\eta| < 2.7$) as the particle flux is the highest here, and is beyond the operation rate of MDTs, which is 150 Hz cm^{-2}.

The MS trigger system provides fast response times rather than spatial precision. RPCs are parallel electrode-pate detectors with a 2 mm gas-filled gap. There are two detector layers in each RPC module and three such modules in the barrel region. RPCs provide a spatial resolution of 1 cm and a timing resolution of 1.5 ns. TGCs are multi-wire proportional chambers in the end-cap regions of the MS which trigger on muon tracks as well as provide azimuthal measurements of tracks. They provide a spatial resolution of 2-6 mm and timing resolution of 4 ns.

3.3.6 Trigger and Data Acquisition System

The proton-proton bunch crossing time at the LHC is approximately 25 ns, which converts to a collision frequency of 40 MHz, with 20 collisions per bunch crossing. This event rate is reduced to 1.5 kHz by the trigger and data acquisition (TDAQ) system. The TDAQ works in three stages: the hardware based Level-1 (L1) trigger, the software based Level-2 trigger and event filter. The latter two combine to form the High-Level Trigger (HLT) [5].

The L1 trigger performs initial loose event filtering decision within 2.5 μs of bunch crossing and reduces the event rate from the LHC crossing frequency of 40 MHz to an accept rate of 100 kHz. It consists of the calorimeter trigger (L1Calo), muon trigger (L1Muon), the Central Trigger Processor (CTP) and the Timing, Trigger and Control (TTC) system. The L1Calo accepts signals from the calorimeters to look for electrons, photons, jets, $\tau-$ leptons decaying into hadrons as well as large E_T^{miss}. The L1Muon accepts signals from the muon trigger system to identify high p_T muons. The decision to accept the objects lies with the CTP, which distributes the accept command to the HLT via the TTC [5, 40]. The L1 trigger also identifies regions of detectors in terms of η and ϕ, defined as the Regions of Interest (RoI), which contain possible triggers objects. The information on RoI is also sent to the HLT.

The HLT performs a more refined selection of data by roughly reconstructing physics objects. It receives the information about the RoI's from L1 as well as data from the inner detector. The high precision HLT algorithms use the calorimeters' and muon triggers' data from within the RoI to provide improved threshold energy cuts on particles. Together with track reconstruction information from the inner detector, the HLT enhances particle identification, for e.g., distinction between photons and electrons. The entire operation of the TDAQ is controlled by the online system, while the detector control system monitors the hardware components of the ATLAS detector [5, 41].

3.4 Minimum Bias Trigger

The selection of events by the main trigger system enhances the efficiency of collection for chosen events but also introduces some biasing in the observed rates of particles. Hence, a special trigger called the Minimum Bias Trigger is used to record events with the highest efficiency and lowest biasing possible. Special dedicated runs are carried out each year with the minimum bias trigger to measure fundamental properties like charge multiplicity, rapidity gap etc., which are possible only for events at low luminosity.

The Minimum Bias Trigger Scintillators (MBTS) are thin plastic scintillation counters mounted on the front face of each end cap calorimeter, providing a pseudorapidity range of $2.08 < |\eta| < 3.75$. Minimum bias events are recorded if the particle passes through the ID as well. Thus, the pseudorapidity range is limited to $|\eta| < 2.5$ [42, 43]. Minimum bias is appropriate for types of events where no trigger is defined. It has low rates but enables feasibility studies, thus, can be used for searches for which no dedicated trigger is defined.

Chapter 4

Data Selection

4.1 The decay reconstruction

The analysis focuses on the study of the invariant mass distributions of the $K_s^0K_s^0$, $K_s^0\Lambda^0$ and $\Lambda^0\Lambda^0$ combinations using the ATLAS detector, as explained in the introduction. We assume a possible tetraquark state could be produced in the proton-proton collisions which decays to a pair of K_s^0's. Similarly, a possible pentaquark state could decay into a K_s^0 and a Λ^0, and a possible hexaquark state could decay into a pair of Λ^0's. Furthermore, the neutral strange hadrons K_s^0 and Λ^0 are reconstructed using the decay channels $K_s^0 \rightarrow \pi^+\pi^-$ with a large branching ratio of 0.6920 ± 0.0005 and $\Lambda^0 \rightarrow p^+\pi^-$ with a large branching ratio of 0.641 ± 0.005, respectively [44]. This is shown in Fig. 4.1.

The final decay products are the pions and protons, which allow for the clean reconstruction of the K_s^0 and Λ^0, which are the lightest of strange mesons and baryons, respectively. Both their decay channels are through the weak interactions, which allow for a long decay length. They are each reconstructed from two oppositely charged particle tracks and are defined as the 'secondary' (V^0) vertices, i.e, away from the z-axis. The reconstructed K_s^0 and Λ^0 are then combined in three different ways to further reconstruct possible 'primary' vertices, which are the points of p-p interactions. Any other vertex on the proton-proton collision axis, called the 'pile-up' vertex, needs to be removed.

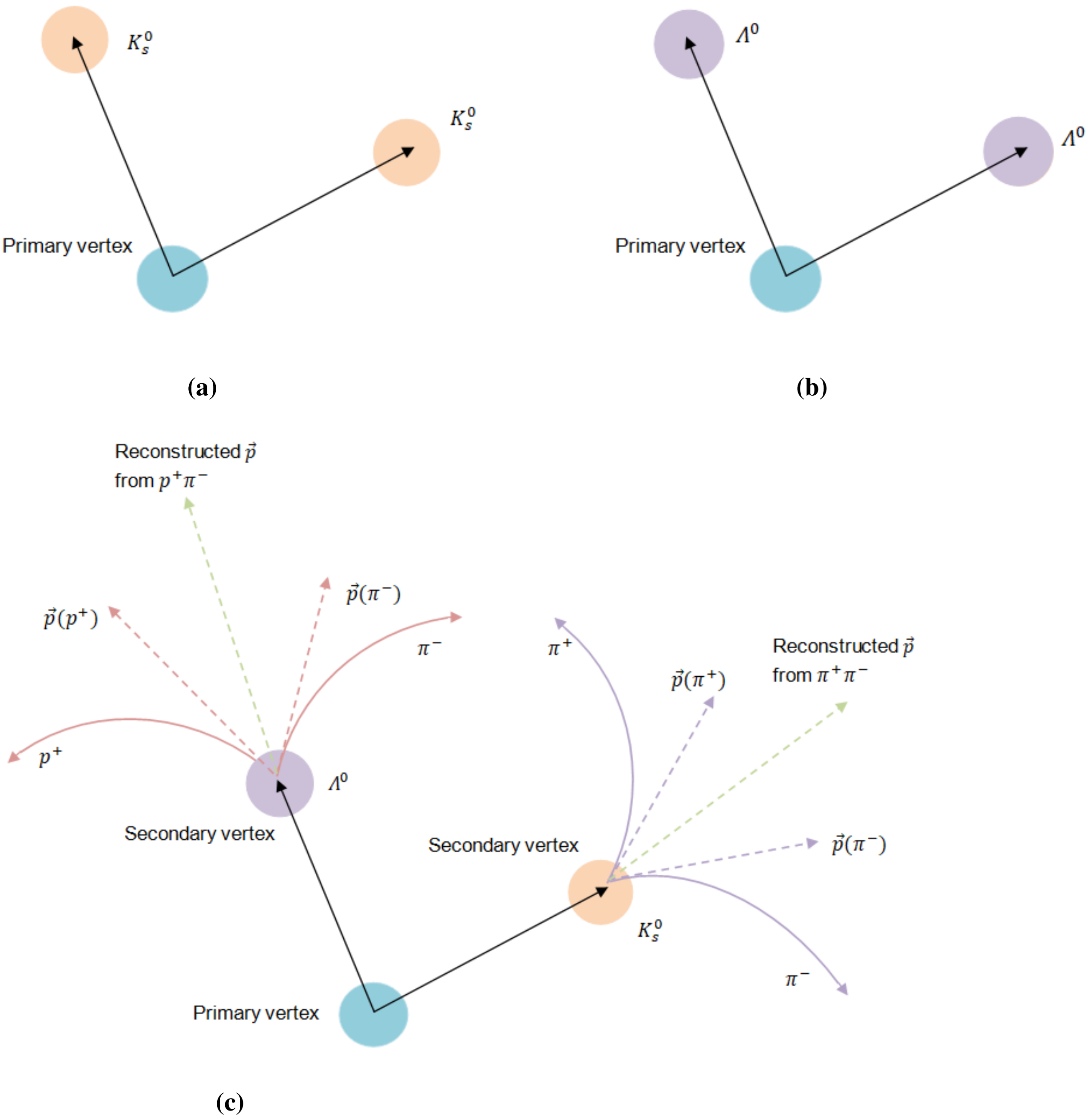

Figure 4.1: Decay channels of possible (a) tetraquark state to a pair of K_s^0's, (b) hexaquark states to a pair of Λ^0's and (c) pentaquark state to a K_s^0 and a Λ^0. (c) further shows the decay channels of K_s^0 and Λ^0.

4.2 Data samples and event selection

This analysis uses Minimum Bias events recorded by the ATLAS detector during the special B1 runs of proton-proton collisions in 2015 at the center-of-mass energy of $\sqrt{s} = 13$ TeV. The data samples from the six B1 runs correspond to an integrated luminosity of $21.559\,nb^{-1}$. The data are collected from the MBTS triggers, explained in Section 3.4, and consist of events with low p_T tracking. Minimum bias events are selected for this study as no other trigger exists for possible multiquark signals, whereas minimum bias events may contain some, which is appropriate for a feasibility study but not optimized for a full search.

The sample is first passed through the Good Runs List '*15_13TeV.periodB1_DetStatus-v62-pro18_DQDefects-00-01-02_PHYS_StandardGRL_All_Good*'. This checks that the events were collected during stable LHC and ATLAS conditions, in this case, during the B1 run of 2015. The event selection is then done such that an event contains only one primary vertex. If present, events with any other vertex on the beam axis, i.e., the 'pile-up' vertex, is removed. Further, for the selection of K_s^0 and Λ^0, events with at least one secondary vertex are selected. Table 4.1 shows the number of events after each cut.

Cut description	Number of events
All Events	202,711,755
Events in Good Runs Lists	196,495,039
Events with a primary vertex	156,986,197
Events with no pile-up vertices	154,658,808
Events with at least one secondary vertex	139,152,132
Events with at least two secondary vertices	50,907,455

Table 4.1: Cut flow for event selection

4.2.1 K_s^0 and Λ^0 selection

The K_s^0 and Λ^0 particles are selected using the V^0 reconstruction algorithm [44, 45]. Vertices are reconstructed such that they originate from two oppositely charged particle tracks and have a neutral track that leads to the primary vertex, with the following basic cuts:

- $|\eta| < 2.5$
- track $p_T > 100$ MeV

The invariant masses are calculated from the 4-momenta of the constituent particles, via the formula:

$$m_0^2 = \left(\sum E\right)^2 - \left\|\sum \mathbf{p}\right\|^2 \tag{4.1}$$

where m_0 is the invariant mass of the decaying particle, $(\sum E)^2$ is the sum of the energies and $\|\sum \mathbf{p}\|^2$ is the vector sum of the momenta of the decay products. In case of K_s^0 the decay products are taken as π^+ and π^- whereas for Λ^0, the decay products are taken as p^+ and π^- (for $\bar{\Lambda}^0$, the decay products are p^- and π^+). Consequently, both tracks for the K_s^0 are assumed to have pion mass. The higher p_T track in the case of Λ^0 (or $\bar{\Lambda}^0$) is assumed to have proton mass as the heavier mass of the proton compared to the pion kinematically takes up a greater part of the Λ^0 momentum at higher momenta.

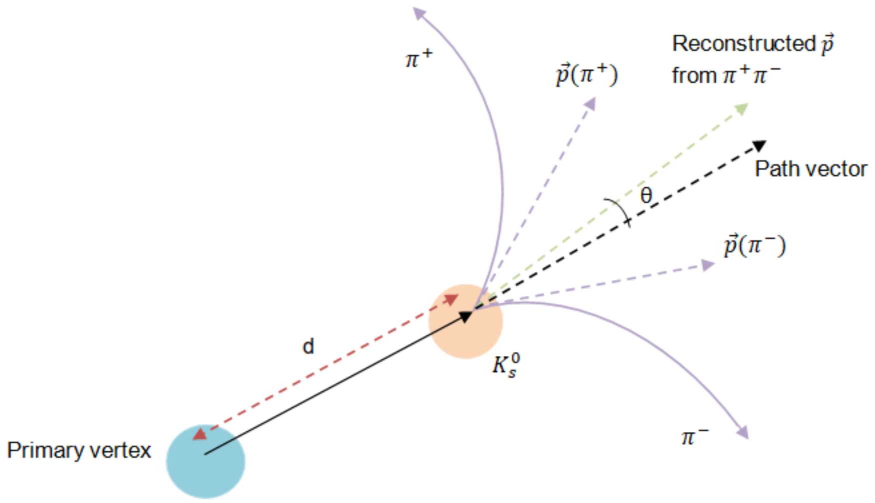

Figure 4.2: Parameters of the decay of a secondary vertex

Particle misidentification, e.g. between the proton and the positively charged pion can cause ambiguity in the reconstructed particle. As a result, this contributes to combinatorial background, which is reduced by applying selection cuts to the following parameters of the decay, also shown in fig. 4.2:

- $\cos\theta$, where θ is the pointing angle between the reconstructed transverse momentum and the path vector of the secondary vertex of interest. The path vector is defined as the line connecting the primary vertex to the secondary vertex.
- d, which is the flight distance of the decaying particle, measured from the primary vertex
- p_T, which is the reconstructed transverse momentum
- Invariant masses of the secondary vertices, i.e, K_s^0 and Λ^0

Following [44], the cuts on the various parameters are estimated. Looser cuts than recommended are taken for the initial selection and are fine-tuned in the later steps of the analysis. It is to be noted that an initial version of one of the data samples, consisting of all vertices, is taken to visualize the cuts on the parameters.

The cosine of the pointing angle, $\cos\theta$, is taken to be greater than 0.9998 ($\approx 1.15^\circ$) as an initial selection, to reduce background as much as possible while also retaining most of the signal. Ideally, $\cos\theta$ would have been zero, which would mean that the reconstructed momentum of the secondary vertex is in line with the path vector from the primary vertex. Due to its sensitivity, it acts as a very efficient background rejection tool. The 1-dimensional projection of $\cos\theta$ is shown in Fig. 4.3 with red line showing where the cut is. The effect of the $\cos\theta$ cut is shown in Fig. 4.4 for both K_s^0 and Λ^0 and is evidently, the strongest cut. The steep drop at about 650 MeV is caused by the limit on the pion's momentum being reached for the calculation of the invariant mass of K_s^0.

Owing to their weak decays, the K_s^0 and Λ^0 have considerably longer lifetimes compared to particles stemming from strong decays and as such, the flight distances are longer too. The distribution of the flight distances are plotted in Fig. 4.5 for both the particles to estimate a cut on them, while their 1-dimensional projections are shown in Fig. 4.6. As can be seen, there is a high background close to the primary vertex, implying that a lot of particles from various decays are produced near the interaction point. A minimum cut of 3 mm for the K_s^0 and 13 mm for the Λ^0 are made. Owing to the longer lifetime of the Λ^0 compared to that of the K_s^0, the minimum cut on

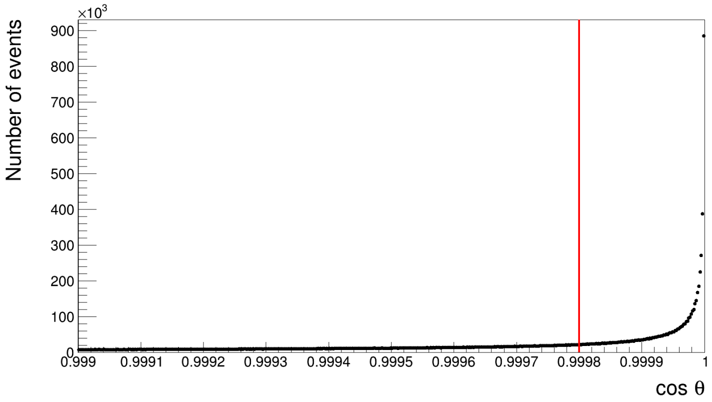

(a)

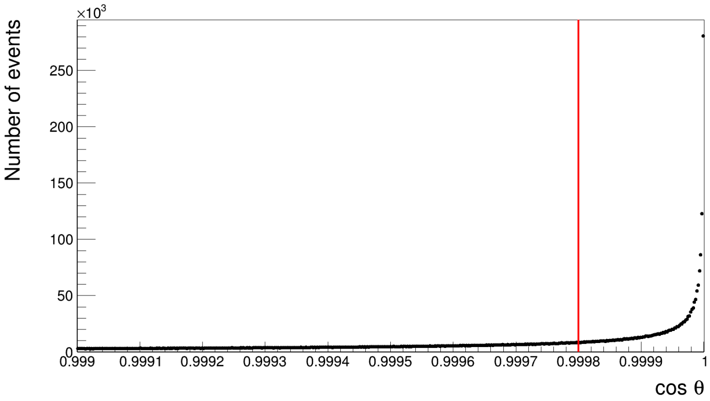

(b)

Figure 4.3: 1-dimensional distribution of $\cos\theta$ with (a) K_s^0 and (b) Λ^0, each showing an initial selection cut at 0.9998.

the distance is also larger. With these, the background near the primary vertex is removed for each particle.

Further, distributions of the reconstructed momentum p_T with respect to the reconstructed masses of K_s^0 and Λ^0 are plotted to estimate the cuts. The reconstructed momentum of the kaon is fairly localized as it is reconstructed symmetrically from two pions, but a loose cut of 300 MeV is still applied to remove some background to the left of the peak, as seen in Fig. 4.7a. The reconstructed momentum of the lambda is estimated to be higher than that of the kaon, as the momentum of a proton track is higher than that of a pion track. At lower momenta, it is difficult to distinguish between a proton and a pion, which contributes to a large background. A minimum,

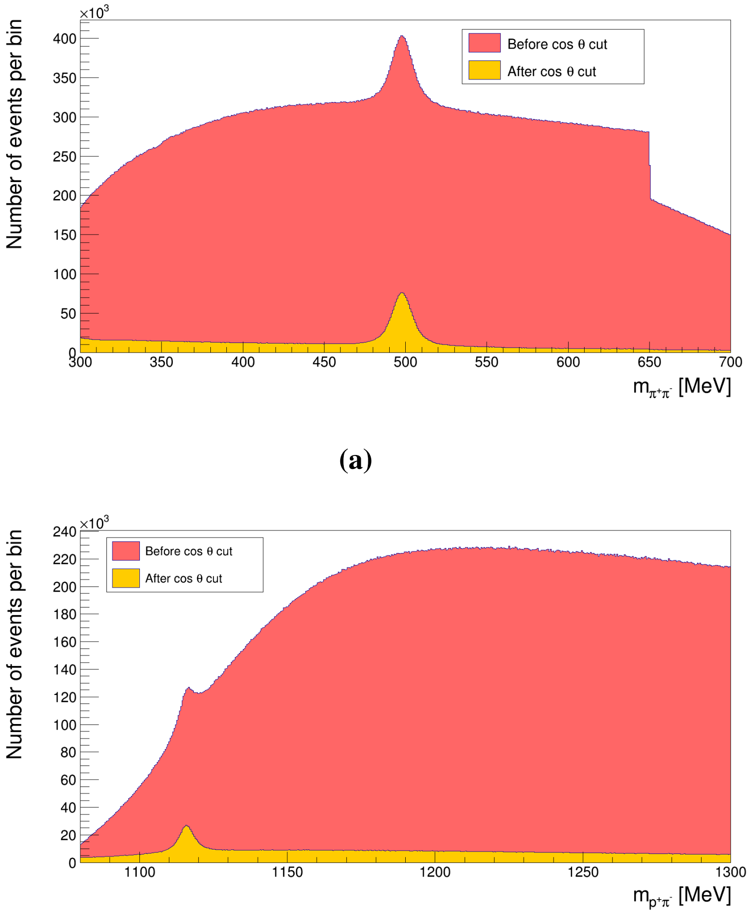

(a)

(b)

Figure 4.4: Effect of the $\cos\theta$ cuts on the invariant mass spectra of (a) K_s^0 and (b) Λ^0. The K_s^0 mass spectrum has a peak at around 500 MeV and the Λ^0 mass spectrum has a peak at around 1115 MeV.

loose cut of 400 MeV is applied which removes much of the background, as can be seen from Fig. 4.7b. The 1-dimensional projections of the p_T of both K_s^0 and Λ^0 are shown in Fig. 4.8, with the loose cuts displayed, which are approximately taken halfway between the maximum and minimum slopes.

The secondary vertex selection applies collectively to both the K_s^0 and Λ^0 candidates, with the difference being only in the magnitude of the cuts on each parameter. To separate the two particles, it is important to identify and compare their invariant masses. As mentioned before, particle misidentification can lead to ambiguous results. To identify the conflict regions, a correlation plot

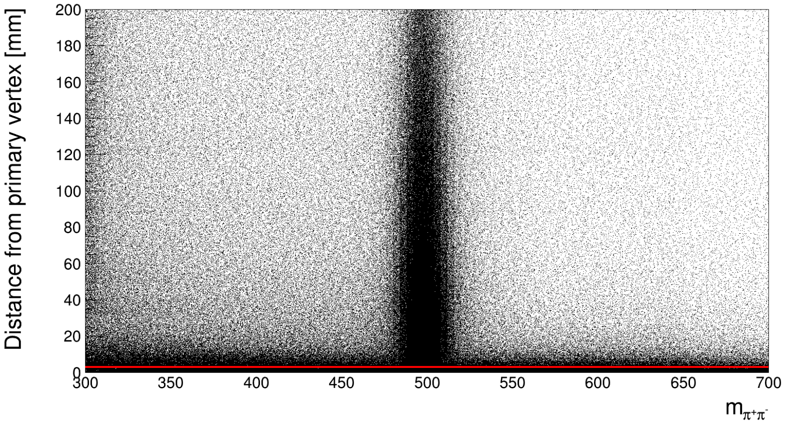

(a)

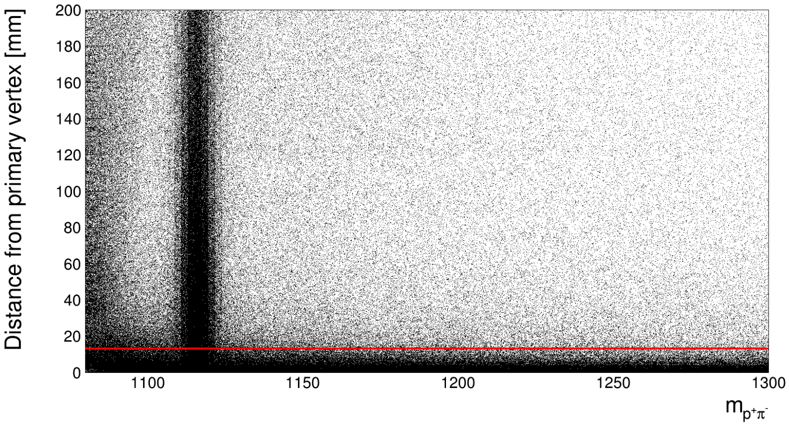

(b)

Figure 4.5: Distribution of the flight distance d as a function of the reconstructed mass of (a) K_s^0 with a cut at 3 mm and (b) Λ^0 with a cut at 13 mm. The points below these cuts are removed.

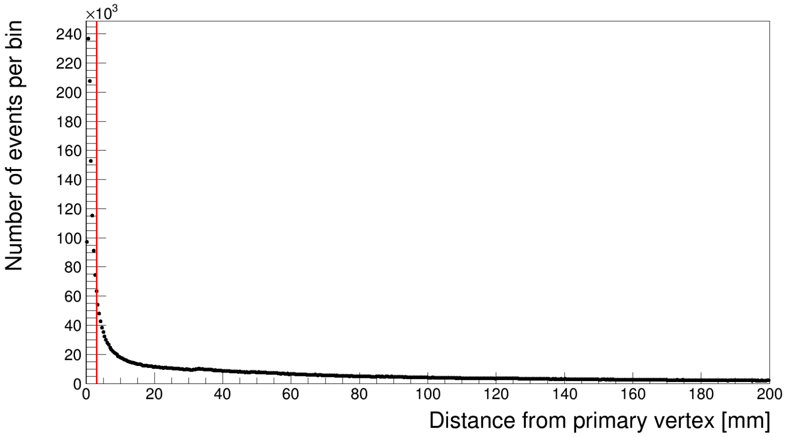

(a)

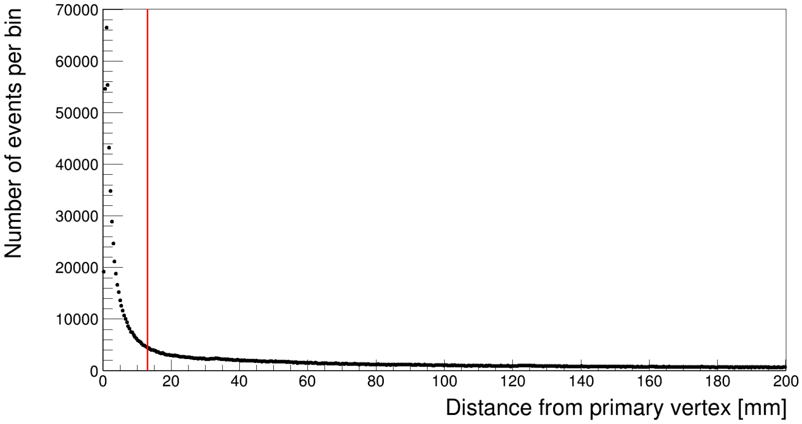

(b)

Figure 4.6: The 1-dimensional distribution of the flight distance d of (a) K_s^0 with a cut at 3 mm and (b) Λ^0 with a cut at 13 mm.

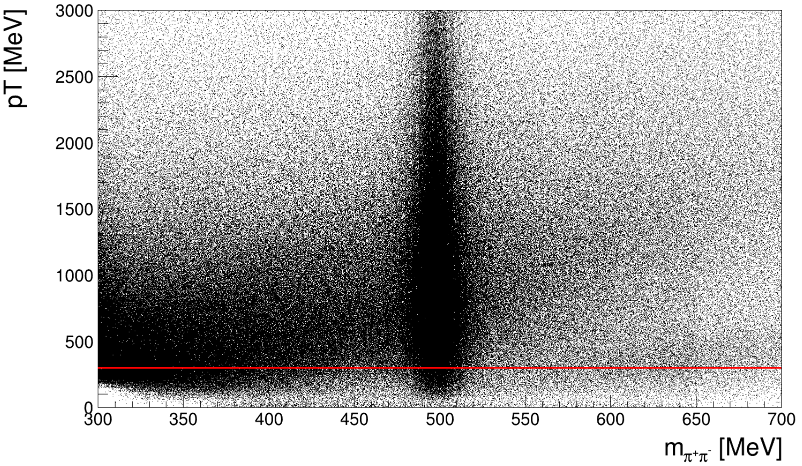

(a)

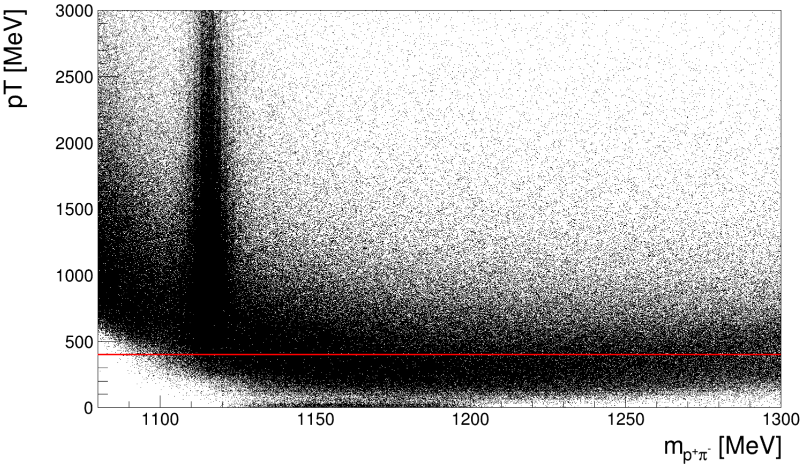

(b)

Figure 4.7: Distribution of the reconstructed transverse momentum p_T as a function of the reconstructed mass of (a) K_s^0 with a cut at 300 MeV and (b) Λ^0 with a cut at 500 MeV. The points below these cuts are removed.

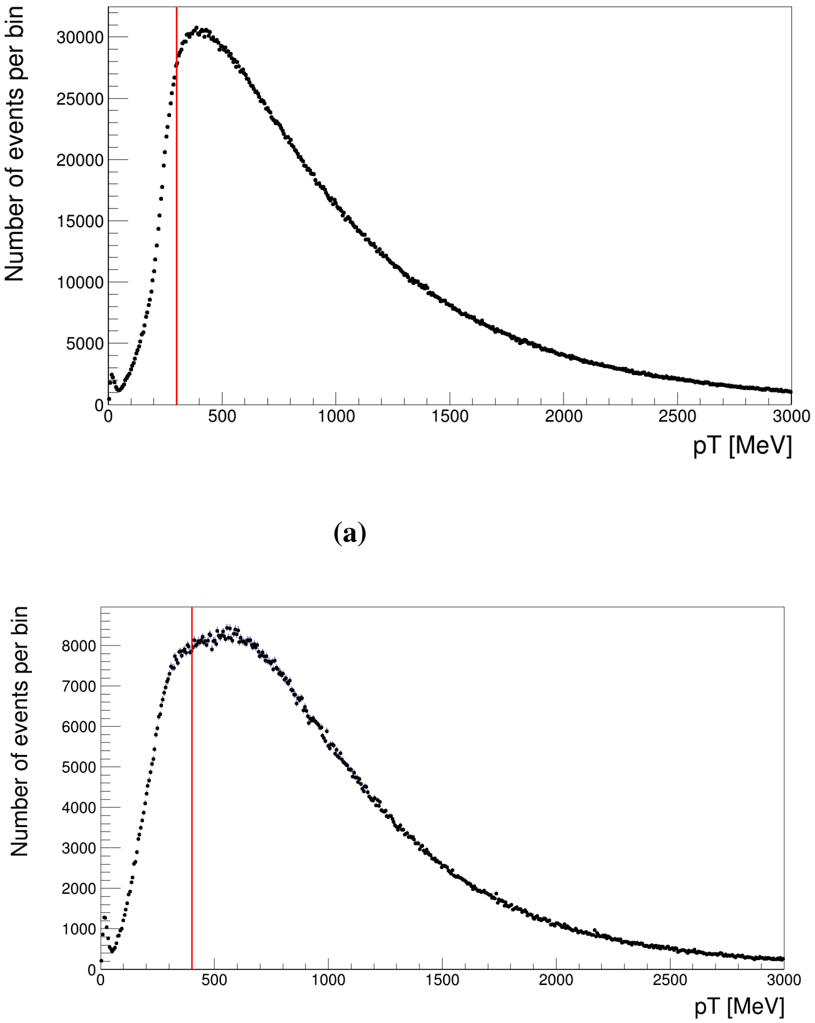

(a)

(b)

Figure 4.8: The 1-dimensional distribution of the transverse momentum p_T of (a) K_s^0 with a cut at 300 MeV and (b) Λ^0 with a cut at 500 MeV.

of the two assumptions is produced. The ambiguity can be clearly seen in Fig. 4.9 where the final states, K_s^0 and Λ^0, mass peaks coincide. Candidates corresponding to this region could be either a K_s^0 or Λ^0. If a proton is misidentified as a pion, the resultant vertex would be a K_s^0 instead of a Λ^0. The lower mass would then show up as background on the invariant mass spectrum of the Λ^0. Similarly, if a K_s^0 is misidentified as a Λ^0 it would contribute as background to the higher end of the K_s^0 invariant mass spectrum. This combinatorial background can be reduced by applying cuts on the invariant masses of the two particles, thus, effectively rejecting the entire region of ambiguity. When K_s^0 is considered, the mass of a Λ^0 is taken to be greater than 1125 MeV. Any Λ^0 candidate below this mass is rejected. When a Λ^0 is considered, the mass of a K_s^0 is taken between 340 MeV and 480 MeV. Any K_s^0 candidate with a mass outside this region is rejected. This selection leads to a loss of a few good candidates, but is required to reduce the combinatorial background. The lower limit cut on the K_s^0 mass is applied to reduce the background which can be seen on the lower left end of Fig. 4.9. This background arises from e^+e^- production and has been studied extensively in [46].

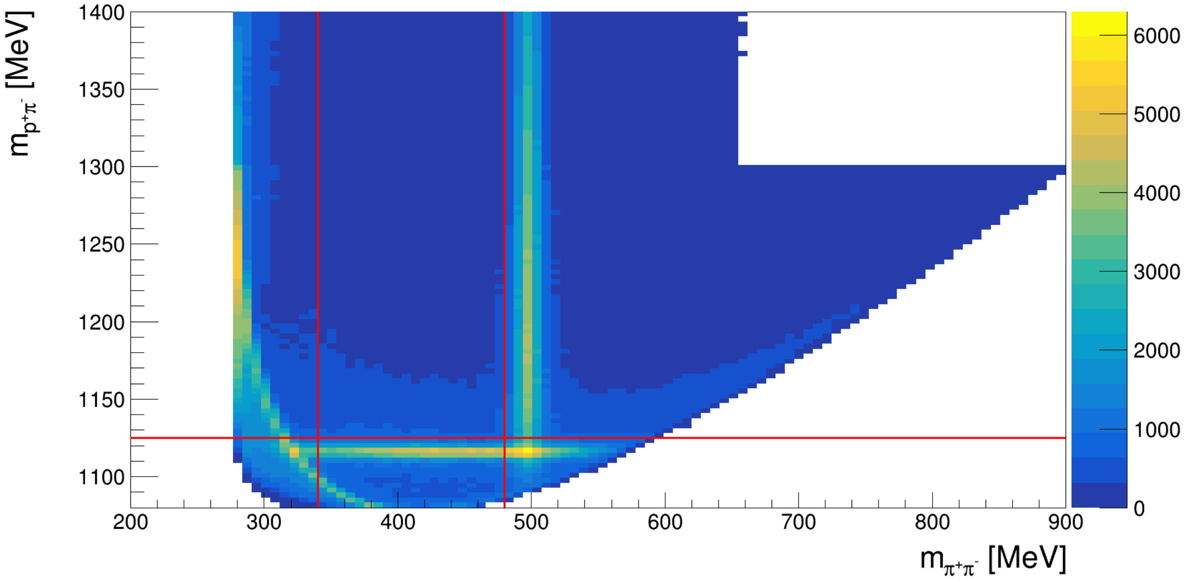

Figure 4.9: Correlation plot of the invariant mass spectra of K_s^0 and Λ^0. When K_s^0 is considered, the Λ^0 mass is taken to be above 1125 MeV, marked by the horizontal line. When Λ^0 is considered, the K_s^0 mass is taken between 340 MeV and 480 MeV, marked by the two vertical lines.

The initial set of the selection cuts is summarized in table 4.2.

Parameter	K_s^0 - Minimum	K_s^0 - Maximum	Λ^0 - Minimum	Λ^0 - Maximum
$\cos\theta$	0.9998	-	0.9998	-
d [mm]	3	-	13	-
p_T [MeV]	300	-	400	-
K_s^0 invariant mass [MeV]	300	700	340	480
Λ^0 invariant mass [MeV]	1125	-	1080	1300

Table 4.2: Initial set of parameter cuts for K_s^0 and Λ^0 candidates

4.2.2 $K_s^0 K_s^0$, $K_s^0 \Lambda^0$ and $K_s^0 \Lambda^0$ selection

The dataset is refined after applying the initial selection cuts. The number of K_s^0 and Λ^0 candidates produced in each event is calculated. Only the events containing two K_s^0 or Λ^0 candidates or one of each, are selected for further procedure. The invariant mass spectra of the combinations are then analyzed to look for possible tetra-, hexa-, or penta-quarks respectively [47]. The invariant mass is calculated using Eq. 4.1.

Chapter 5

Lifetime and Invariant Mass Distributions

5.1 Lifetime distributions of K_s^0 and Λ^0

As the first step of the analysis, the particle identification is verified using the dataset of those events which have at least two K_s^0 and Λ^0 particles. To do so, the lifetime distributions of both particles are plotted. The mean half-life of a particle is calculated from the formula:

$$d = \beta\gamma c\tau, \tag{5.1}$$

where d is the average decay length, $\beta = v/c$ (where v is the velocity of the particle and c is the speed of light), $\gamma = 1/\sqrt{1-\beta^2}$ is the Lorentz factor and τ is the mean half-life. Rearranging the formula and writing it in terms of mass and the total momentum gives:

$$\begin{aligned} \tau &= \frac{d}{\beta\gamma c} \\ &= \frac{d}{v\gamma} \\ &= \frac{dm}{p} \qquad [\because p = \gamma m v] \end{aligned} \tag{5.2}$$

Following this, the flight distance and the total momentum of both particles are considered to calculate the lifetime distributions. The distributions are fitted using the least square (χ^2) method, with a function consisting of two exponentials, one each for describing the signal and the background:

$$f(t) = C_0 + C_B\, e^{r_B t} + C_S\, e^{r_S t}, \tag{5.3}$$

where C_0+$C_B\, e^{r_B t}$ describes the background and $C_S\, e^{r_S t}$ describes the signal [48]. An external study using the data from sidebands in the invariant mass plot of K_s^0 and Λ^0 has shown the background to also have an exponential slope [49]. Tighter cut of $cos\,\theta = 0.9999$ is applied for both particles to further reduce the value of θ. Since the lifetime is related to the parameters d and p_T, the cuts on these parameters are also varied. The variation of cuts for each of the K_s^0 and Λ^0 particle are given in tables 5.1 and 5.2, respectively. The combinations of these parameter cuts which give the best signal-to-noise ratios (SNR), computed from the areas under each curve, with good fits, are taken into final consideration. The final fits results along with the cuts on the parameters are shown in table 5.3.

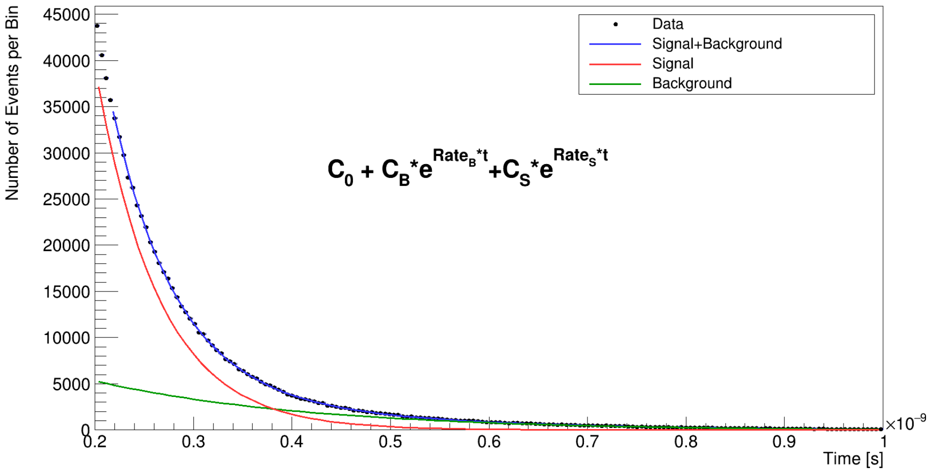

Figure 5.1: Lifetime distribution of K_s^0 with SNR 2.72. The fitted lifetime value is found to be $(6.788 \pm 0.053) \times 10^{-11} (stat)\ s$.

The lifetime distribution plots, with fits corresponding to the ones in table 5.3, are shown in Figs. 5.1 and 5.2. The lifetime values of the K_s^0 and Λ^0 found from the fits and in the Particle Data Group (PDG) [1] are summarized in Table 5.4. The fit values do not include systematic uncertainties

---

[1] The Particle Data Group is an international collaboration of particle physicists which regularly documents and updates published results relating to fundamental particles and interactions.

-	CosThetaMin	DelRMin (mm)	DelRMax (mm)	PtMin (MeV)	PtMax (meV)	MassKMin (MeV)	MassKMax (MeV)	MassLMin (MeV)	MassLMax (MeV)	Lifetime (s)	Error	Lifetime (Background) (s)	Error (background)	Chisq (red)	bkg/sig
PDG Value	-	-	-	-	-	-	-	-	-	8.954E-11	4E-14	-	-	-	-
-	0.9999	4	400	300	2000	475	525	1125		6.7887E-11	5.37224E-13	2.50084E-10	1.03256E-11	1.10753	0.367575
-	0.9999	4	300	400	2000	475	525	1125		5.84594E-11	9.06195E-13	1.20803E-10	3.25332E-12	1.12663	0.520145
-	0.9999	4	300	300	2000	475	525	1125		1.02566E-10	6.59021E-24	2.17965E-10	2.9762E-23	1270.59	16.6254
-	0.9999	3	300	300	2000	475	525	1125		1.02566E-10	6.59021E-24	2.17965E-10	2.9762E-23	1270.59	16.6254
-	0.9998	3	300	300	2000	475	525	1125		5.72587E-11	7.85466E-13	1.29929E-10	2.78521E-12	0.854411	0.645697
-	0.9999	4	300	300	2000	475	525	1125		1.02566E-10	6.59021E-24	2.17965E-10	2.9762E-23	1270.59	16.6254
-	0.9999	5	300	300	2000	475	525	1125		1.02566E-10	6.59021E-24	2.17965E-10	2.9762E-23	1270.59	16.6254
-	0.9999	5	400	300	2000	475	525	1125		6.7887E-11	5.37224E-13	2.50084E-10	1.03256E-11	1.10753	0.367575
-	0.9999	7	400	300	2000	475	525	1125		6.7887E-11	5.37224E-13	2.50084E-10	1.03256E-11	1.10753	0.367575
-	0.9999	10	400	300	2000	475	525	1125		6.7887E-11	5.37224E-13	2.50084E-10	1.03256E-11	1.10753	0.367575
-	0.9999	15	400	300	2000	475	525	1125		6.7887E-11	5.37224E-13	2.50084E-10	1.03256E-11	1.10753	0.367575
-	0.9999	25	400	300	2000	475	525	1125		6.7887E-11	5.37224E-13	2.50084E-10	1.03256E-11	1.10753	0.367575
-	0.9999	25	400	500	2000	475	525	1125		6.73161E-11	5.79276E-13	2.29502E-10	9.28958E-12	1.10635	0.355756
-	0.9999	25	400	600	2000	475	525	1125		2.72368E-11	1.04913E-21	2.22713E-10	7.01462E-20	758.964	9.54428
-	0.9999	25		300	2000	475	525	1125		7.20083E-11	2.33009E-13	9.15078E-09	6.46248E-10	2.36401	0.787711
-	0.9999	4	400	300	2000	475	525	1125		6.7887E-11	5.37224E-13	2.50084E-10	1.03256E-11	1.10753	0.367575
-	0.9999	4		300	2000	475	525	1125		7.20083E-11	2.33009E-13	9.15078E-09	6.46248E-10	2.36401	0.787711
-	0.9999		400	300	2000	475	525	1125		6.7887E-11	5.37224E-13	2.50084E-10	1.03256E-11	1.10753	0.367575
-	0.9999	4	400		2000	475	525	1125		6.7887E-11	5.37224E-13	2.50084E-10	1.03256E-11	1.10753	0.367575
-	0.9999	4	400	300		475	525	1125		6.35762E-11	5.19295E-13	2.19998E-10	6.97257E-12	0.961854	0.430771
-	0.9999	4	400	300		475	525	1125		6.35762E-11	5.19295E-13	2.19998E-10	6.97257E-12	0.961854	0.430771

Table 5.1: Systematic study of the variation of parameter cuts on the K_s^0 lifetime.

-	CosThetaMin	DelRMin (mm)	DelRMax (mm)	PtMin (MeV)	PtMax (meV)	MassKMin (MeV)	MassKMax (MeV)	MassLMin (MeV)	MassLMax (MeV)	Lifetime (s)	Error	Lifetime (Background) (s)	Error (background)	Chisq (red)	bkg/sig
PDG Value	-	-	-	-	-	-	-	-	-	2.632E-10	2E-12	-	-	-	-
-	0.9999	25	600	500		340	480	1100	1130	1.61045E-10	5.31288E-13	4.08696E-08	2.17842E-09	2.08558	0.946083
-	0.9999	25	500	500		340	480	1100	1130	1.62144E-10	5.1551E-13	3.63945E-08	1.72268E-09	1.52866	0.786842
-	0.9999	25	400	500		340	480	1100	1130	1.58252E-10	4.78132E-13	1.39411E-08	1.20972E-10	1.13866	0.619411
-	0.9999	25		500		340	480	1100	1130	1.45615E-10	4.98753E-13	1.02166E-07	6.50018E-09	20.2276	1.84057
-	0.9999	20	500	500		340	480	1100	1130	1.62144E-10	5.1551E-13	3.63945E-08	1.72268E-09	1.52866	0.786842
-	0.9999	20	400	500		340	480	1100	1130	1.58252E-10	4.78132E-13	1.39411E-08	1.20972E-10	1.13866	0.619411
-	0.9999	20	700	500		340	480	1100	1130	1.58839E-10	5.11268E-13	4.68078E-08	2.27934E-09	3.30123	1.09278
-	0.9999		400	500		340	480	1100	1130	1.58252E-10	4.78132E-13	1.39411E-08	1.20972E-10	1.13866	0.619411
-	0.9999		500	500		340	480	1100	1130	1.62144E-10	5.1551E-13	3.63945E-08	1.72268E-09	1.52866	0.786842
-	0.9999	25	400			340	480	1100	1130	1.58627E-10	4.85587E-13	1.39629E-08	1.27836E-10	1.03693	0.643869
-	0.9999	25	400	600		340	480	1100	1130	1.5619E-10	4.6577E-13	3.4525E-08	2.33355E-09	1.54926	0.588207
-		25	400	500		340	480	1100	1130	1.61246E-10	4.51687E-13	3.85265E-08	1.30684E-09	1.60047	0.72342
-	0.9999	25	400	500		340	480	1100	1130	1.58252E-10	4.78132E-13	1.39411E-08	1.20972E-10	1.13866	0.619411
-	0.9999	20	400	500		340	480	1100	1130	1.58466E-10	4.6979E-13	1.23072E-08	9.64859E-11	1.14726	0.612231
-	0.9999	15	400	500		340	480	1100	1130	1.58466E-10	4.6979E-13	1.23072E-08	9.64859E-11	1.14726	0.612231
-	0.9999	30	400	500		340	480	1100	1130	1.58466E-10	4.6979E-13	1.23072E-08	9.64859E-11	1.14726	0.612231
-	0.9999	30	400	600		340	480	1100	1130	1.56675E-10	4.58729E-13	2.88417E-08	2.62984E-09	1.38369	0.582571
-	0.9999	20	400	600		340	480	1100	1130	1.56675E-10	4.58729E-13	2.88417E-08	2.62984E-09	1.38369	0.582571
-	0.9999	25	400	400		340	480	1100	1130	1.58739E-10	4.71245E-13	1.2275E-08	1.01711E-10	1.15897	0.633316
-	0.9999	20	400	400		340	480	1100	1130	1.58739E-10	4.71245E-13	1.2275E-08	1.01711E-10	1.15897	0.633316

Table 5.2: Systematic study of the variation of parameter cuts on the Λ^0 lifetime.

Particle	K_s^0	Λ^0
$\cos\theta$	0.9999	0.9999
Minimum d [mm]	4	25
Maximum d [mm]	400	400
Minimum p_T [MeV]	300	500
Maximum p_T [MeV]	2000	-
Signal lifetime [$\times 10^{-10}$ s]	0.678 ± 0.005	1.582 ± 0.005
Background lifetime [$\times 10^{-10}$ s]	2.500 ± 0.103	139.411 ± 1.209
χ^2_{red}	1.10	1.14
SNR	2.72	1.61

Table 5.3: Lifetime fits results for K_s^0 and Λ^0.

and hence, are not compatible with the PDG values. However, a better modelling of the background is expected to give results closer to the PDG values. Systematic studies for the lifetime distributions are not included as they are not crucial to this analysis. However, they are required as they give better estimates on the lifetime values and reduce background more efficiently. As such, studies on the same are being conducted separately [49].

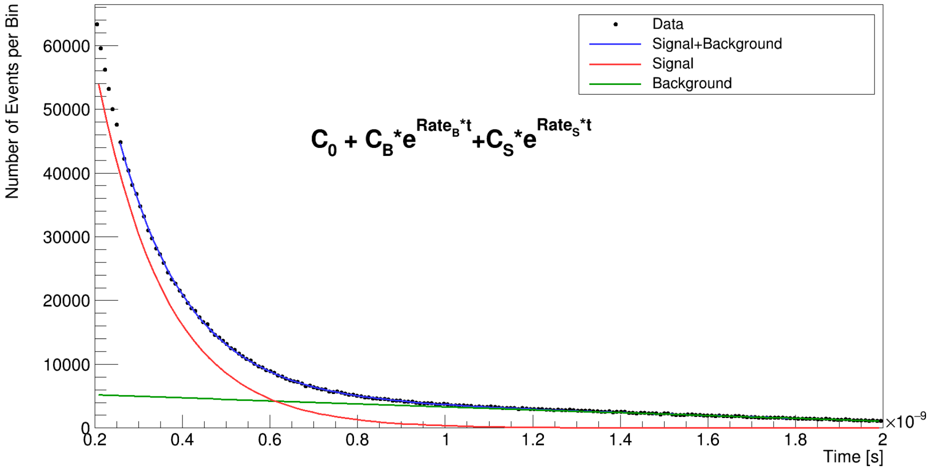

Figure 5.2: Lifetime distribution of Λ^0 with SNR 1.61. The fitted lifetime value is found to be $(1.583 \pm 0.005) \times 10^{-10} (stat)\ s$.

Particle	Lifetime from fit [$\times 10^{-10}$ s]	Lifetime PDG 2022 values [$\times 10^{-10}$ s]
K_s^0	$0.678 \pm 0.005\ (stat)$	0.8954 ± 0.0004
Λ^0	$1.583 \pm 0.005\ (stat)$	2.632 ± 0.020

Table 5.4: Lifetime values from this analysis and PDG 2022.

5.2 Invariant mass distributions of K_s^0 and Λ^0

Finally, the invariant mass distributions of both K_s^0 and Λ^0 are investigated such that all K_s^0 from the $K_s^0 K_s^0$ and $K_s^0\Lambda^0$ channels, and all Λ^0 from the $\Lambda^0\Lambda^0$ and $K_S^0\Lambda^0$ channels are included. They are fitted with a simple function, comprising a single-Gaussian model to describe the signal and a linear polynomial to describe the background.

$$f(x) = h \exp\left(-\frac{(x-\mu)^2}{2\sigma^2}\right) + c_0 + c_1 x, \tag{5.4}$$

where h is the height of the Gaussian, μ and σ are the mean and standard deviation respectively, and $c_0 + c_1 x$ is the linear polynomial.

The tail of each of the mass peak of K_s^0 and Λ^0 is only approximately fitted in case of the single-Gaussian model. Even so, the single-Gaussian is preferred for the purpose of estimation of the mean and width of the mass peaks. The masses of the K_s^0 and Λ^0 found from the fits are summarized in Table 5.5. The range of the invariant mass distribution for Λ^0 is limited to 1100-1600 MeV for better modelling of the background. The SNR for K_s^0 is found to be 2.56 between 400-600 MeV while that for the Λ^0 is found to be 2.77 between 1100-1160 MeV. They differ a bit from the SNR of lifetime distributions due to the slight difference in mass ranges.

The width, σ, of the K_s^0 mass peak is found to be 6.7 MeV, while that of the Λ^0 is found to be 2.6 MeV. These numbers provide a good estimate on the cuts to be applied to the respective masses of the K_s^0 and Λ^0 particles, which is $\pm 3\sigma$ around the mean of each peak. This specific cut is chosen for each particle, as the data within 3σ on either side of the peak retains 99.7% of the signal efficiently and as such this cut provides the best balance between signal versus background

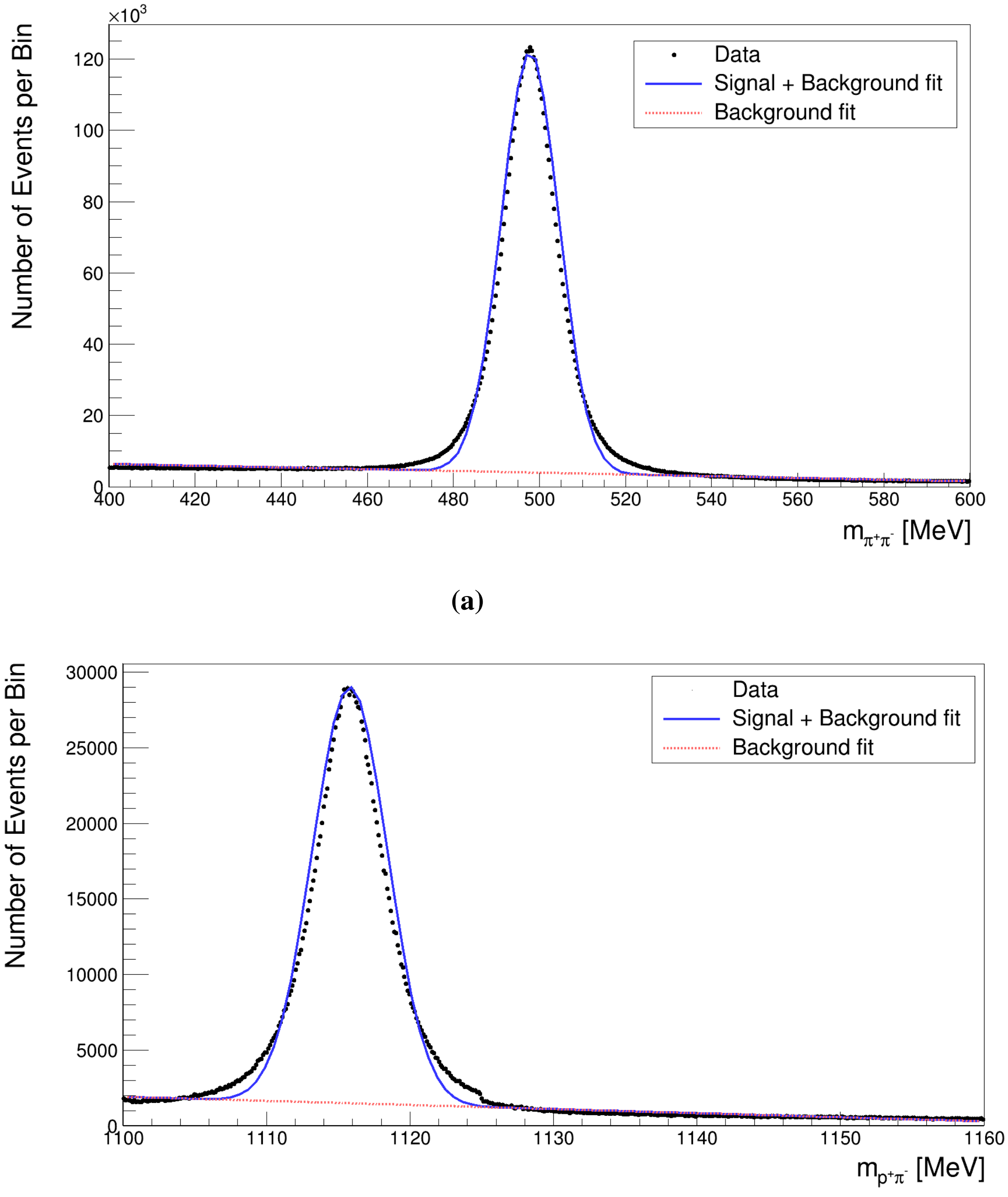

(a)

(b)

Figure 5.3: Invariant mass distribution of (a) K_s^0 with SNR 2.56 and (b) Λ^0 with SNR 2.77. An approximate fitting is done to estimate the peak of the distributions, which is found at (497.803 ± 0.002 (*stat*) MeV for the K_s^0 and at 1115.820 ± 0.002 (*stat*) MeV for the Λ^0. Both distributions are fitted with a single-Gaussian function for the signal and a linear polynomial for the background.

events. This translates to tighter mass cuts of 478 - 518 MeV for the K_s^0 and 1108 - 1124 MeV, as can be seen in table 5.6.

Particle	Mass from single-Gaussian fit (MeV)	Mass PDG 2022 values (MeV)
K_s^0	497.803 ± 0.002 (*stat*)	497.611 ± 0.013
Λ^0	1115.820 ± 0.002 (*stat*)	1115.683 ± 0.006

Table 5.5: Mass values from this analysis and PDG 2022.

The single-Gaussian fit provides a good estimate of the numbers required for tighter mass cuts. However, a better fit of the tails of the mass peaks of both K_s^0 and Λ^0 have been obtained by describing the peak using a double-Gaussian model, as included in Appendix A.

The set of final cuts obtained from the above analyses is thus presented:

Parameter	K_s^0 - Minimum	K_s^0 - Maximum	Λ^0 - Minimum	Λ^0 - Maximum
$\cos\theta$	0.9999	-	0.9999	-
d [mm]	4	400	25	400
p_T [MeV]	300	2000	500	-
K_s^0 invariant mass [MeV]	478	518	340	480
Λ^0 invariant mass [MeV]	1125	-	1108	1124

Table 5.6: Final set of parameter cuts for K_s^0 and Λ^0 candidates

After applying the final selection cuts, the number of events in the $K_s^0K_s^0$, $K_s^0\Lambda^0$ and $\Lambda^0\Lambda^0$ combinations are given in table 5.7.

Channel	Number of events
$K_s^0K_s^0$	1,587,069
$K_s^0\Lambda^0$	420,742
$\Lambda^0\Lambda^0$	232,617

Table 5.7: Statistics of the three channels after applying final selection cuts

Chapter 6

$K_s^0 K_s^0$ Invariant Mass

This chapter focuses on the search for lower energy resonances in the $K_s^0 K_s^0$ channel previously observed by the ZEUS and L3 experiments, which have been discussed in section 2.3.

6.1 The $K_s^0 K_s^0$ channel

The selection criteria used to reconstruct the $K_s^0 K_s^0$ candidates is discussed in section 4.2.2. The final cuts obtained from table 5.6 are applied to each of the K_s^0's and the invariant mass distribution of $K_s^0 K_s^0$ is investigated. Fig. 6.1 shows the full range of the invariant $K_s^0 K_s^0$ mass distribution. A peak at around 1000 MeV can be seen here, which is a consequence of the selection cuts from table 5.6 made on the individual K_s^0 and is not a real state. In this chapter, the range 1200-2700 MeV is considered. The upper limit is the same as had been previously considered by C. Zhou [4]. The lower limit is so chosen to exclude the peak at about 1000 MeV and the steep gradient below.

6.2 Search for lower energy resonances

6.2.1 Statistics

The lower mass range of $K_s^0 K_s^0$ is investigated using RooFit [50]. An extended maximum likelihood fit is performed on the data, which is described as a composite model $M(x)$ constructed from a signal model $S(x)$ and background model $B(x)$ as:

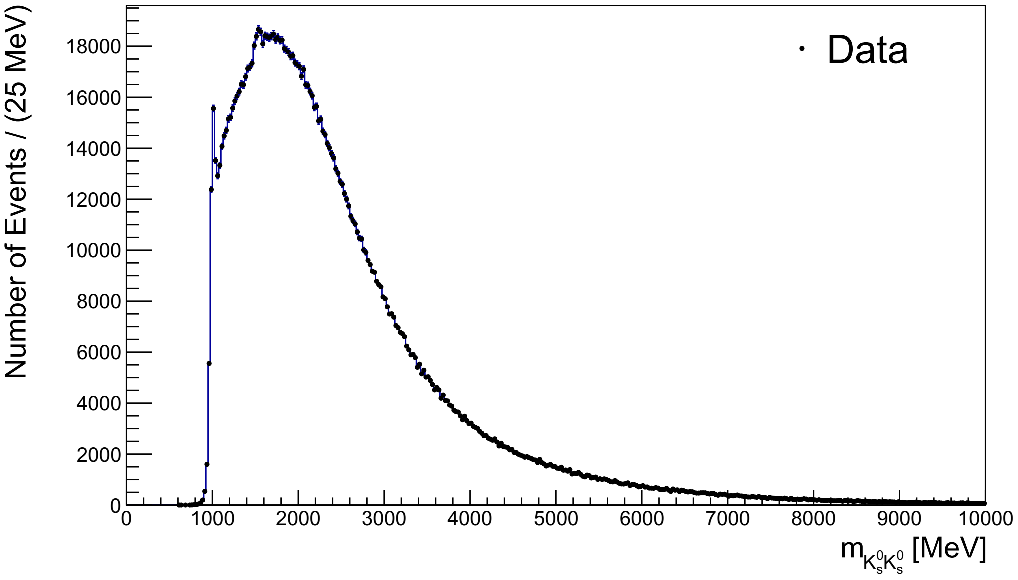

Figure 6.1: Invariant mass distribution of $K_s^0 K_s^0$

$$M_E(x) = N_S S(x) + N_B B(x) \tag{6.1}$$

where $M_E(x)$ is a probability distribution function, not normalized to 1, but rather to $N_S + N_B = N$, the observed number of events in the data. The shape of the distribution and the expected number of events can be obtained if M is considered as [51]:

$$M(x) = \left(\frac{N_S}{N_S + N_B}\right) S(x) + \left(\frac{N_B}{N_S + N_B}\right) B(x), \text{ and} \tag{6.2}$$

$$N_{exp} = N_S + N_B \tag{6.3}$$

The likelihood function L for observables $\vec{x}$ and parameters $\vec{p}$, in the extended case, is defined as

$$L(\vec{p}) = \prod_{data} M(\vec{x}; \vec{p}) \cdot Poisson(N_{exp}, N_{obs}) \tag{6.4}$$

where N_{obs} comes from the data, and the best fit parameters are obtained by maximizing the likelihood L, or minimizing the negative log likelihood (NLL) as:

$$\left.\frac{\partial \ln L(\vec{p})}{\partial \vec{p}}\right|_{p=\hat{p}} = 0 \tag{6.5}$$

In this case, $\vec{x}$ is the data being fit, which is the $K_s^0 K_s^0$ mass and the parameters $\vec{p}$ are the parameters of the fit model describing the background and the signal, elaborated in the next section.

6.2.2 Fit to $K_s^0 K_s^0$ mass

The first fit model used to describe the data consists of a single-gaussian model for the signal and a third degree Chebyshev polynomial for the background:

$$M_E(x) = N_S \, Gauss(x, \mu, \sigma) + N_B \, Cheb3(x) \tag{6.6}$$

The mean of the gaussian is found to be at 1535.19 ± 5.46 MeV and the width is found to be 28.57 ± 5.18 MeV, shown in Fig. 6.2. Approximately 1899 signal events are obtained from the fit with an error of 362 events. This results in $> 5\sigma$ significance, which in particle physics, is a positive signal. Thus, it is concluded that a state at 1535 MeV has been observed, which can be assumed to be the $f_2'(1525)$ tensor meson. The reduced χ^2 of the fit is 1.26. A better fit in the 1200-1500 MeV range could be used to describe the residual structures, which could possibly be arising from the peaks, $f_2(1270)$ and $a_2(1320)$ shown in Fig. 2.3.

Another fit model using a non-relativistic Breit Wigner (BW) distribution for the signal peak has been used to describe the data:

$$f(x, x_0, \gamma) = \frac{1}{\pi\gamma}\left[\frac{\gamma^2}{(x - x_0)^2 + \gamma^2}\right] \tag{6.7}$$

where x_0 is the mean of the peak and 2γ is the full width at half maximum (FWHM). This is the most commonly used distribution for modelling resonant peaks, as it is similar to the relativistic BW function which in turn arises from the propagator of an unstable particle [52, 53]. The background model remains the same as the previous fit, as shown in Fig. 6.3. The motivation for this fit arises

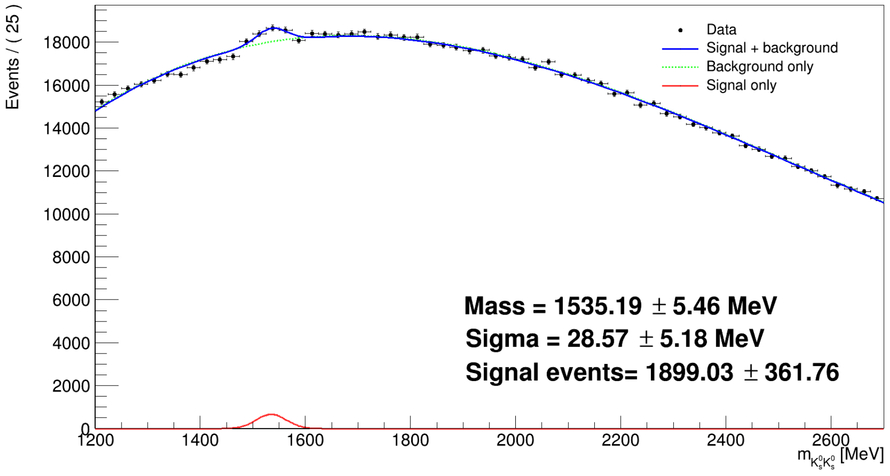

Figure 6.2: Invariant mass distribution of $K_s^0K_s^0$ in the range of 1200-2700 MeV

from the fact that previous experiments have used the BW fit to describe the resonant peaks in the $K_s^0K_s^0$ spectrum. The reduced χ^2 of this fit is 1.33. In this case, the mean of the peak is fitted to be at 1541.28 ± 5.25 MeV. A peak is observed, with FWHM of 52.32 ± 11.87 MeV. The FWHM is ~2.3 times the standard deviation, σ, which gives the width of the peak to be 22.74 ± 5.16 MeV. The statistical significance of the signal is found to be 2423/459 $\approx$ 5, which corresponds to ‘discovery’, i.e. clear confirmation of the observation of the resonance, as can be seen in Fig. 6.3.

No other resonant states like $f_J(1710)$, $a_2^0(1320)$ or $f_2(1270)$ have been observed, and it would be helpful to analyze more statistical data in order to look for those states. The two fits are only used for comparisons and neither fit produces a good enough result for the exact measurement of the resonant states. The fact that a resonant state, presumably $f_2'(1525)$, is observed provides a proof of principle of calibration to further look at higher energy range for possible multiquark states.

6.2.3 Comparison with other experiments

The results obtained for the $f_2'(1525)$ state in the previous section are compared with the results obtained by other experiments, such as ZEUS and L3. In table 6.1, the first two rows show the statistics obtained by the two fits in this analysis.

The third row shows the results obtained by C. Zhou with the ZEUS data collected in the HERA (Hadron Electron Ring Accelerator) particle accelerator from *ep* collisions. As shown in Fig.

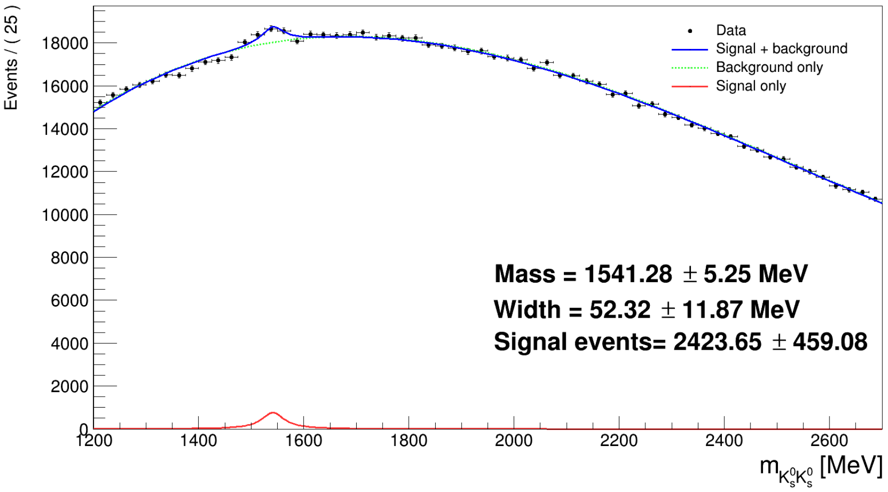

Figure 6.3: Invariant mass distribution of $K^0_sK^0_s$ in the range of 1200-2700 MeV; Breit Wigner fit

Comparison for $f_2'(1525)$	Mass	Width
Single gaussian fit	1535.19 ± 5.46	28.57 ± 5.18
Breit Wigner fit	1541.28 ± 5.25	22.74 ± 5.16
ZEUS Incoherent BW (C. Zhou)	$1523 \pm 3^{+2}_{-8}$	$71 \pm 5^{+17}_{-2}$
L3 Incoherent BW	1523 ± 6	100 ± 15
PDG 2022 values	1517.4 ± 2.5	86 ± 5

Table 6.1: Comparison of $f_2'(1525)$ results from different fits and experiments

4.1a, three resonant peaks, $f_2(1270)/a^0_2(1320)$, $f_2'(1525)$ and $f_J(1710)$ are obtained in the $K^0_sK^0_s$ spectrum in the ZEUS analysis. Two individual fits, incoherent and coherent BW functions, are used to describe the spectrum. The difference between the two is that the incoherent BW function does not take into account the interference among the three states [4] whereas the coherent BW does. Since no state other than the one assumed to be $f_2'(1525)$ is observed in this ATLAS analysis, interference is not taken into account. Hence, the results of this analysis are only compared to the result from the incoherent BW fit of the ZEUS analysis. The mean values of both fits in this ATLAS analysis are higher than the one obtained in the ZEUS analysis, while the width values are much lower.

The fourth row shows the results from the L3 analysis carried out in the LEP (large Electron-Positron) collider via the process $\gamma\gamma \rightarrow K_s^0 K_s^0$ [3]. A maximum likelihood fit consisting of three BW functions for the peaks and a second order polynomial for the background is used to describe the entire spectrum. The previously-mentioned three resonant states can be clearly seen in Fig. 4.1c. The interference among the states had not been taken into account in the L3 analysis. The mean values of $f_2'(1525)$ are once again seen to be higher than the one in the L3 analysis, and the width values, lower.

Finally, the latest PDG results for the $f_2'(1525)$ state are included in the last row of the table. It is to be noted that the PDG values include both statistical and systematic errors while the fits in the ATLAS analysis include only statistical errors.

6.2.4 Discussion

The search for previously-observed low energy states is an interesting prospect as it provides validation to the data currently investigated. The presence of a resonant state at ~1535 MeV indeed validates that the $K_s^0 K_s^0$ invariant mass has been correctly reconstructed. This automatically extends to the $K_s^0 \Lambda^0$ and $\Lambda^0 \Lambda^0$ masses since the same method has been used for their reconstruction. However, since other states have not been observed, more studies need to be done to understand the background, and it will be beneficial to use the rest of the Run-2 data for the same as they would provide more statistics. It also provides a proof of calibration of the ATLAS detector since the mean of the mass peak is close to what has been observed before (ref. to table 6.1). Thus, overall it gives a proof of principle as a part of the feasibility study. It is also required to have a closer look at the low energy ranges of the other distributions, i.e, $K_s^0 \Lambda^0$ and $\Lambda^0 \Lambda^0$.

Since the resonant states were already known, the mean and width of the state could be approximated before fitting in this case, and later fine-tuned. To look for resonances at higher energies, a bump searching is done across the entire range which is discussed in the next chapter.

Chapter 7

Search for multiquark states

The observation of a resonant state, assumed to be the $f_2'(1525)$ meson validates the reconstruction of the $K_s^0 K_s^0$ mass spectrum. The next step is to look for resonant states in the higher energy range of the same spectrum and extend the search methods to the other two spectra, namely, $K_s^0 \Lambda^0$ and $\Lambda^0 \Lambda^0$. This chapter goes into the details of the bump searching method on all the three spectra and the interpretation of the results obtained.

7.1 Bump hunting technique

There are different statistical tests devised to look for the presence of local data excess as a result of resonant production, commonly referred to as 'bumps'. This analysis is based on a simple hypothesis test, where the null hypothesis, H_0, is described by the background processes and the alternative hypothesis, H_1, is described by the background plus the signal that is being searched for. Since it is a data-driven analysis, no Monte Carlo (MC) simulations are used to describe H_0. Instead, a background fit is performed on the data which accounts for H_0. A single-Gaussian function for the signal is described over the background fit, which acts as H_1 here, that is used to look for significance. The test is conducted on each bin and the level of agreement with H_0 is measured quantitatively by computing a $p-$value. The $p-$value is the probability of finding data of greater incompatibility with the predictions of H_0, when H_0 is assumed to be true. If the fluctuation of a single bin is significant, the null hypothesis is ruled out even if it were true. Thus, each bin is considered a trial that could potentially lead to a discovery. All these trials need to be considered during the search which is referred to as the trials factor. To reduce the possibility of a false discovery, all trial factors are considered using a hypertest which, by definition, means a combination of other hypothesis sets. In this analysis, the hypothesis test is conducted on each of the individual bins in a specific, restricted range of the spectrum. This bin by bin test is done iteratively for bin widths from 5 MeV to 100 MeV, increased in steps of 5 MeV. The union of these individual hypothesis tests form the hypertest, which increases the sensitivity of the search method [54, 55].

7.1.1 Significance estimation

In this analysis, the incompatibility mentioned in Section 7.1 is measured based on the number of signal events. In particle physics, the $p-$value is converted into an equivalent significance, Z, and is expressed in units of the standard deviation (σ). It is defined such that a Gaussian distributed variable found Z standard deviations above its mean has an upper-tail probability of p:

$$Z = \Phi^{-1}(1 - p), \tag{7.1}$$

where Φ is the quantile (inverse of cumulative distribution) of the standard Gaussian. A discovery is stated when the statistical significance is equal to or greater than 5σ, which corresponds to $p = 2.87 \times 10^{-7}$. A possible observation is stated when the statistical significance is equal to or greater than 3σ.

Here, the significance in terms of σ is calculated using the number of events under the Gaussian signal divided by the standard deviation of the measurement. The significance on either side of zero is considered as any excess or deficit from the background can hint towards the presence of a resonant state. To look for excesses (or deficits), the Gaussian signal for any test is assumed to span three bins, with its mean centred on the n^{th} bin and its tails extending up to the $(n-1)th$ and $(n+1)th$ bins. The bin width is increased in steps of 5 from 5 to 100 MeV for each fit, which is equivalent to increasing the width of the gaussian signal over more than three bins.

7.2 $K_s^0 K_s^0$ channel

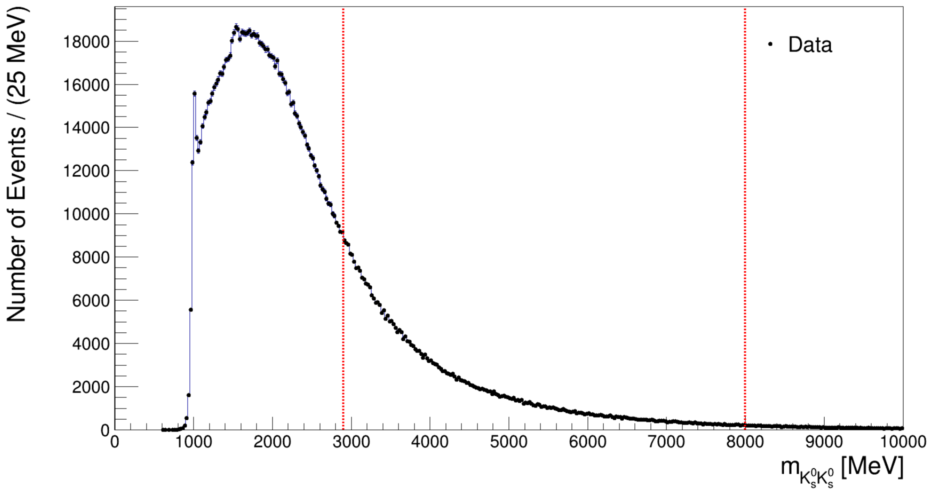

Figure 7.1: Invariant mass distribution of $K_s^0 K_s^0$, marked with the region investigated for possible multiquark states. Same as Fig. 6.1, but with range of search included.

The $K_s^0 K_s^0$ channel is investigated using the bump searching method described earlier. The range 2900-8000 MeV is considered, motivated by Fig. 2.4, as most of the multiquark structures observed by other experiments falls within this rang. Moreover, as seen from Fig. 7.2, beyond 8000 MeV, the number of events in every 5 MeV bin falls below 50, which can increase the error on the signal significance. The data in this range is described by a background fit of the form:

$$f(x) = \text{Exp}(a_0 + a_1 x + a_2 x^2 + a_3 x^3) \tag{7.2}$$

which acts as the null hypothesis, H_0. A polynomial in the exponential form is preferred over a simple polynomial for the background estimation as it is better behaved, gives a better reduced χ^2 value and converges for all bin widths. The $K_s^0 K_s^0$ spectrum along with the background fit is shown in Fig. 7.2. The reduced χ^2 of the fit is 1.05. The parameters found from this fit are then fixed to prevent the introduction of any fitting biases of a Gaussian signal, as described in Section 7.1.1, which is introduced on top of the fixed background. The signal significance obtained from the hypothesis test is shown in Figs. 7.3 for 5 MeV binning and 7.4 for binnings of 25 MeV, 50 MeV, 75 MeV and 100 MeV. The plots for the rest of the bin widths are included in Appendix B.1.

The bin widths could be well extended to beyond 100 MeV but since no hints of a peak had been observed in these bins, the study was stopped at 100 MeV. Previously observed exotic states have measured widths mostly within the range of 5-100 MeV [56].

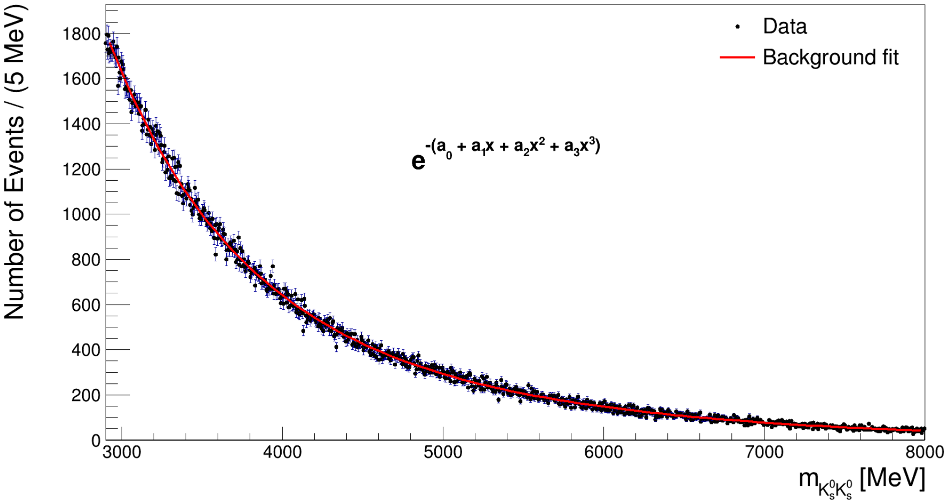

Figure 7.2: Higher range of invariant mass distribution of $K_s^0 K_s^0$ with background fitting

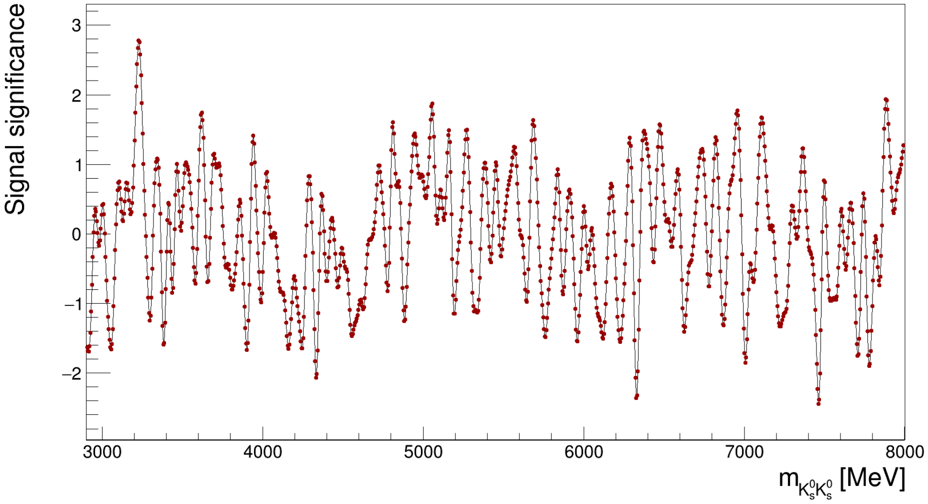

Figure 7.3: Significance plot of $K_s^0 K_s^0$ for binning of 5 MeV

It is evident from the plots that no significance equal to or greater than 3σ is obtained which means no resonant state has been discovered, or even observed, in the $K_s^0 K_s^0$ spectrum.

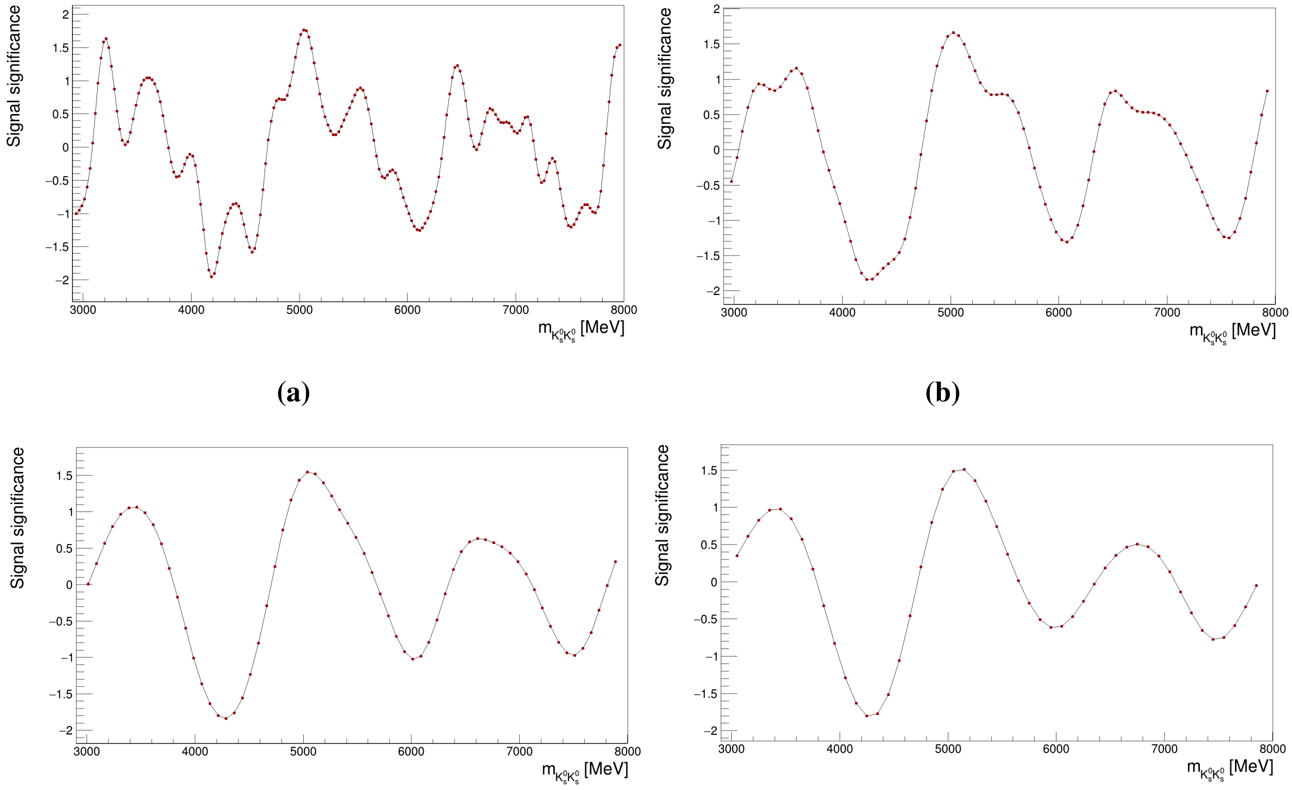

(a)

(b)

(c)

(d)

Figure 7.4: Significance plots of $K_s^0K_s^0$ for binnings of (a) 25 MeV (b) 50 MeV (c) 75 MeV and (d) 100 MeV

7.3 $K_s^0\Lambda^0$ channel

The $K_s^0\Lambda^0$ mass channel is reconstructed using the invariant mass formula given by Eq. 4.1. The tighter cuts taken from table 5.6 are then separately applied on the K_s^0 and the Λ^0 particles to reduce some background. Fig. 7.5 shows the full spectrum of the channel, out of which the same range of 2900-8000 MeV is investigated to look for resonant structures.

The same search method is extended to the $K_s^0\Lambda^0$ channel. The fit function described in Eq. 7.3 is used to describe the background in this channel as well, as shown in Fig. 7.6, with a reduced χ^2 of 0.98. The significance plots for binnings of 5, 25, 50, 75 and 100 MeV are shown in Figs. 7.7 and 7.8. The plots for the rest of the bin widths are included in Appendix B.2.

Once again, no significance equal to or greater than 3σ is flagged in any of the binnings, which leads to the conclusion that no resonant state is observed in the $K_s^0\Lambda^0$ channel either.

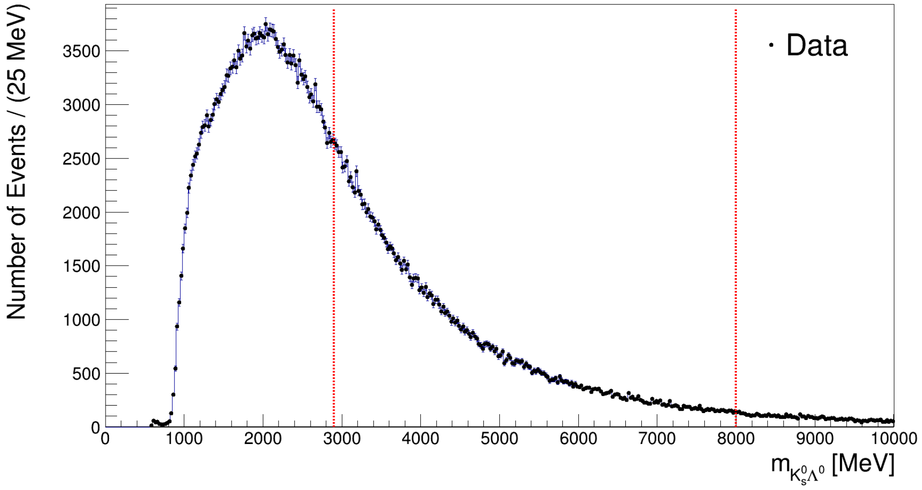

Figure 7.5: Invariant mass distribution of $K_s^0\Lambda^0$. The region bounded by the vertical red lines is investigated for search of possible multiquark states.

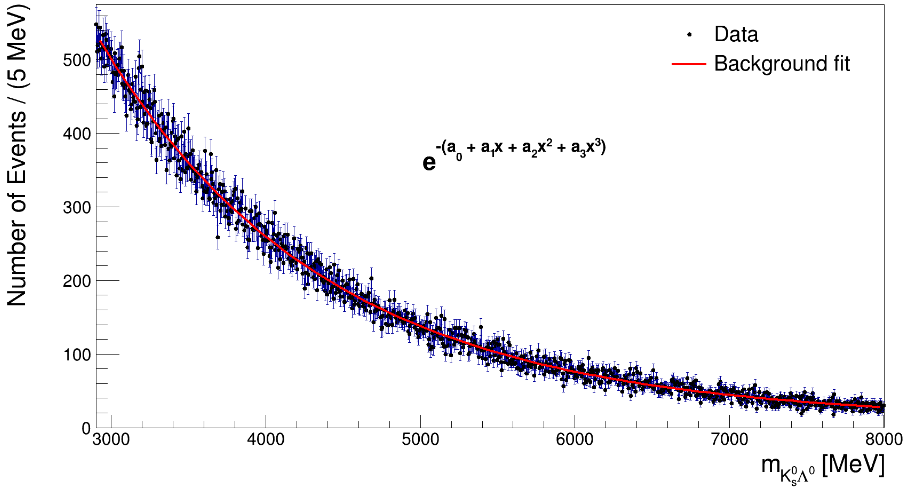

Figure 7.6: Higher range of invariant mass distribution of $K_s^0\Lambda^0$ with background fitting

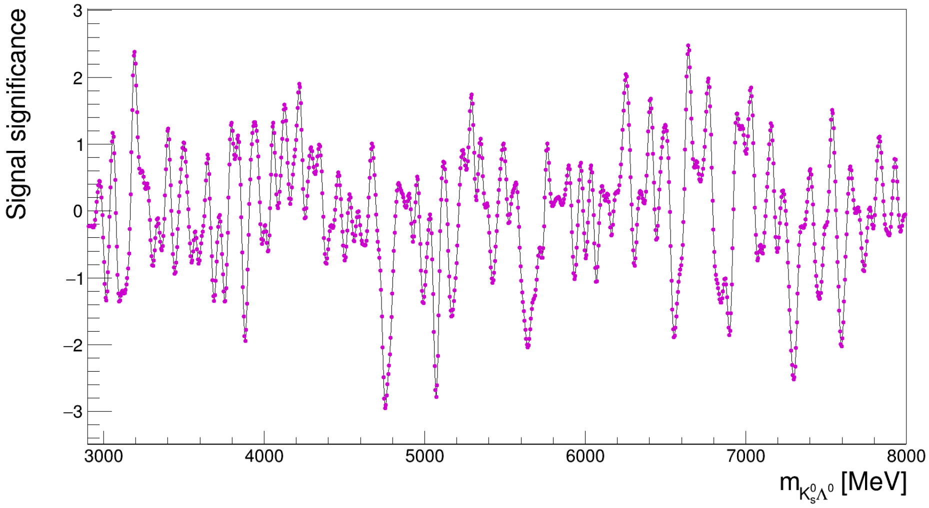

Figure 7.7: Significance plot of $K_s^0\Lambda^0$ for binning of 5 MeV

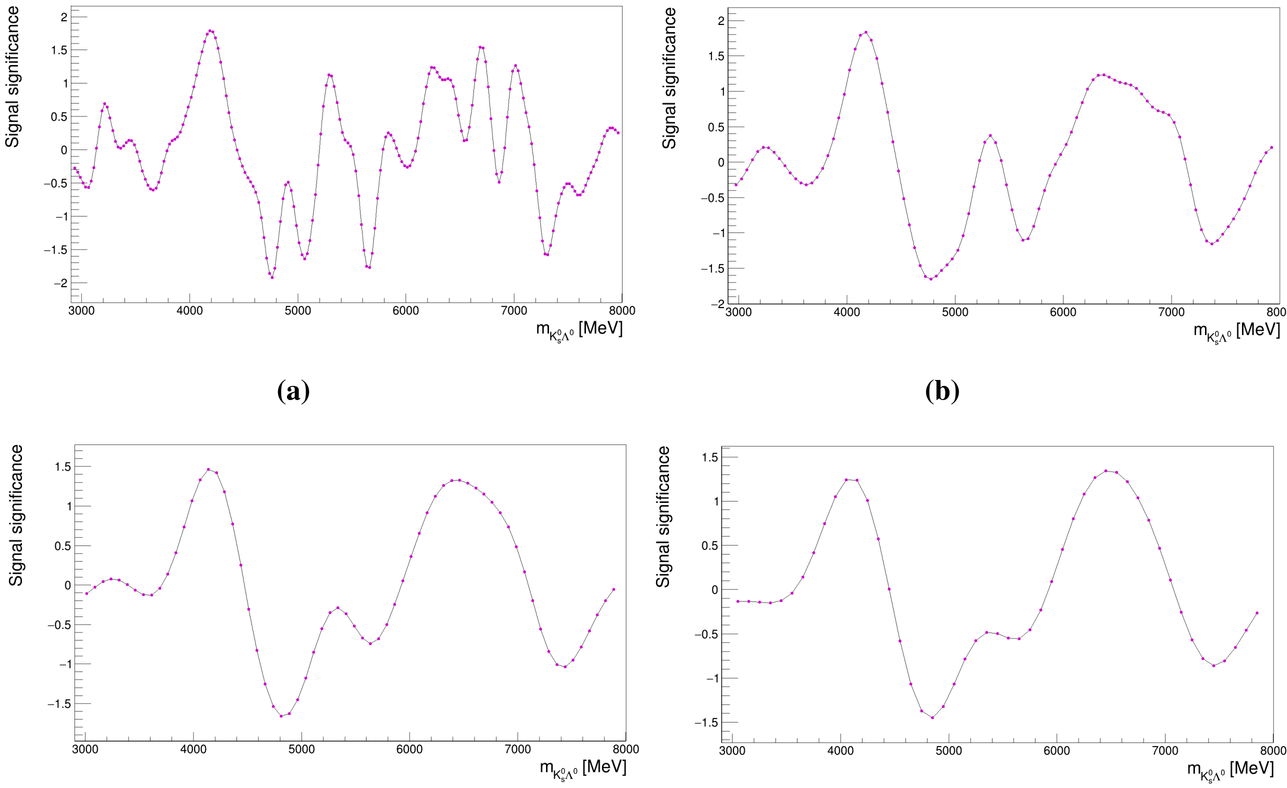

(a)

(b)

(c)

(d)

Figure 7.8: Significance plots of $K_s^0\Lambda^0$ for binnings of (a) 25 MeV (b) 50 MeV (c) 75 MeV and (d) 100 MeV.

7.4 $\Lambda^0\Lambda^0$ channel

The $\Lambda^0\Lambda^0$ invariant mass distribution is, once again, obtained in the same way as the other channels. Tighter selection cuts on each Λ^0 are applied to reduce some background. The distribution is shown in Fig. 7.9.

The bump search method described in Section 7.1 is applied on the $\Lambda^0\Lambda^0$ channel. This time the background function has a second order polynomial in the exponent, rather than a third order one, as it was more well-behaved and converged for all bin widths. It gave a reduced χ^2 of 1.02 and is shown in Fig. 7.10:

$$f(x) = \mathrm{Exp}(a_0 + a_1 x + a_2 x^2) \tag{7.3}$$

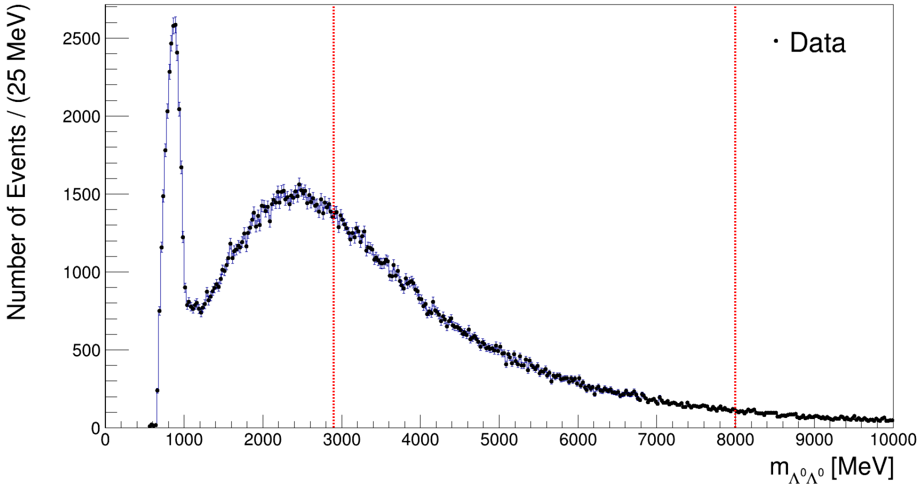

Figure 7.9: Invariant mass distribution of $\Lambda^0\Lambda^0$. The region bounded by the vertical red lines is investigated for search of possible multiquark states.

Fig. 7.11 shows few bins between 3800-4000 MeV have significance greater than 3σ with a reduced χ^2 of ~1.02 in those bins. When compared to Fig. 7.10, it can be seen that the data points in that interval lie above the background fit, which possibly results in a higher significance. This need not mean the observation of a signal, as it could be arising from purely statistical fluctuations. However, it is certainly an interesting structure, which can also be seen in Fig. 7.9, and needs

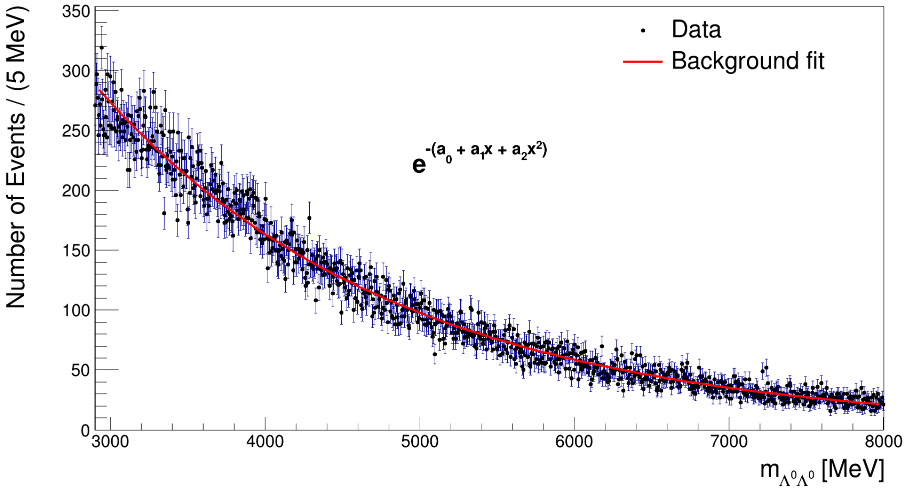

Figure 7.10: Higher range of invariant mass distribution of $\Lambda^0\Lambda^0$ with background fitting.

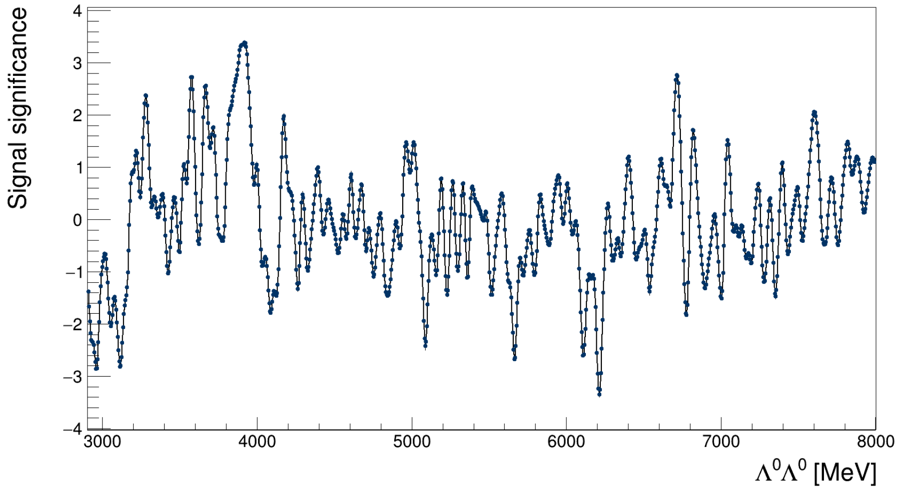

Figure 7.11: Significance plot of $\Lambda^0\Lambda^0$ for binning of 5 MeV

to be looked at more closely, including tests for the 'look elsewhere' effect to exclude any local significance [57].

Also, in Fig. 7.12, the 'peak' broadens with increasing bin width, which is to say that bins beyond 3800-4000 MeV start showing significance greater than 3σ. The fitting of the Gaussian signal is not independent in each bin since every Gaussian peak spans over three bins. This leads to a correlation of significance between consecutive bins which can consequently cause the significance

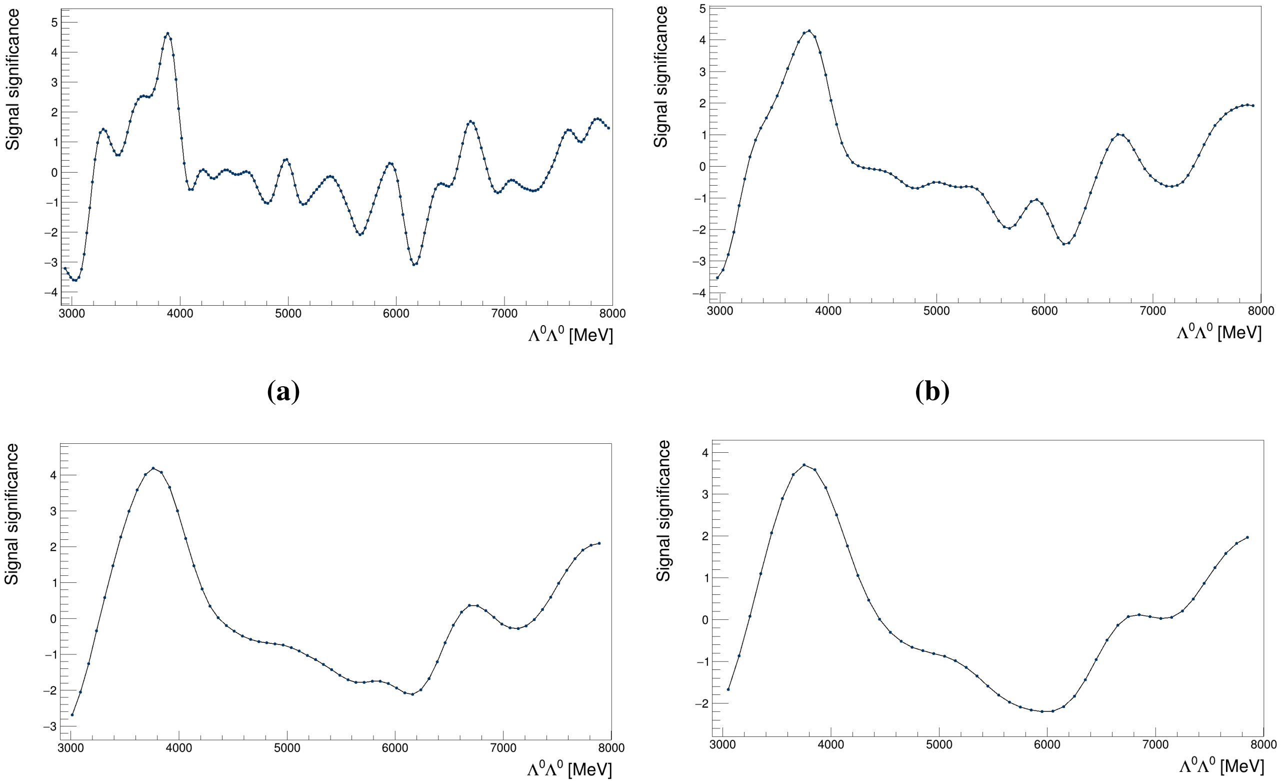

(a)

(b)

(c)

(d)

Figure 7.12: Significance plots of $\Lambda^0\Lambda^0$ for binnings of (a) 25 MeV (b) 50 MeV (c) 75 MeV and (d) 100 MeV.

of those neighbouring bins to increase as bin width increases. As with the previous channels, the significance plots in the rest of the bin widths are included in Appendix B.3.

7.5 Results

The significance plots obtained for the $K_s^0K_s^0$ and $K_s^0\Lambda^0$ channels do not point towards any possible discovery or observation of a resonant state. The significance plots for the $\Lambda^0\Lambda^0$ channel flags significance of $> 3\sigma$ for a few bins between 3800-4000 MeV. However, it could be only statistical fluctuations and/or inappropriate background modelling but calls for further study. It is difficult to draw any conclusive results using only a background estimation of the data, as the statistical fluctuations can lead to false significant signals. Previous experiments could not have conducted this study due to low statistics in this particular search range.

As a check, the normalized number of bins of given significance for bin width 5 MeV as a function of the signal significance is plotted for each of the three channels, and is compared to the standard normal distribution. Figs. 7.13 and 7.14 show that the number of bins is described well by the standard normal distribution, which implies that the significance in each bin is randomly distributed about the mean, which is zero significance in this case. A small, non-zero value between $3 - 3.5\sigma$ can be seen in Fig. 7.15, which is expected from the results discussed above. However, more comprehensive analysis is required to rule out statistical fluctuations and modelling uncertainties.

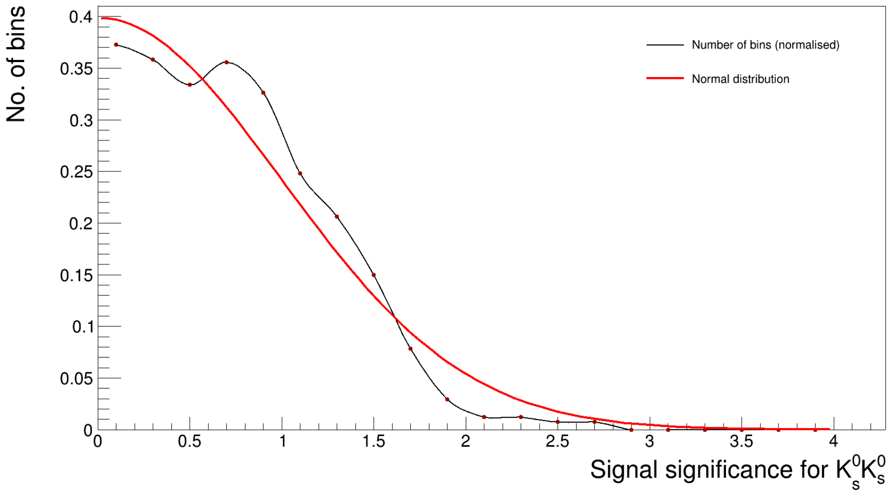

Figure 7.13: Comparison with normal distribution: $K_s^0 K_s^0$

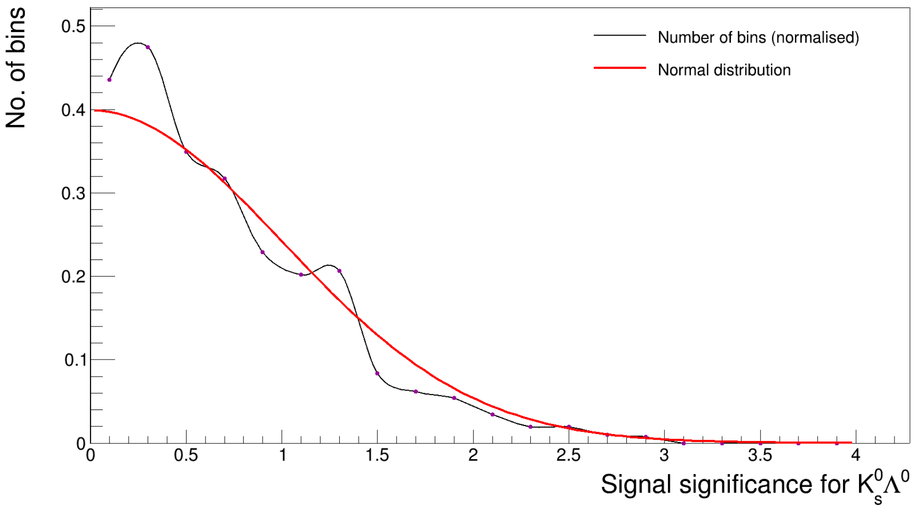

Figure 7.14: Comparison with normal distribution: $K_s^0\Lambda^0$

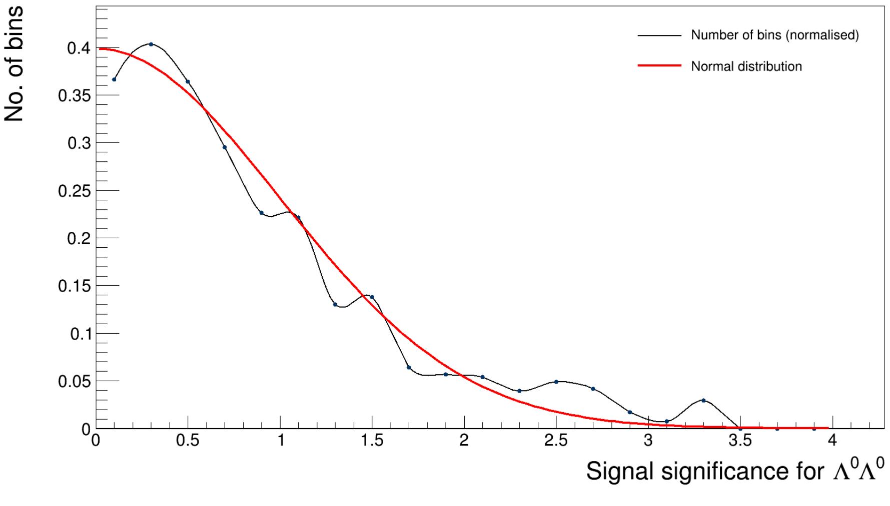

Figure 7.15: Comparison with normal distribution: $\Lambda^0\Lambda^0$

Chapter 8

Conclusion and Outlook

This analysis studies the strange particles, K_s^0 and Λ^0, to look for possible multiquark states. Minimum Bias events recorded by the ATLAS detector in 2015, in proton-proton collisions at $\sqrt{s} = 13$ TeV, corresponding to an integrated luminosity of 21.559 nb^{-1} have been used here. Initial studies are carried out on the lifetime distributions and invariant masses of the individual K_s^0 and Λ^0 to verify their identification. In the next step, the $K_s^0 K_s^0$ invariant mass spectrum is investigated where a peak at $\sim$ 1535 MeV with significance $> 5\sigma$ is observed. This is assumed to be the $f_2'(1525)$ state, though the width of the peak does not fall within the error limits set by previous experiments. The discrepancy in width and the absence of other signals, especially for the $f_J(1710)$ state, require a more thorough investigation of the background removal processes and use of the rest of the Run-2 data.

Finally, a signal searching technique is performed on the higher range of the invariant $K_s^0 K_s^0$, $K_s^0 \Lambda^0$ and $\Lambda^0 \Lambda^0$ mass spectra to look for possible tetraquark, pentaquark and hexaquark states. No observation of signal with $> 5\sigma$ significance has been made using different bin widths. The $\Lambda^0 \Lambda^0$ mass spectrum does show significance of $> 3\sigma$ in the range of 3800-4000 MeV, but it could be possible due to the modelling of the background and reduced statistics. Since no MC simulations have been used in this analysis, the background modelling is only approximate.

This is a feasibility study to search for multiquark states using strange particles and there exists a lot of scope to improve the results. Firstly, only 2015 data has been used in this analysis, which is a small fraction of the entire run-2 (2015-2018) data. Analysis of the 2016-2018 data has not been possible due to the time constraints of the thesis, but more events can provide better estimates of the statistical effects in the results. Moreover, MC simulations are not considered because of the same time constraints and computational challenges, and also because the simulations do not contain any information on possible multiquark states. As such systematic uncertainties from the detector could not be considered. Systematics from other sources, like selection cuts and fits, also need to be considered to give a better approximation on the invariant mass and lifetime values of the K_s^0 and Λ^0. At the time of writing this thesis, studies are currently ongoing for better understanding of the background and lifetime distributions of the K_s^0 and Λ^0.

The limits on the cross-section of the $K_s^0K_s^0$, $K_s^0\Lambda^0$ and $\Lambda^0\Lambda^0$ invariant masses could not be derived since no acceptance limits were available due to the absence of MC simulations. An approximate limit can be still measured from the number of events and the luminosity of 21.559 nb^{-1}, considering acceptance limit as 100%. This gives 76.9 nb at a significance of 2.8σ for $K_s^0K_s^0$, 27.2 nb at 2.9σ for $K_s^0\Lambda^0$ and 34.9 nb at 3.3σ for $\Lambda^0\Lambda^0$. Thus, it can be concluded that using the entire Run-2 data and MC simulations, and the signal searching technique described here, a comprehensive study and more quantitative study would be worth doing on the search for possible multiquark states decaying to strange particles.

Appendices

Appendix A

Gaussian fits to invariant mass distributions

As mentioned in Section 5.2, a function comprising of a double-Gaussian and a linear polynomial provides a better fit to the invariant mass distributions of the K_s^0 and Λ^0. The function is described as:

$$f(x) = h_0 \exp\left(-\frac{(x-\mu)^2}{2\sigma_0^2}\right) + h_1 \exp\left(-\frac{(x-\mu)^2}{2\sigma_1^2}\right) + c_0 + c_1 x, \tag{A.1}$$

where the heights (h_0, h_1) and SD (σ_0, σ_1) of the Gaussian functions describing the signal vary but the mean μ for both the Gaussians is the same. The linear polynomial, $c_0 + c_1 x$, describes the background. Table A.1 compares the results of this fit with the single-Gaussian fit.

Particle	Single-Gaussian fit		Double-Gaussian fit	
	Mass [MeV]	Width [MeV]	Mass [MeV]	Width [MeV]
K_s^0	497.803 ± 0.002	5.852 ± 0.006	497.808 ± 0.003	16.339 ± 0.039
Λ^0	1115.820 ± 0.002	2.627 ± 0.002	1115.800 ± 0.003	4.329 ± 0.018

Table A.1: Comparison of mass and width of peaks with the single-Gaussian and double-Gaussian fit

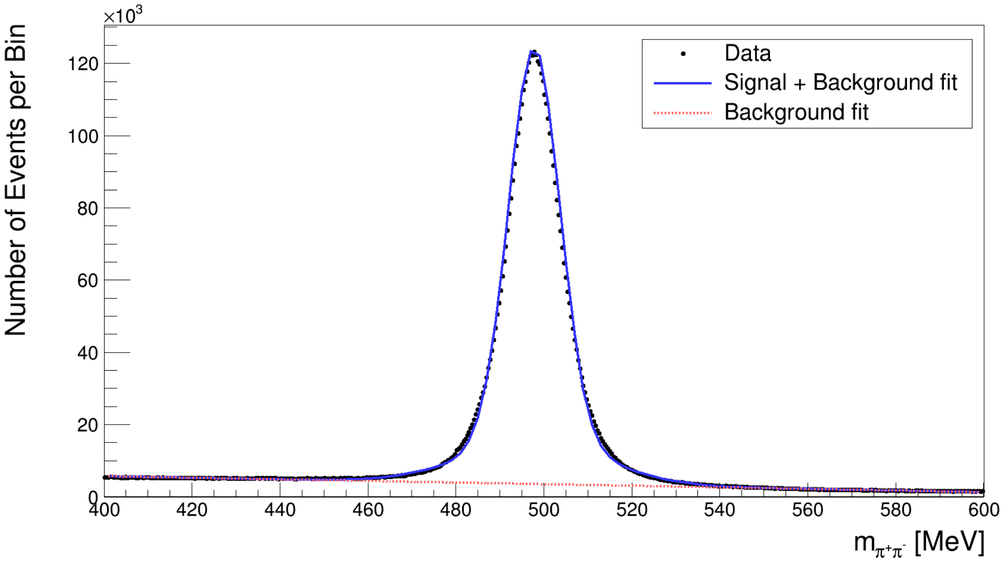

(a)

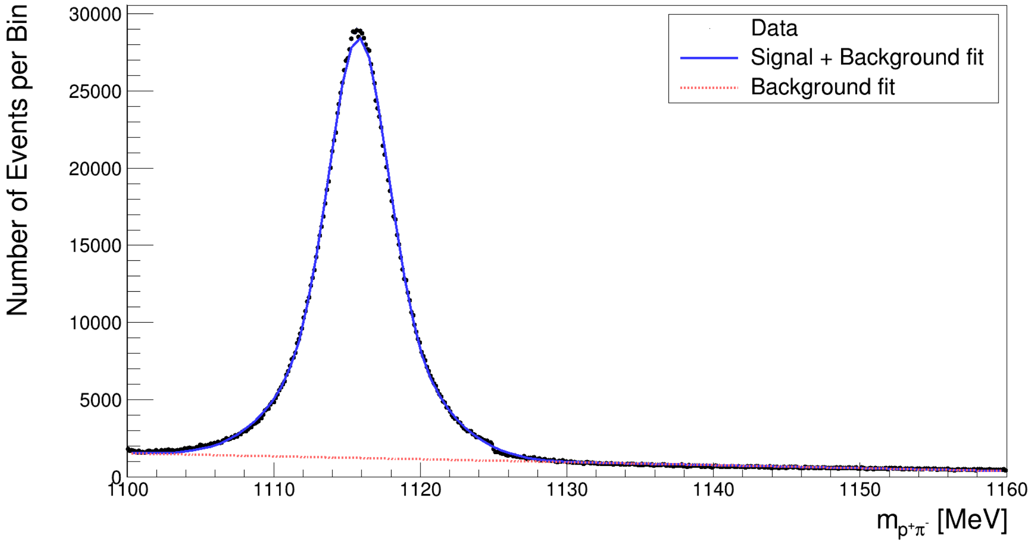

(b)

Figure A.1: Invariant mass distribution of (a) K_s^0 and (b) Λ^0 with a double gaussian fitting to describe the signal. The peak for K_s^0 is at 497.8 MeV and that for Λ^0 is at 1115.8 MeV.

Appendix B

Additional plots for different binnings in multiquark search

This section presents the significance plots in different bin widths for the three channels.

B.1 $K_s^0 K_s^0$ channel

Fig. B.1 shows the significance plots for $K_s^0 K_s^0$ in different bin widths, ranging from 5 MeV to 100 MeV, with increase in step of 5 MeV.

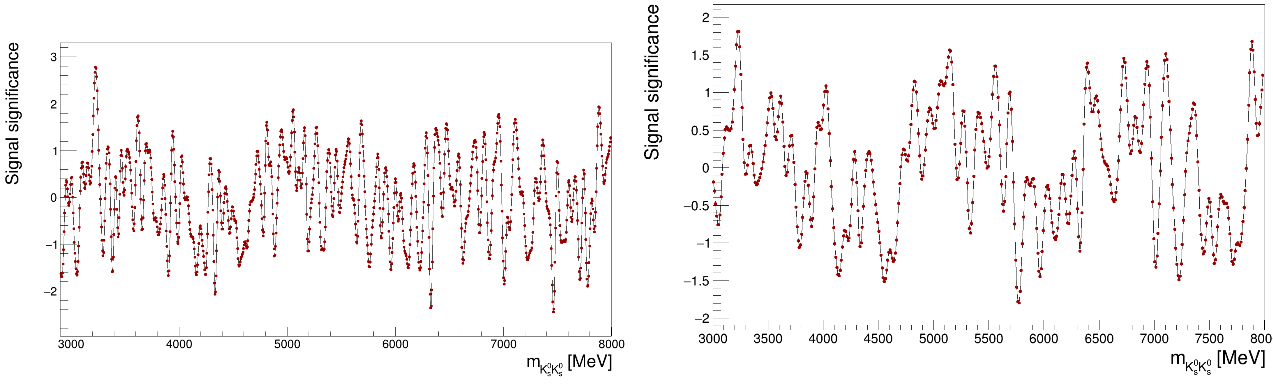

(a) 5 MeV

(b) 10 MeV

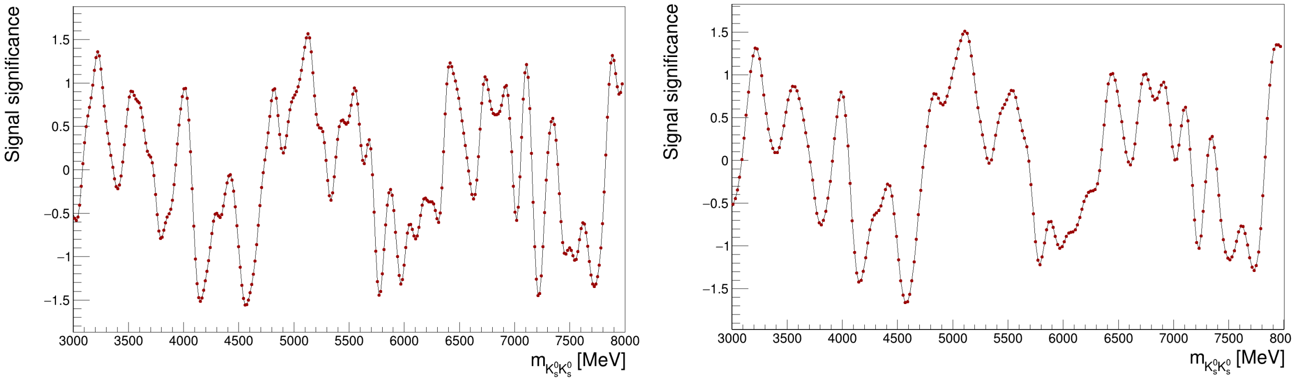

(c) 15 MeV

(d) 20 MeV

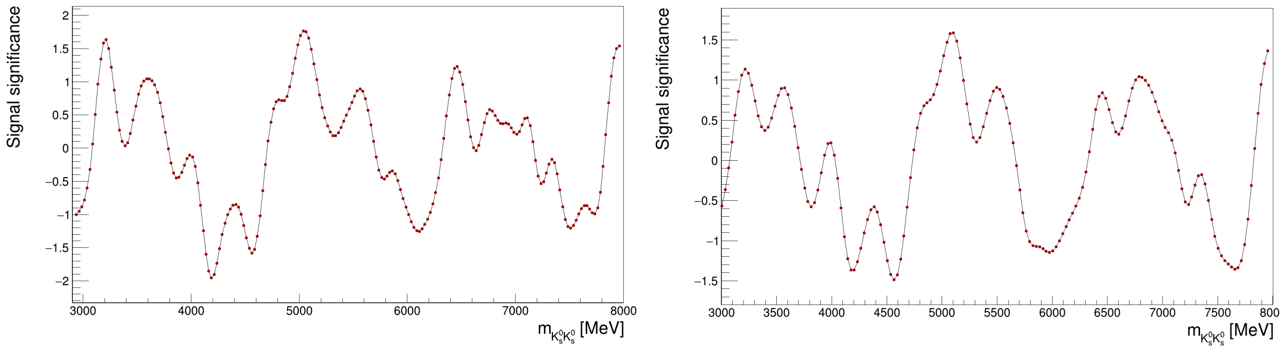

(e) 25 MeV

(f) 30 MeV

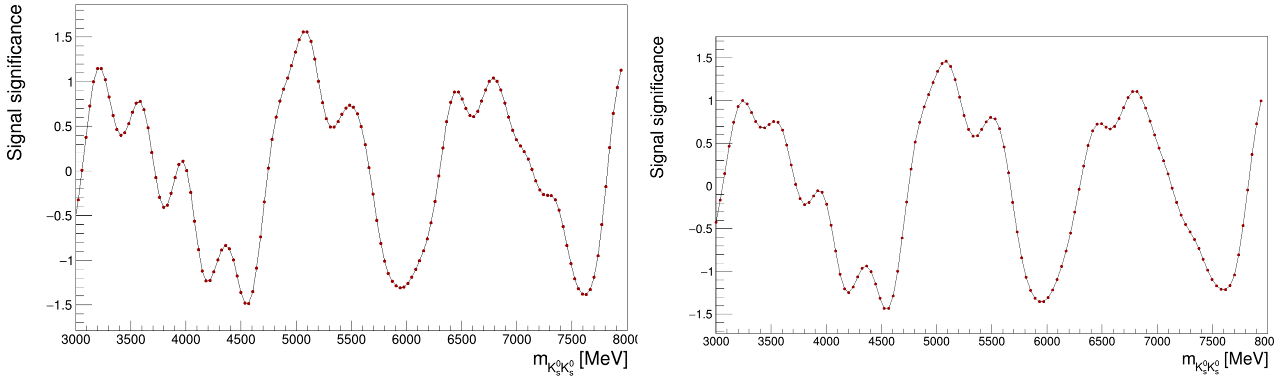

(g) 35 MeV

(h) 40 MeV

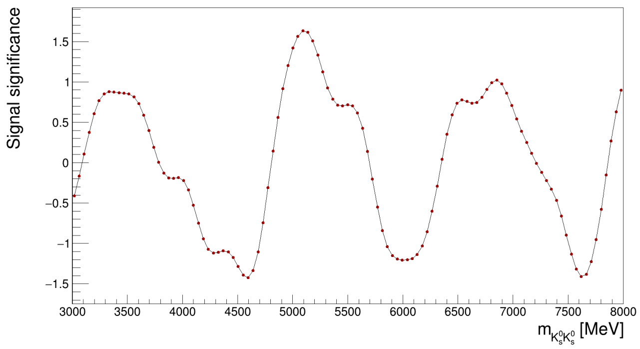

(i) 45 MeV

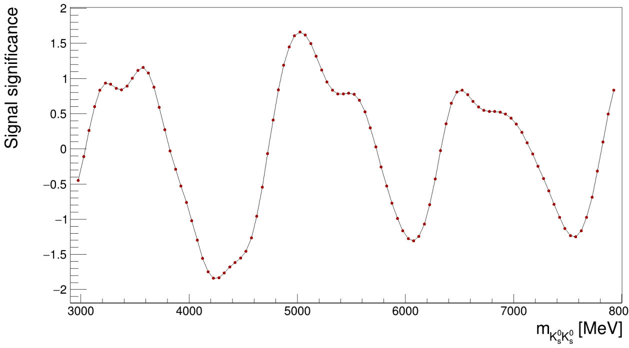

(j) 50 MeV

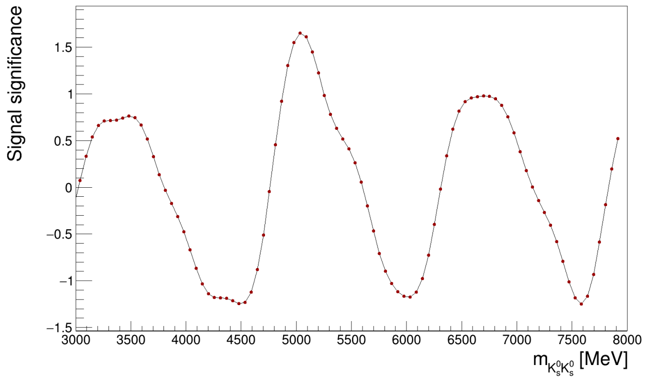

(k) 55 MeV

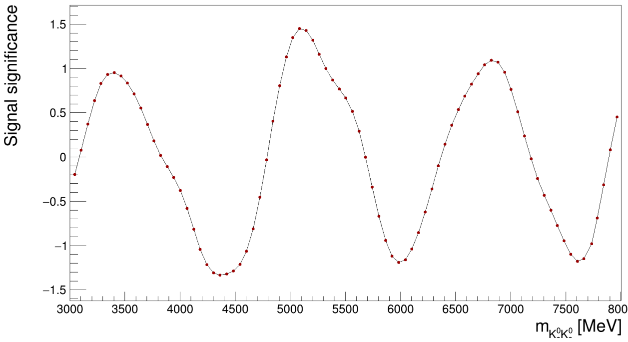

(l) 60 MeV

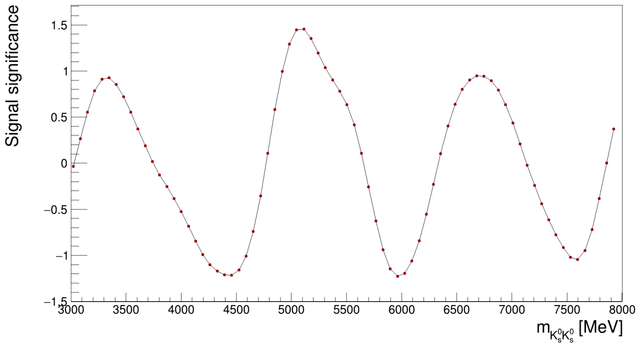

(m) 65 MeV

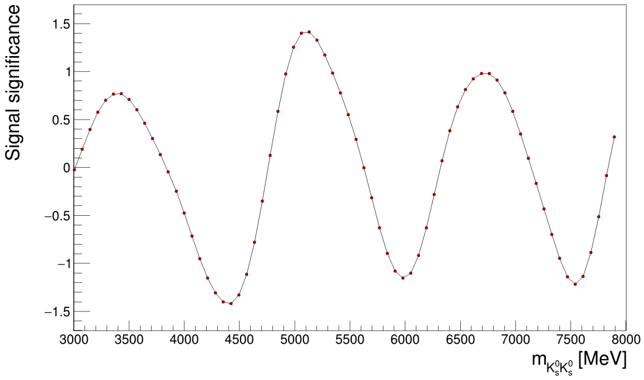

(n) 70 MeV

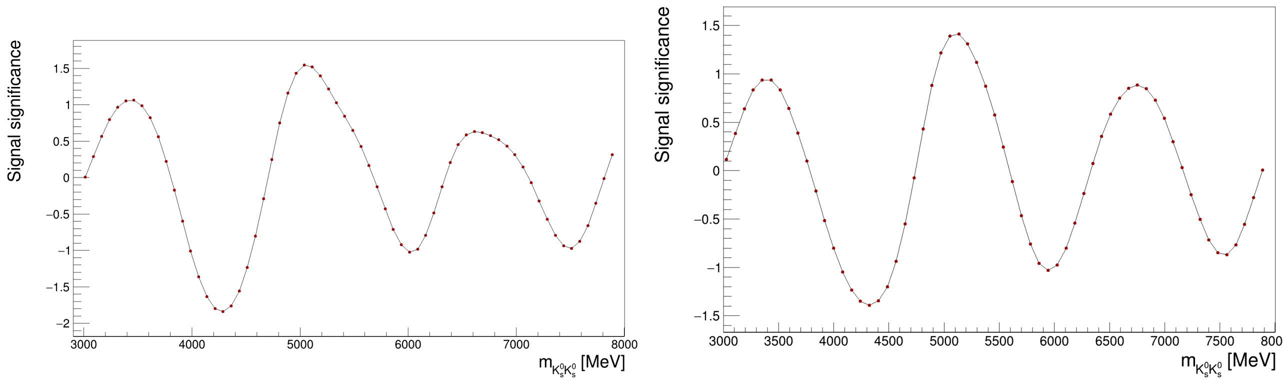

(o) 75 MeV

(p) 80 MeV

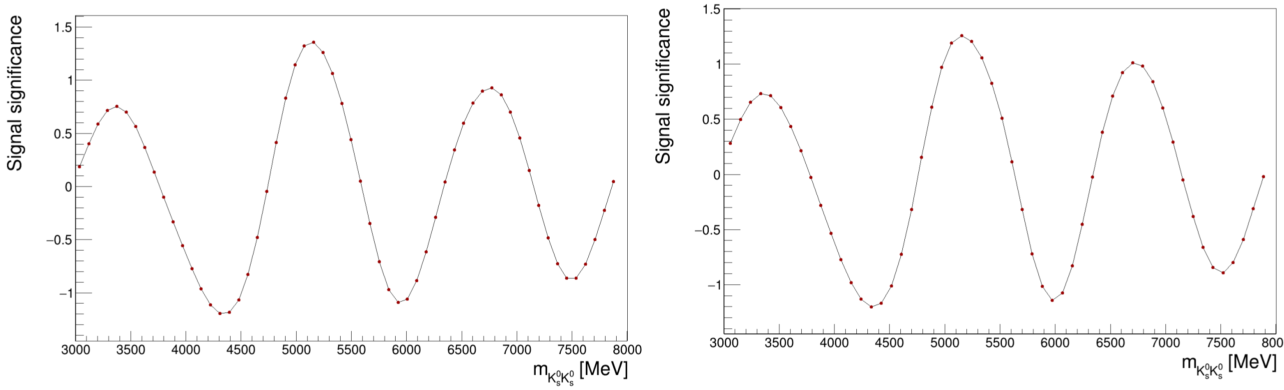

(q) 85 MeV

(r) 90 MeV

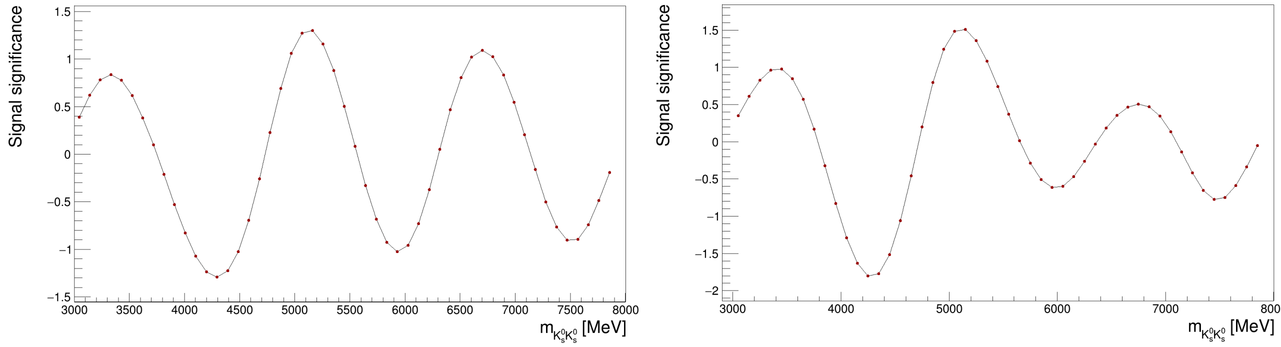

(s) 95 MeV

(t) 100 MeV

Figure B.1: Significance plots in different bin widths for $K_s^0 K_s^0$.

B.2 $K_s^0\Lambda^0$ channel

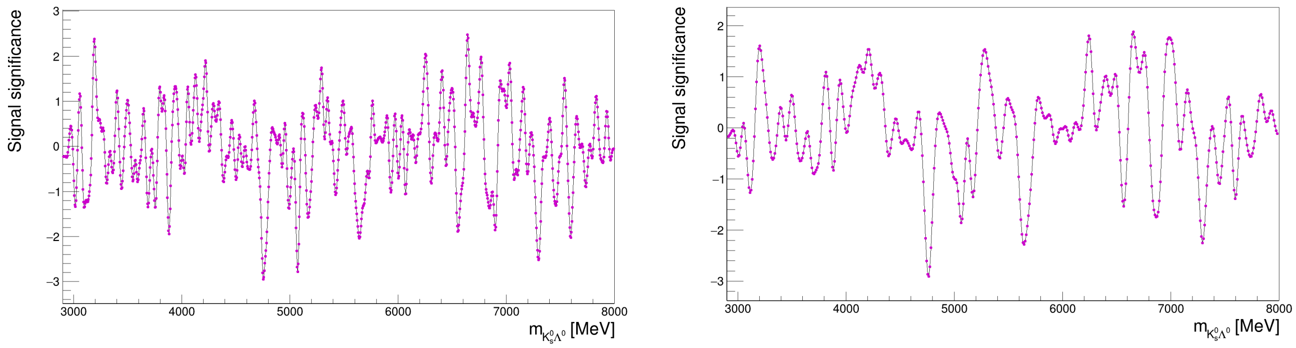

(a) 5 MeV

(b) 10 MeV

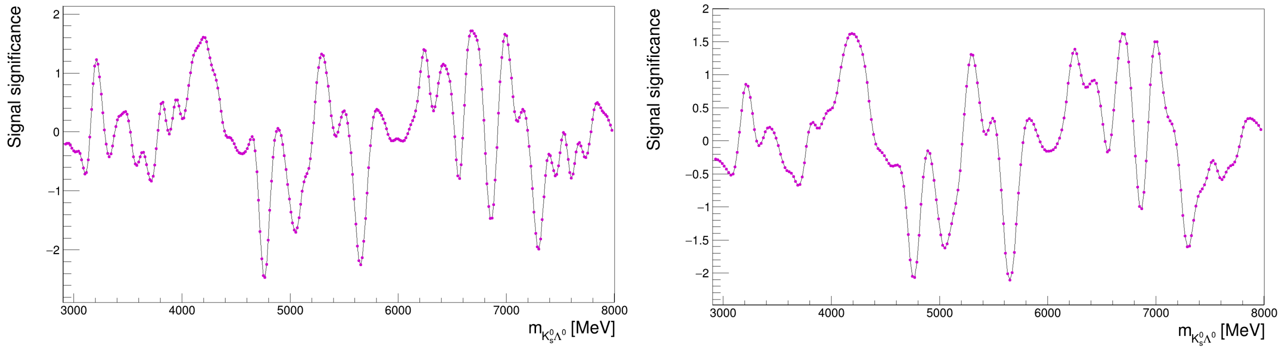

(c) 15 MeV

(d) 20 MeV

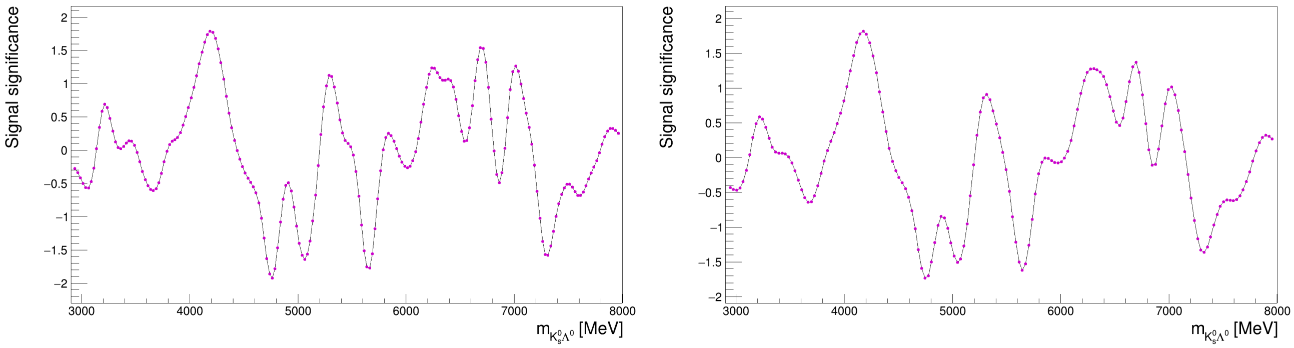

(e) 25 MeV

(f) 30 MeV

Similar to the previous section, Fig. B.2 shows the significance plots for $K_s^0\Lambda^0$ in different bin widths, ranging from 5 MeV to 100 MeV, with increase in step of 5 MeV.

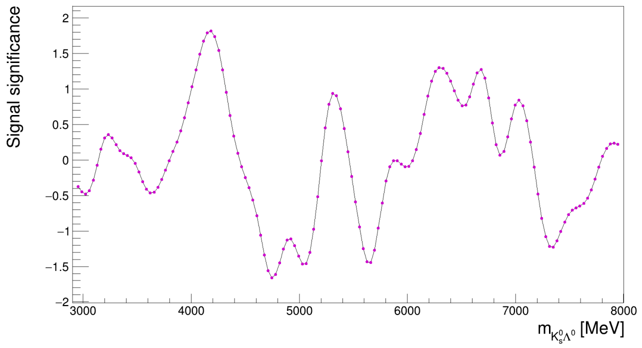

(g) 35 MeV

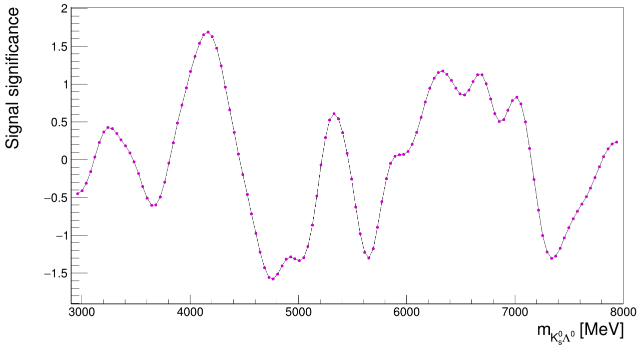

(h) 40 MeV

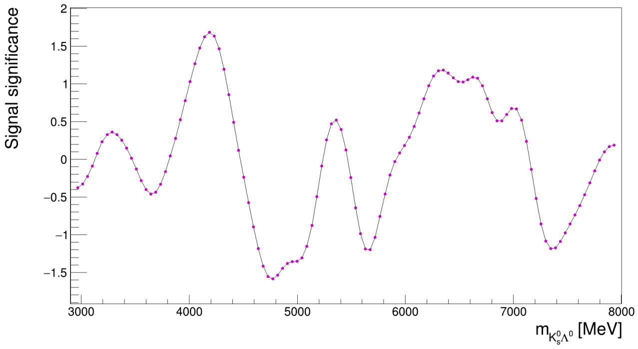

(i) 45 MeV

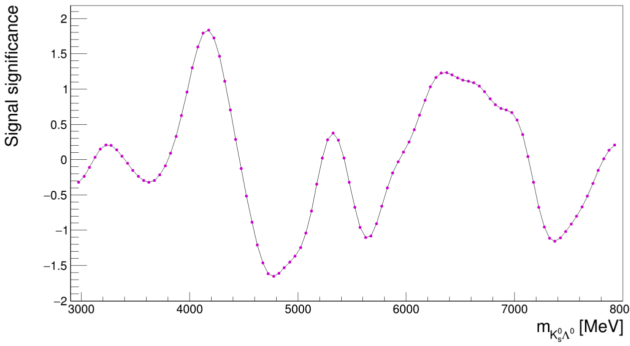

(j) 50 MeV

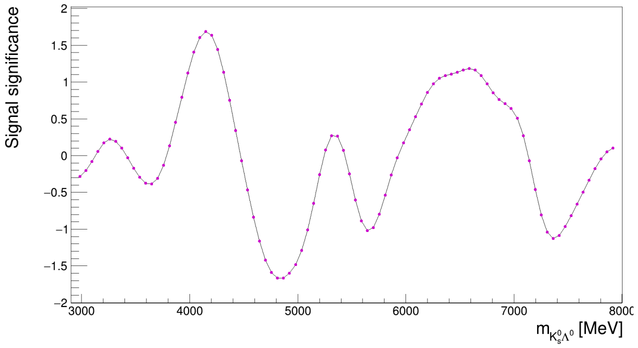

(k) 55 MeV

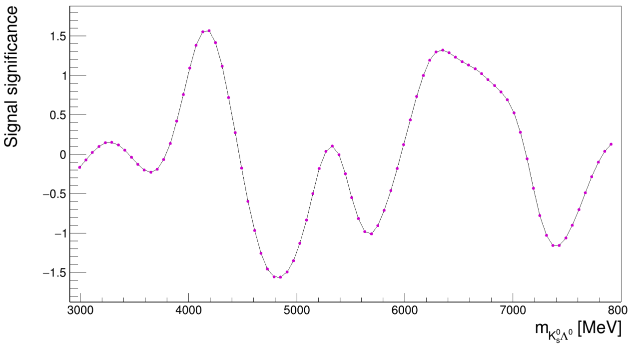

(l) 60 MeV

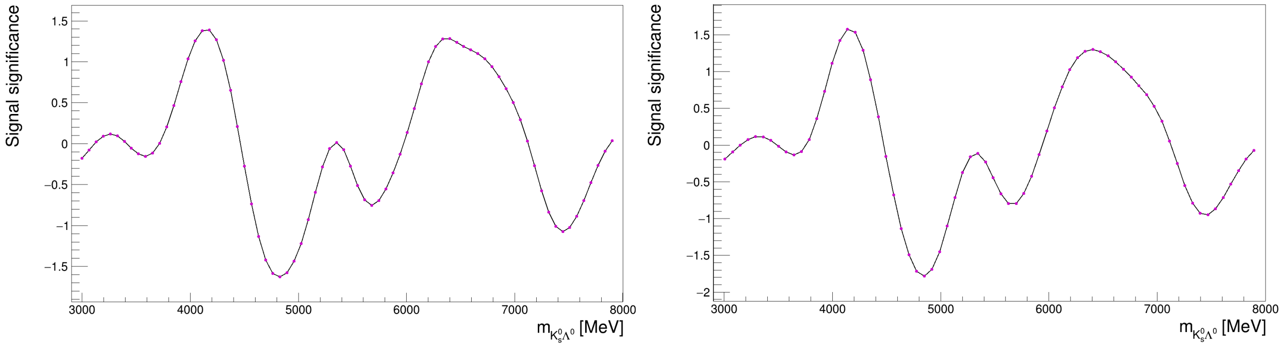

(m) 65 MeV

(n) 70 MeV

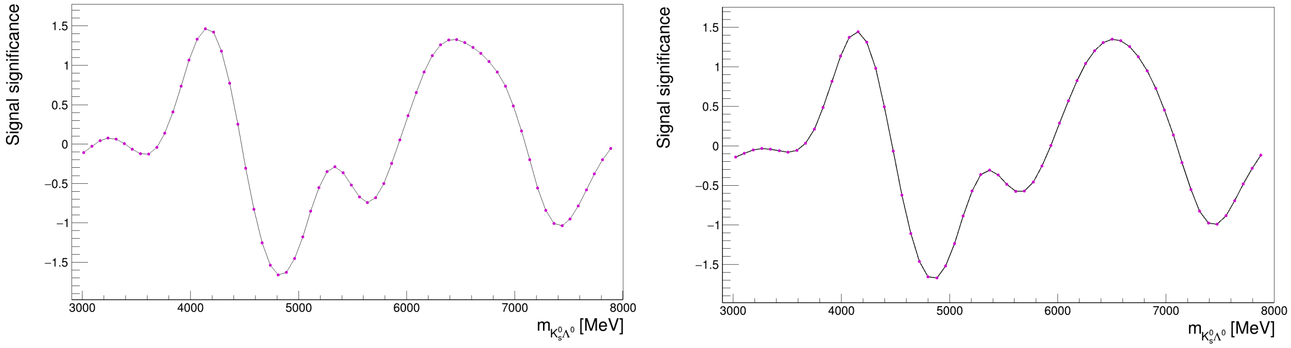

(o) 75 MeV

(p) 80 MeV

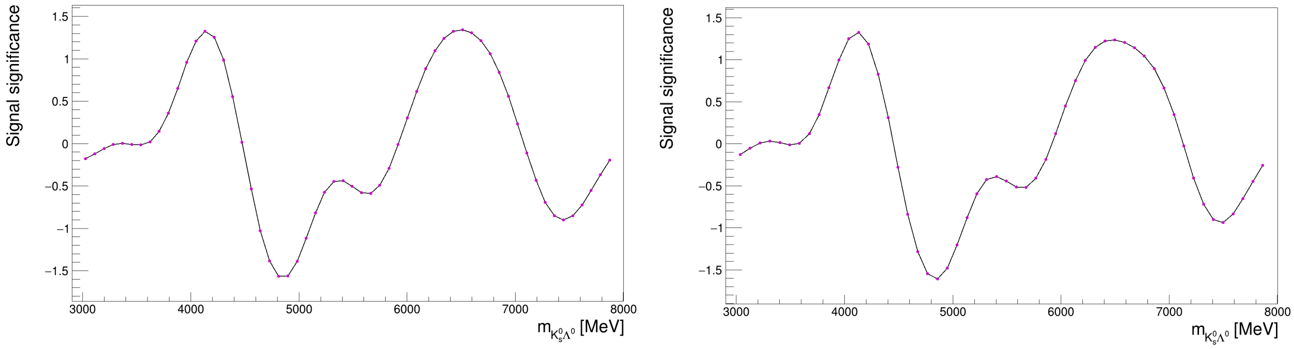

(q) 85 MeV

(r) 90 MeV

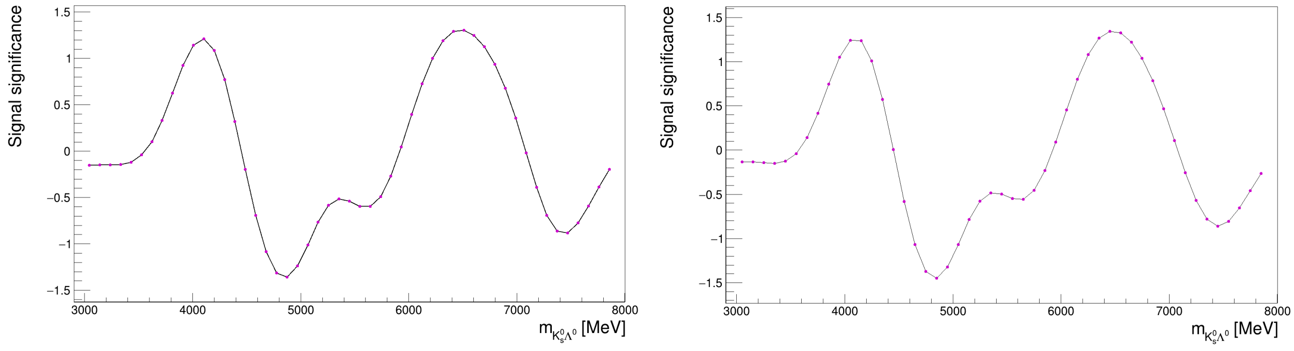

(s) 95 MeV

(t) 100 MeV

Figure B.2: Significance plots in different bin widths for $K_s^0\Lambda^0$.

B.3 $\Lambda^0\Lambda^0$ channel

As in the previous two sections, Fig. B.3 shows the significance plots for $K_s^0\Lambda^0$ in different bin widths, ranging from 5 MeV to 100 MeV, with increase in step of 5 MeV.

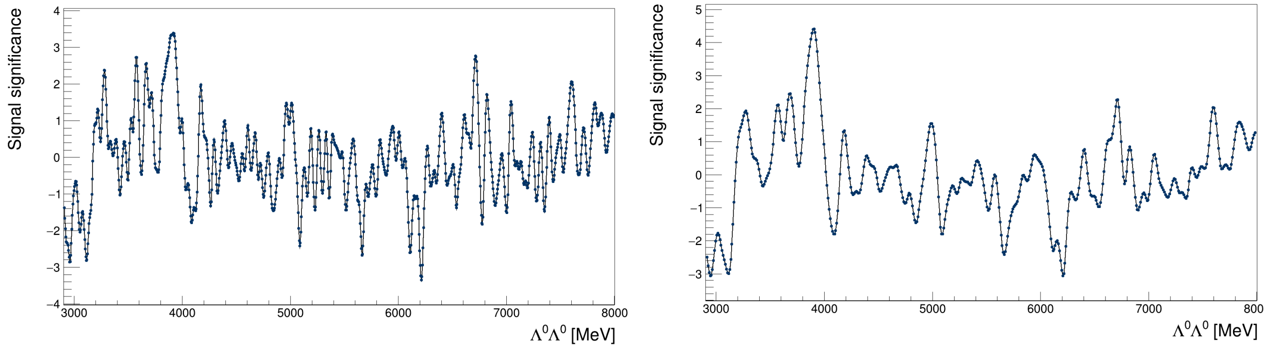

(a) 5 MeV

(b) 10 MeV

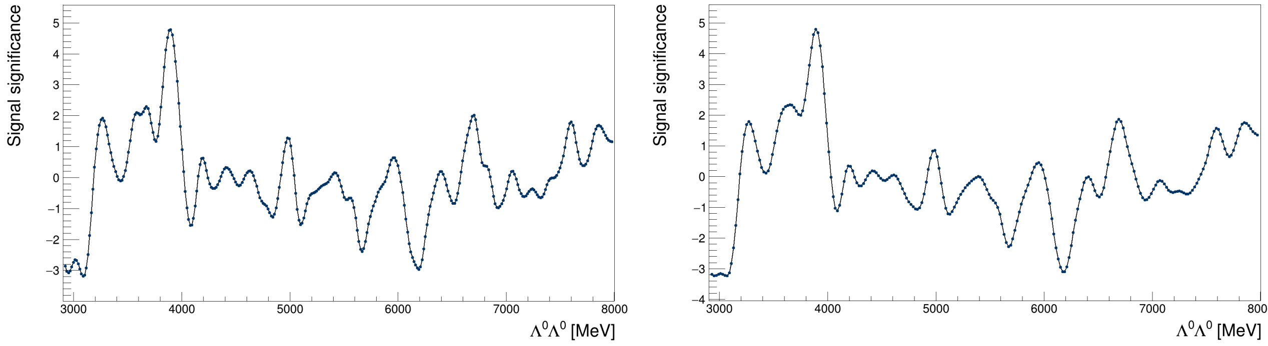

(c) 15 MeV **(d)** 20 MeV

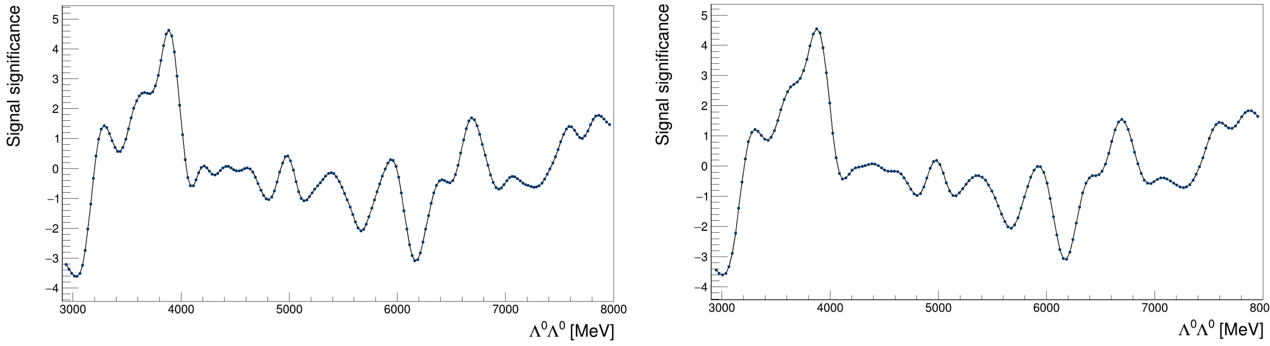

(e) 25 MeV **(f)** 30 MeV

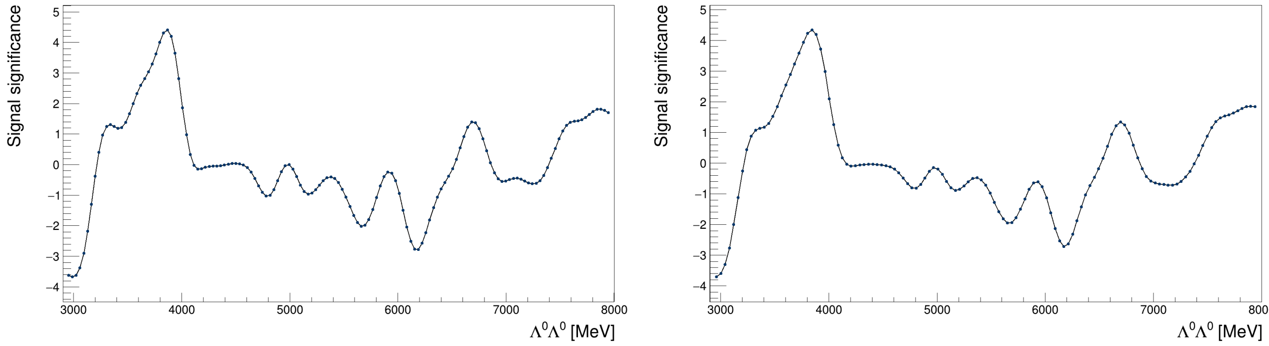

(g) 35 MeV **(h)** 40 MeV

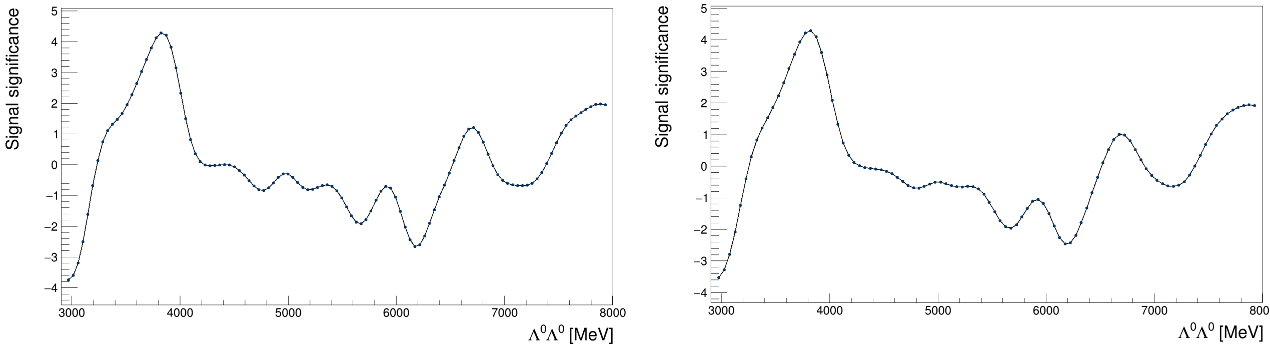

(i) 45 MeV **(j)** 50 MeV

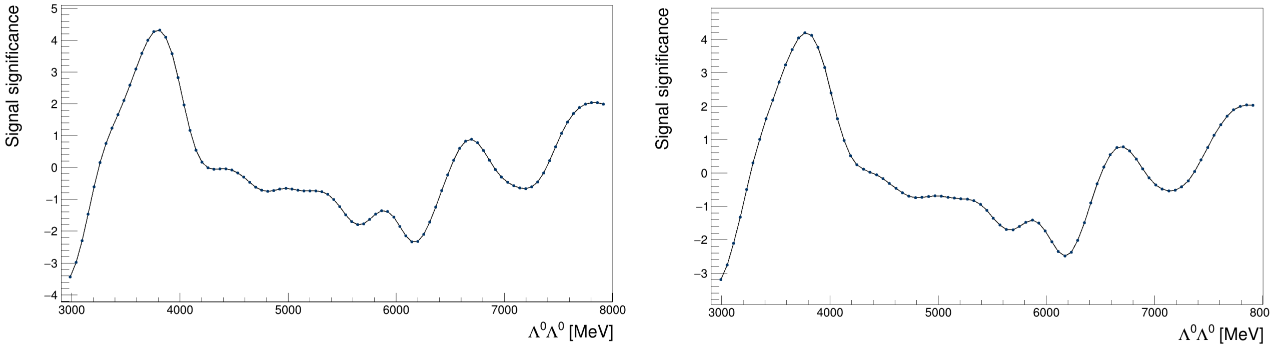

(k) 55 MeV

(l) 60 MeV

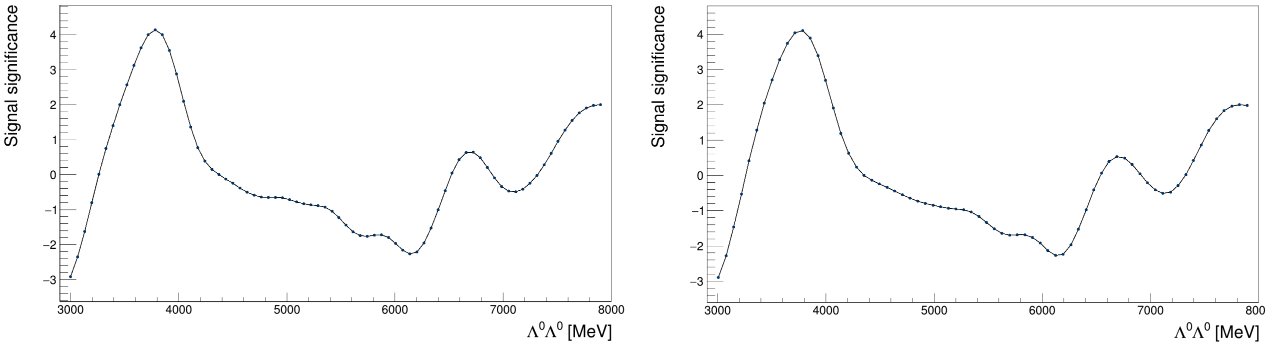

(m) 65 MeV

(n) 70 MeV

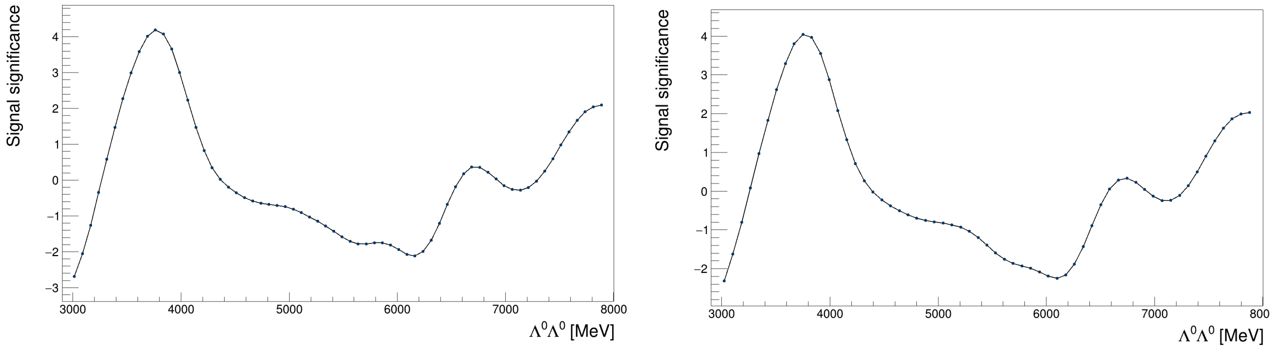

(o) 75 MeV

(p) 80 MeV

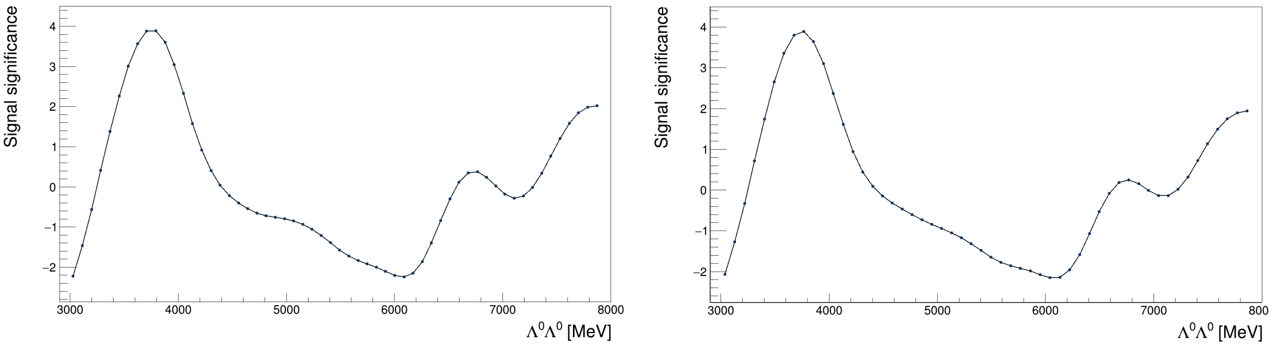

(q) 85 MeV

(r) 90 MeV

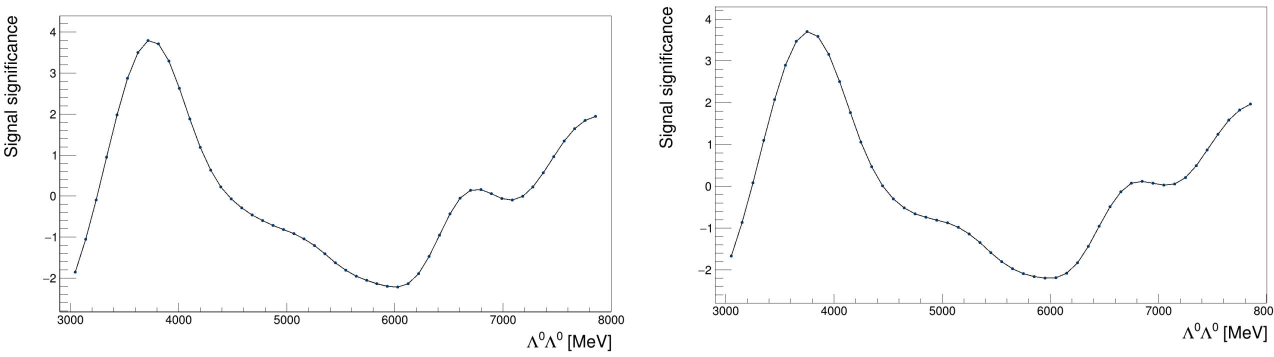

(s) 95 MeV

(t) 100 MeV

Figure B.3: Significance plots in different bin widths for $\Lambda^0\Lambda^0$.

Acronyms

ATLAS A Toroidal LHC ApparatuS.

BSM Beyond Standard Model.

CERN Conseil Européen pour la Recherche Nucléaire.

CSC Cathode Strip Chambers.

CTP Central Trigger Processor.

ECAL electromgnetic calorimeter.

HCAL hadron calorimeter.

HLT High Level Trigger.

ID Inner Detector.

L1 Level-1.

LAr liquid Argon.

LHC Large Hadron Collider.

LS2 Long Shutdown 2.

MBTS Minimum Bias Trigger Scintillators.

MC Monte Carlo.

MDT Monitored Drift Tube.

MS Muon Spectrometer.

PD Pixel Detector.

PDG Particle Data Group.

QCD quantum chromodynamics.

QED quantum electrodynamics.

RF radiofrequency.

RMS Root Mean Square.

RoI Regions of Interest.

RPC Resistive Plate Chamber.

SCT Semiconductor Detector.

SM Standard Model.

SNR Signal to Noise Ratio.

SPS Super Proton Synchrotron.

TDAQ trigger and data acquisition system.

TGC Thin Gap Chamber.

TRT Transition-Radiation Tracker.

TTC Timing, Trigger and Control system.

Bibliography

[1] S.-K. Choi et al. "Observation of a Narrow Charmonium like State in Exclusive $B^{\pm} \rightarrow K^{\pm}\pi^{+}\pi^{-}J/\psi$ Decays". In: *Physical Review Letters* 91.26 (Dec. 2003). DOI: 10.1103/physrevlett.91.262001.

[2] G. Mezzadri and S. Spataro. "XYZ states: An experimental point-of-view". In: *Reviews in Physics* 8 (2022), p. 100070. ISSN: 2405-4283. DOI: https://doi.org/10.1016/j.revip.2022.100070.

[3] M. Acciarri et al. "K0SK0S final state in two-photon collisions and implications for glueballs". In: *Physics Letters B* 501.3-4 (Mar. 2001), pp. 173–182. DOI: 10.1016/s0370-2693(01)00116-2.

[4] C. Zhou. "Inclusive KS0KS0 Resonance Production in Electron-Proton Collisions at HERA". PhD thesis. McGill University, 2010.

[5] ATLAS Collaboration. "The ATLAS Experiment at the CERN Large Hadron Collider". In: *JINST* 3 (2008), S08003. 437 p. URL: https://cds.cern.ch/record/1129811.

[6] W. N. Cottingham and D. A. Greenwood. *An Introduction to the Standard Model of Particle Physics*. Cambridge University Press, 2007. ISBN: 9780511791406.

[7] Mark Thomson. *Modern Particle Physics*. Cambridge University Press, 2013. ISBN: 9781107034266.

[8] MissMJ and Cush. "Standard Model of Elementary Particles". Sept. 2019. URL: https://creativecommons.org/licenses/by/3.0/deed.en.

[9] CMS Collaboration. "The CMS experiment at the CERN LHC. The Compact Muon Solenoid experiment". In: *JINST* 3 (2008), S08004. 361 p. URL: https://cds.cern.ch/record/1129810.

[10] Ian C. Brock and Thomas Schörner-Sadenius. "Setting the Scene". In: *Physics at the Terascale*. John Wiley and Sons, Ltd, 2011. Chap. 1, pp. 1–22. ISBN: 9783527634965.

[11] R. L. Workman et al. "Review of Particle Physics". In: *PTEP* 2022 (2022), p. 083C01. DOI: 10.1093/ptep/ptac097.

[12] S. L. Olsen, T. Skwarnicki, and D. Zieminska. "Nonstandard heavy mesons and baryons: Experimental evidence". In: *Reviews of Modern Physics* 90.1 (Feb. 2018). DOI: 10.1103/revmodphys.90.015003.

[13] M. Gell-Mann. "A schematic model of baryons and mesons". In: *Physics Letters* 8.3 (1964), pp. 214–215. ISSN: 0031-9163. DOI: https://doi.org/10.1016/S0031-9163(64)92001-3.

[14] H. Fritzsch, M. Gell-Mann, and H. Leutwyler. "Advantages of the color octet gluon picture". In: *Physics Letters B* 47.4 (1973), pp. 365–368. ISSN: 0370-2693. DOI: https://doi.org/10.1016/0370-2693(73)90625-4.

[15] J. Vijande, A. Valcarce, and J. M. Richard. "Stability of hexaquarks in the string limit of confinement". In: *Phys. Rev. D* 85 (2012), p. 014019. DOI: 10.1103/PhysRevD.85.014019. arXiv: `1111.5921 [hep-ph]`.

[16] V. Mathieu, N. Kochelev, and V. Vento. "The Physics of glueballs". In: 18.01 (Jan. 2009), pp. 1–49. DOI: 10.1142/s0218301309012124.

[17] Nathan Isgur and Jack Paton. "Flux-tube model for hadrons in QCD". In: *Phys. Rev. D* 31 (11 June 1985), pp. 2910–2929. DOI: 10.1103/PhysRevD.31.2910.

[18] P. Koppenburg. "List of hadrons observed at the LHC". In: LHCb-FIGURE-2021-001 (Mar. 2021). and 2022 updates. URL: https://cds.cern.ch/record/2693187.

[19] LHCb Website. *Observation of a strange pentaquark, a doubly charged tetraquark and its neutral partner.* https://lhcb-outreach.web.cern.ch/2022/07/05/observation-of-a-strange-pentaquark-a-doubly-charged-tetraquark-and-its-neutral-partner/. (Accessed: 23.07.2022).

[20] M. S. Livingston and J Blewett. *Particle Accelerators*. New York: McGraw-Hill, 1969. ISBN: 9781114443846.

[21] CERN Website. *The History of CERN.* https://timeline.web.cern.ch/timeline-header/89. (Accessed: 23.04.2022).

[22] CERN Website. *CERN's accelerator complex*. https://home.cern/science/accelerators/accelerator-complex. (Accessed: 23.04.2022).

[23] Ewa Lopienska. "The CERN accelerator complex". In: (3Feb 2022). https://cds.cern.ch/images/CERN-GRAPHICS-2022-001-1.

[24] CERN Website. *The Large Hadron Collider*. https://home.cern/science/accelerators/large-hadron-collider. (Accessed: 23.04.2022).

[25] CERN Website. *A vacuum as empty as interstellar space*. https://home.cern/science/engineering/vacuum-empty-interstellar-space. (Accessed: 23.04.2022).

[26] CERN Website. *Pulling together: Superconductinng electromagnets*. https://home.cern/science/engineering/pulling-together-superconducting-electromagnets. (Accessed: 23.04.2022).

[27] LHCb Collaboration. "The LHCb Detector at the LHC". In: *JINST* 3 (2008), S08005. DOI: 10.1088/1748-0221/3/08/S08005. URL: https://cds.cern.ch/record/1129809.

[28] ALICE Collaboration. "The ALICE experiment at the CERN LHC. A Large Ion Collider Experiment". In: *JINST* 3 (2008), S08002. 259 p. URL: https://cds.cern.ch/record/1129812.

[29] Joao Pequenao. "Computer generated image of the whole ATLAS detector". Mar. 2008. URL: https://cds.cern.ch/record/1095924.

[30] Ana Maria Rodriguez Vera and Joao Antunes Pequenao. "ATLAS Detector Magnet System". General Photo. May 2021. URL: https://cds.cern.ch/record/2770604.

[31] Joao Pequenao. "Computer generated image of the ATLAS inner detector". Mar. 2008. URL: https://cds.cern.ch/record/1095926.

[32] ATLAS Collaboration. "ATLAS inner detector: Technical Design Report, 1". In: Technical design report. ATLAS (1997). URL: http://cds.cern.ch/record/331063.

[33] M Capeans et al. "ATLAS Insertable B-Layer Technical Design Report". In: (Sept. 2010). URL: https://cds.cern.ch/record/1291633.

[34] Joao Pequenao. "Computer Generated image of the ATLAS calorimeter". Mar. 2008. URL: https://cds.cern.ch/record/1095927.

[35] ATLAS Collaboration. “ATLAS liquid-argon calorimeter: Technical Design Report”. In: Technical design report. ATLAS (1996). URL: http://cds.cern.ch/record/331061.

[36] ATLAS Collaboration. “ATLAS tile calorimeter: Technical Design Report”. In: Technical design report. ATLAS (1996). URL: http://cds.cern.ch/record/331062.

[37] Joao Pequenao. “Computer generated image of the ATLAS Muons subsystem”. Mar. 2008. URL: https://cds.cern.ch/record/1095929.

[38] ATLAS Collaboration. “ATLAS muon spectrometer: Technical Design Report”. In: Technical design report. ATLAS (1997). URL: https://cds.cern.ch/record/331068.

[39] Sandro Palestini. “The muon spectrometer of the ATLAS experiment”. In: *Nuclear Physics B - Proceedings Supplements* 125 (2003). Innovative Particle and Radiation Detectors, pp. 337–345. ISSN: 0920-5632. DOI: https://doi.org/10.1016/S0920-5632(03)91013-9.

[40] ATLAS Collaboration. “ATLAS level-1 trigger: Technical Design Report”. In: Technical design report. ATLAS (1998). URL: http://cds.cern.ch/record/381429.

[41] ATLAS Collaboration. “ATLAS high-level trigger, data-acquisition and controls: Technical Design Report”. In: Technical design report. ATLAS (2003). URL: https://cds.cern.ch/record/616089.

[42] A. Sidoti. “Minimum Bias Trigger Scintillators in ATLAS Run II”. In: *Journal of Instrumentation* 9.10 (Oct. 2014), pp. C10020–C10020. DOI: 10.1088/1748-0221/9/10/c10020.

[43] M. Aaboud et al. “Measurement of the Inelastic Proton-Proton Cross Section at $\sqrt{s} = 13$ TeV with the ATLAS Detector at the LHC”. In: *Phys. Rev. Lett.* 117 (18 Oct. 2016), p. 182002. DOI: 10.1103/PhysRevLett.117.182002.

[44] G. Aad et al. “K_s^0 and Λ production in pp interactions at $\sqrt{s}$=0.9 and 7 TeV measured with the ATLAS detector at the LHC”. In: *Phys. Rev. D* 85 (1 Jan. 2012), p. 012001. DOI: 10.1103/PhysRevD.85.012001.

[45] S. Chatrchyan et al. “Measurement of neutral strange particle production in the underlying event in proton-proton collisions at $\sqrt{s} = 7$ TeV”. In: *Phys. Rev. D* 88 (5 Sept. 2013), p. 052001. DOI: 10.1103/PhysRevD.88.052001.

[46] N. Oosterman. "Isolating e^+e^- data from the background of reconstructed multiquark decay into strange particles in the ATLAS detector". McGill University (Internal communication), 2022.

[47] C. A. Coughlin. "The Search for Multiquarks at the Large Hadron Collider". McGill University, 2020.

[48] K. O'Sullivan-Steben. "Determination of the Kaon and Lambda particle lifetimes from the ATLAS detector data and study of the background and systematic effects". McGill University, 2019.

[49] S. Sirota. "Systematic studies on lifetimes of strange particles in the ATLAS detector". McGill University (Internal communication), 2022.

[50] Wouter Verkerke and David P. Kirkby. "The RooFit toolkit for data modeling". In: *eConf* C0303241 (2003). Ed. by L. Lyons and Muge Karagoz, MOLT007. arXiv: physics/0306116.

[51] Wouter Verkerke and David P. Kirkby. "RooFit Users Manual v2.91". In: (2008).

[52] Arno R. Bohm and Yoshihiro Sato. "Relativistic resonances: Their masses, widths, lifetimes, superposition, and causal evolution". In: *Phys. Rev. D* 71 (8 Apr. 2005), p. 085018. DOI: 10.1103/PhysRevD.71.085018.

[53] Michael Edward Peskin and Daniel V. Schroeder. *An Introduction to Quantum Field Theory*. Reading, USA: Addison-Wesley (1995) 842 p. Westview Press, 1995.

[54] G. Cowan et al. "Asymptotic formulae for likelihood-based tests of new physics". In: *The European Physical Journal C* 71.2 (Feb. 2011). DOI: 10.1140/epjc/s10052-011-1554-0.

[55] G. Choudalakis. "On hypothesis testing, trials factor, hypertests and the BumpHunter". In: (2011). DOI: 10.48550/ARXIV.1101.0390.

[56] Patrick Koppenburg. *New particles discovered at the LHC*. https://www.nikhef.nl/~pkoppenb/particles.html. (Accessed: 11.08.2022).

[57] E. Gross and O. Vitells. "Trial factors for the look elsewhere effect in high energy physics". In: *Eur. Phys. J. C* 70 (2010). DOI: 10.1140/epjc/s10052-010-1470-8.